MODIS-based modeling of evapotranspiration from woody vegetation supported by root-zone water storage

Guotao Cui[1,2,*], Weichao Guo[2], Michael Goulden[3], Roger Bales[2,4]

[1] Carbon-Water Research Station in Karst Regions of Northern Guangdong, School of Geography and Planning, Sun Yat-sen University, Guangzhou, Guangdong, China. [2] Sierra Nevada Research Institute, University of California, Merced, Merced, California, USA. [3] Department of Earth System Science, University of California, Irvine, Irvine, California, USA. [4] Department of Civil and Environmental Engineering, University of California, Berkeley, Berkeley, California, USA [*] Corresponding author.

Graphical abstract

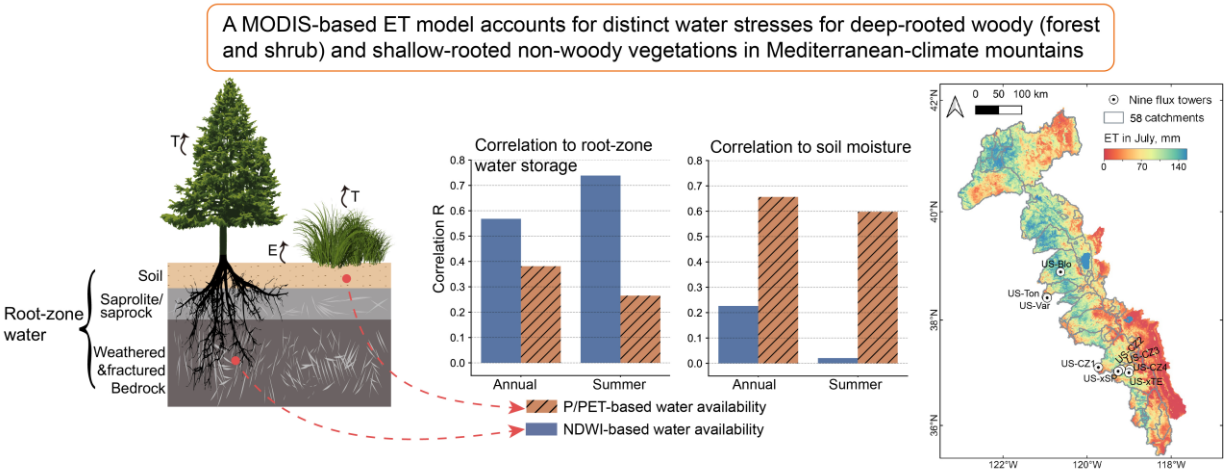

Abstract

As an important process regulating the water cycle, forest evapotranspiration (ET) also reflects vegetation and moisture conditions in response to a changing environment. For mountains in a Mediterranean climate and precipitation largely in winter, inconsistent seasonal variations between water stress and forest growth complicate remote-sensing-based ET modeling. Focusing on the Mediterranean-climate forests of California's Sierra Nevada, this regional study presents an NDWI-CWS (Normalized Difference Water Index-Canopy Water Stress) model to estimate daily ET in a globally important, representative region using MODIS NDWI and NDVI (normalized difference vegetation index) data, plus ground-based meteorological data. Specifically, to account for the important yet less-studied role of root-zone water storage in supporting the growth of deep-rooted woody vegetation (i.e. forest tree and shrub) during dry seasons and droughts, we proposed to use water availability based on NDWI in modeling woody ET. In contrast, given the predominant role of surface soil moisture for non-woody vegetation (e.g. grass) with shallow roots, the model calculated non-woody ET using water availability based on the ratio of cumulative precipitation to potential ET (denoted as P/PET). With ET measurements from 18 flux towers and long-term water-balance measurements at 58 catchments in the relatively data-rich California study area, we compared ET estimates from four modeling experiments with different water availability combinations, and six global and regional ET products. Overall, our NDWI-CWS ET estimates generally agreed best with field measurements, with R^2 of 0.74 for point-scale woody-ET comparison and R^2 of 0.42 for catchment-scale comparison. The mean annual woody ET (634 mm) during water year 2003-2020 was larger than that (353 mm) in non-woody areas. Further, with NDWI-CWS ET estimates and snow data, we estimated that the mean root-zone water storage capacity (601 mm) in forests is double that (285 mm) in non-woody (e.g. grassland) vegetated areas in the Sierra Nevada. We found that remote-sensing NDWI-based water availability is highly correlated with deep root-zone water storage, and much so (correlation R of 0.74) during dry summers. However, P/PET-based water availability reflects surface soil moisture (R of 0.66) modulated by short-term precipitation. Together, explicitly accounting for the distinct roles of root-zone water storage and soil moisture for woody versus non-woody vegetated areas improves MODIS-based ET estimation, which is critical for regional water resources and forest management, in addressing water cycle in a warming climate.

Keywords: Evapotranspiration; Mediterranean mountain; Forest; Woody vegetation; Root-zone water storage; MODIS

1 Introduction

Evapotranspiration (ET) links the water, carbon, and energy cycles through land surface-atmosphere interactions (Jung et al., 2010), transferring water to the atmosphere, through vegetation transpiration and evaporation from soil and open water. From a global

view, terrestrial ET is approximately 60% of total land precipitation, with transpiration accounting for 70% of terrestrial ET (Oki and Kanae, 2006; Poyatos et al., 2021; Wang and Dickinson, 2012). Since mountains provide a large portion of freshwater to the population in downstream regions, making up 50-90% of total freshwater in arid areas (Viviroli et al., 2007; Viviroli and Weingartner, 2004), it is important to understand and predict how mountain ET affects the timing and magnitude of water yield (Bales et al., 2006; Gaertner et al., 2019; Rungee et al., 2019). ET also reflects ecosystem productivity, vegetation conditions, and moisture availability, and is widely used for drought-related studies (Cui et al., 2022a; Teuling et al., 2013; Yang et al., 2021). Accurate ET estimates at a high spatiotemporal resolution are crucial for water resources, ecosystem, and agricultural resource management (Cheng et al., 2021; He et al., 2019; Zhang et al., 2010). However, compared to direct measurements of precipitation and runoff, ET is inherently difficult to measure at large scales and has historically been an uncertain component in regional and global water cycles (Fisher et al., 2017; Ma et al., 2021; Zhang et al., 2010).

ET at point and local scales is often measured by eddy covariance flux towers (Wang and Dickinson, 2012), which are sparsely distributed and costly. Through data sharing and community collaboration, in-situ EC datasets are powerful resources to help understand the ET fluxes in terrestrial ecosystems across multiple networks, including the FLUXNET network (Baldocchi et al., 2001), the AmeriFlux and ChinaFLUX national networks (Novick et al., 2018; Yu et al., 2006), and regional networks e.g. TERENO, HiWATER, and SSCZO (Bales et al., 2018; Bogena et al., 2018; Goulden et al., 2012; Li et al., 2017). To estimate ET at broader spatial and temporal coverages for applications, a number of studies have upscaled point-scale ET from flux towers to global and regional scales through statistical (Goulden and Bales, 2019, 2014) and machine-learning approaches (Jung et al., 2009; T. Xu et al., 2018). Land-surface models are also valuable tools for estimating ET, e.g. the global Breathing Earth System Simulator (BESS) ET product is estimated using a biophysical process-based model (Jiang and Ryu, 2016). Alternatively, various types of satellite remote sensing data have become an emerging and effective way to estimate the spatio-temporal distribution of ET over local to global extents (Bai et al., 2017; Cheng et al., 2021; Consoli and Vanella, 2014; Glenn et al., 2010; Hong et al., 2009). Among a wide variety of satellite datasets, the Moderate Resolution Imaging Spectroradiometer (MODIS) data from NASA's Terra and Aqua satellites are commonly used to provide operational ET products at relatively fine spatial (500 m) and temporal (8-day) resolutions (Maselli et al., 2014; Mu et al., 2011, 2007; Zhang et al., 2019). Methods to estimate MODIS ET can be generally classified into two categories, surface-energy-balance-based (e.g. Surface Energy Balance Algorithm for Land, SEBAL) and vegetation-index-based (e.g. MOD16 and PML2 datasets using the Penman-Monteith model) (Bastiaanssen et al., 1998; Zhu et al., 2022). Since infrequent availability of land-surface-temperature data at coarse spatial resolution in surface-energy-balance-based models may increase the ET uncertainty over heterogeneous landscapes, operational MODIS ET products are often based on relatively simple vegetation-index methods (e.g. using the normalized difference vegetation index, NDVI), which are resilient to data gaps and widely applied over a wide range of landscapes (Glenn et al., 2010; Pan et al., 2020).

Although vegetation-index-based models have successfully estimated ET for operational applications, high uncertainty still exists in ET estimates for some landscapes with specific climates. For example, in regions with a Mediterranean climate, ET estimates from the MOD16 algorithm showed unsatisfactory performance compared to flux-tower sites (Michel et al., 2016; Mu et al., 2011; Vinukollu et al., 2011), likely due to the seasonal variation of vegetation index (e.g. NDVI) differing from that of water stress (Chiesi et al., 2013; Maselli et al., 2014), which is an important factor in regulating seasonal ET. Biederman et al. (2017) also found that MOD16 ET shows underestimations in water-limited regions, and suggested that adding soil-moisture constraints could improve remote-sensing-based ET products. Incorporating water-stress information, indicated by either soil moisture or water-deficit indicators, can yield improved ET estimates (Bai et al., 2017; Miralles et al., 2011). Soil moisture from microwave remote sensing products, e.g. Soil Moisture Active Passive Mission (SMAP), has been successfully used as water-supply control to improve ET prediction (Brust et al., 2021; Purdy et al., 2018). Maselli et al. (2014, 2009) proposed an NDVI-CWS model with a factor named canopy water stress (CWS), which is based on water deficit calculated using precipitation and potential ET. The NDVI-CWS model accounted for the short-term effects of water stress, showing good ET estimates in Mediterranean Italy. Similarly, a water-deficit indicator based on precipitation and PET (potential ET) data showed a high correlation to shallow soil moisture, which is an important environmental factor modulating ET (Rohatyn et al., 2018).

Aside from surface soil moisture, plant-accessible water also includes deep root-zone water storage, e.g. saprolite, saprock, and weathered and fractured bedrock (Baldocchi et al., 2019; Bales et al., 2011; Klos et al., 2018; McCormick et al., 2021; Rempe and Dietrich, 2018). Globally and annually, plant transpiration mainly relies on surface soil moisture (depth $\leqslant$ 30 cm) (Miguez-Macho and Fan, 2021), which is relevant to microwave remote sensing (Feldman et al., 2023). Yet, in seasonally dry environments (Dralle et al., 2021; Jones and Graham, 1993) and droughts (Zhao et al., 2022), water accessed from the deep root zone is another important water source modulating transpiration (Bai et al., 2017; Yu et al., 2007). Forest trees can tap water from deep root-zone water storage (Lewis and Burgy, 1964; Teuling et al., 2010, 2006), e.g. the Mediterranean forest with deep roots in the Sierra Nevada forest of California (Callahan et al., 2022; Kelly and Goulden, 2016; Klos et al., 2018), where water storage capacity in the deeper root zone was estimated to be roughly nine times that in surface soil (Fellows and Goulden, 2017; McCormick et al., 2021). A recent study (Stocker et al., 2023) has found that plant-available water is stored in deep soils ($\geqslant$ 2 m) across 37% of Earth's vegetated surface. It was also reported that in the Sierra Nevada, the vegetation-index-based MOD16 model underestimated montane forest ET and showed a poor correlation to in-site ET measurements (Goulden et al., 2012). Therefore, ET modeling in semi-arid Mediterranean climates and other water-limited regions with deep soils needs to account for water-stress constraints of the plant - accessible water from surface soil moisture, as well as deep root-zone storage. Yet, how to account for the water from deep root-zone storage is understudied, hindering the appropriate representation of its important role in remote-sensing-based ET models, which may limit the accuracy of spatial ET estimation.

Unlike surface soil moisture, which can be directly measured in situ or in some cases remotely sensed by satellites, measuring deep root-zone water storage at a large scale remains a challenge. To estimate the amount of this important source of plant-accessible water, patterns of water deficit based on precipitation minus actual ET have often been used (Dralle et al., 2021; Fellows and Goulden, 2017; McCormick et al., 2021; Roche et al., 2020; Wang-Erlandsson et al., 2016). In general, root-zone water storage capacity is high in deep-rooted woody vegetated areas (i.e. forest and shrub) with high ET, yet is low in shallow-rooted non-woody areas (e.g. grassland) with lower ET (Liu et al., 2022). As ET is an input for the estimation of root-zone water storage, ET modeling cannot directly incorporate root-zone water storage data. However, the amount of root-zone water storage results in vegetation change, which may be used to in turn reflect root-zone water storage. For example, during California's 2012-2015 severe drought the low root-zone water storage caused by moisture overdraft showed a close spatial correlation to the forest die-off patterns from both aerial detection surveys and NDWI (normalized difference water index) change, demonstrating the important role of root-zone water storage in supporting forest growth during dry seasons (Bales et al., 2018; Cui et al., 2022a; Goulden and Bales, 2019). Meanwhile, previous studies have successfully used a moisture index based on remote sensing NDWI to estimate the moisture-dependent gross primary production (GPP) for many terrestrial ecosystems, e.g. mixed forest, evergreen needle-leaf forest, and tropical evergreen forest (Gao et al., 2014; Xiao et al., 2005, 2004). Building on the above understanding, it is worth investigating whether or not incorporating remote sensing NDWI data, possibly related to root-zone water storage, can improve the ET estimates in Mediterranean-climate mountain vegetated areas.

This study focused on estimating daily ET in the Sierra Nevada region of California to investigate the roles of surface soil moisture and deep root-zone water storage in modulating forest and non-woody ET. California was chosen as the study area because it is data rich, with more flux towers and more known about root-accessible water storage than other possible Mediterranean-climate study areas. It is also an area with deep root-accessible water storage providing significant resilience to historical dry seasons and multi-year droughts. We address the question of how remotely sensed data indicate forest water stress regulated by root-zone water storage. First, we improved a canopy-water-stress (CWS)-based ET model (2014, 2009) based on remote-sensing NDVI data from MODIS and ground-based meteorological data, by adding the consideration of water stress in root-zone water storage for deep-rooted woody vegetations. The NDWI data from MODIS were used as a proxy for water availability in woody areas; we named the improved model NDWI-CWS hereafter. Second, we evaluated the ET estimates from NDWI-CWS versus nine other models (three modeling experiments with different model settings and six ET products) at two spatial scales, i.e. a point scale by comparing against ET measurement from flux towers, and a watershed scale by evaluating long-term water-balance components in 58 catchments. Third, we examined the relationship between water availability

versus in-situ soil moisture and root-zone water storage, which was estimated using the ET data from our improved model. We hypothesized that using remotely sensed NDWI data to account for water availability in deep-rooted woody vegetations supported by root-zone water storage can improve ET estimates in Mediterranean-climate mountains.

2 Methods and Data

We estimated daily ET in California's Sierra Nevada (Figure 1) with an NDWI-CWS model using MODIS NDWI and NDVI data, plus ground meteorological data (Figure 2). This section describes the model development in comparison to a previous CWS model (Maselli et al., 2014, 2009), ground flux-tower measurements (Table 2) and watershed water-balance measurements (Table S1) used for model evaluation, and multiple ET products for model comparison. In addition, we present an approach to estimate root-zone water storage based on our ET product and a snowpack product. This root-zone-water storage product allows us to examine its relation to water availability (a limiting factor for ET), in comparison to in-situ soil moisture.

2.1 Study area

Our study area, California's Sierra Nevada, is around 35.4-41.8° North latitude and 117.6°-123.1° West longitude (Figure 1), extending over an area of 87,000 km2 with a highest elevation of 4280 m (Figure S1a in Supporting Information). Its Mediterranean climate is characterized by cold wet winters and dry summers. Annual precipitation in the Sierra Nevada is 870 mm during water year 2003-2020 (WY, from 1st October to 30th September of the following year), with a wide range from 120 to 2840 mm across the domain (Figure S1b). Most precipitation arrives in multiday winter storms and falls as snow above 1500 m elevation, storing as snowpack in high elevations (Cui et al., 2022b, 2020). During rain-free dry summers, drainage from subsurface storage plus late-season snowmelt provide water supply (Bales et al., 2006), with snowmelt being especially important for water-limited forests (Trujillo et al., 2012). Forests consisting of broadleaf and evergreen needleleaf trees commonly grow in the western mountain region, accounting for 45% of the area of the Sierra Nevada (Figure S1c). In this study, deep-rooted woody vegetation also includes shrubland and woody savannas. We classified non-woody areas as those with grassland, savanna, and other lands (Table S2), together representing 54% of the area of the Sierra Nevada (Figure S1c). The remaining 1% domain area is open water. The deep rooting of Sierra forests can reach up to 10-20 m below the surface (Klos et al., 2018), accessing subsurface water to sustain transpiration during dry seasons (Callahan et al., 2022; Goulden and Bales, 2019; Guo et al., 2022; Kelly and Goulden, 2016; Roche et al., 2020).

2.2 The NDWI-CWS model

Here we first introduce the original CWS model (Maselli et al., 2014, 2009), which was proposed to operationally estimate daily ET in Mediterranean-climate Italy. In our NDWI-CWS model, we added modifications to account for the water stress of deep-rooted vegetation in our study area.

2.2.1 Overview of the original CWS model

The original CWS model (Maselli et al., 2014, 2009) uses remote sensing NDVI and landcover data, plus ground meteorological data to estimate daily ET in water-limited Mediterranean Italy. First, an NDVI-based fractional vegetation cover (*FVC*, unitless) at each pixel is calculated to disentangle ET contributed by vegetation transpiration and soil evaporation (Equation 1).

$$FVC_t = \frac{NDVI_t - NDVI_{min}}{NDVI_{max} - NDVI_{min}} \quad (1)$$

where subscript *t* means the value at day *t*; the maximum value ($NDVI_{max}$) and minimum value ($NDVI_{min}$) are set to 0.15 and 0.9, respectively, for general applications (Jiménez-Muñoz et al., 2009; Maselli et al., 2014).

Second, to account for photosynthesis limitations from water stress (Maselli et al., 2014, 2013, 2009), a canopy-water-stress factor (*CWS*, unitless) was calculated using water availability (*AW*),

$$CWS_t = 0.5 + 0.5AW_t \quad (2)$$

where *CWS* varies from 0.5 (maximum water stress) to 1 (no water stress). *AW* is the ratio between cumulated precipitation (*P*, mm) and cumulated potential evapotranspiration (*PET*, mm) over two months for woody vegetation (e.g. forest tree) versus one month for non-woody vegetation (e.g. grass), that is,

$$AW_t = \frac{\sum_{t-60}^{t} P}{\sum_{t-60}^{t} PET} \quad \text{, for woody veg.} \quad (3)$$

$$AW_t = \frac{\sum_{t-30}^{t} P}{\sum_{t-30}^{t} PET} \quad \text{, for non} - \text{woody veg.} \quad (4)$$

Of note, AW_t in the original model ranges from 0 to 1 with a value of 1 denoting sufficient available water, i.e. cumulative *P* equals to or exceeds cumulative *PET*.

Finally, daily actual ET (ET_t, mm) was calculated as the *FVC*-weighted average of vegetation transpiration (the first term in the square bracket of Equation 5) and soil evaporation (the second term),

$$ET_t = PET_t \times \left[FVC_t \times Kc_{Veg} \times CWS_t + (1 - FVC_t) Kc_{Soil} \times AW_t\right] \quad (5)$$

where Kc_{Veg} and Kc_{Soil} are maximum crop coefficients for vegetation and soil, respectively. Following Maselli et al. (2014), Kc_{Soil} was set equal to a low value of 0.2; the value of Kc_{Veg} for woody vegetation was set equal to 0.7, which is the average value for forest between an upper limit of 0.9 and a lower limit of 0.5 (Allen et al., 1998); Kc_{Veg} for non-woody was set to 1.2, i.e. the value for grasses. Of note, the model does not account for sublimation, which often occurs during relatively low-ET winter season in areas with snow cover (Herrero and Polo, 2016; Sexstone et al., 2018). The above equations briefly describe the main procedures in the original CWS model, and we refer to Maselli et al. (2014) for more details.

2.2.2 Modified NDWI-CWS model

Though the original CWS model was proposed for the Mediterranean climate and successfully applied in Italy, we made further modifications to specifically address the near-rain-free dry summer for applications in California's Sierra Nevada. This is because of the notable difference in precipitation climatology between the two regions (Figures S2a,b), since summer precipitation (June-September) represents only 4% of the annual total (870 mm) in the Sierra Nevada, but is substantially larger, 29% of the annual total (810 mm) in Italy. More importantly, in the Sierra Nevada subsurface root-zone water sustaining the transpiration of deep-rooted woody vegetation during the dry growing season may not be reflected by short-term water availability (i.e. the two-month period in Equation 3 above), as the root-zone water storage is often recharged in a longer term, e.g. during wet years or seasons (Goulden and Bales, 2019; Hahm et al., 2019).

As a widely-used classic index for water content at canopy level (Gao, 1996), NDWI (Equation 6) has also been used to quantify forest disturbances (Goodwin et al., 2008; Van Gunst et al., 2016; Wilson and Sader, 2002),

$$NDWI = \frac{\rho_{nir} - \rho_{swir}}{\rho_{nir} + \rho_{swir}} \quad (6)$$

where ρ_{nir} and ρ_{swir} are the spectral reflectance of the near-infrared band and shortwave-infrared band, respectively. Although NDWI is sensitive to water content, it is also affected by canopy structure and leaf area index (Anderson et al., 2010). A comprehensive comparison between NDWI and other alternative indices (e.g. NIRv, EVI, NDVI, CWSI, LAI, VOD, and aridity index) is out of the scope of this study. However, previous studies (Hardisky et al., 1983; Jin and Sader, 2005; Wilson and Sader, 2002) have found that NDWI is more highly correlated with canopy water content than NDVI, and that NDWI-based forest-change detection has higher accuracy.

Since the NDWI decrement during a multi-year drought in California shows high correlations to tree die-off and subsurface water overdraft (Cui et al., 2022a; Goulden and Bales, 2019), to some extent, a factor based on NDWI may reflect vegetation water availability affected by subsurface root-zone water storage, as also discussed in Section 3.3. Therefore, we used the following equation to calculate NDWI-based water availability (*AW*) for woody vegetation, which relies on water stored in the deep root zone in our study area, particularly during dry season and droughts,

$$AW_t = \frac{1 + NDWI_t}{1 + NDWI_{max}} \quad (7)$$

where $NDWI_{max}$ is the maximum NDWI value during the summer growing season at each pixel. *AW* with a range of 0.5-1 from Equation 7 represents temporal dynamics and spatial patterns of vegetation water availability, which has been used to denote the effect of water on plant photosynthesis for water-dependent GPP estimations (Gao et al., 2014; Xiao et al., 2005, 2004). The *CWS* from NDWI-based *AW* (Equation 3) for woody vegetation has a range of 0.75-1, with 0.75 denoting severe water stress and 1.0 indicating no water stress. The larger low-bound value (i.e. 0.75) of variable *CWS* for woody vegetation reflects its higher resistance to water stress than non-woody vegetation (0.5), as their roots can access deep root-zone water storage (Paço et al., 2009; Wilschut et al., 2022; H. Xu et al., 2018).

Overall, the NDWI-CWS model calculates *AW* using NDWI-based Equation 7 for woody vegetation (i.e. forest tree and shrub) and P/PET-based Equation 4 for non-woody vegetation. The daily *ET* is then estimated by Equation 5, with the *AW* term for soil evaporation using Equation 4. These model settings were chosen after evaluating model performance across different modeling experiments (Table 1, described in Section 2.3 below). As the Priestley-Taylor equation provides reasonable estimates of PET in forests and lakes (Priestley and Taylor, 1972; Rao et al., 2011; Rosenberry et al., 2007), our NDWI-CWS model uses the Priestley-Taylor-based PET, instead of using the PET from the Jensen-Haise method (Jensen and Haise, 1963) in the original CWS model, which might provide unreasonable, negative PET values when temperatures are low (Zhao et al., 2021). Our analysis showed that

using PET from the Jensen-Haise method significantly underestimates ET, compared to the Priestley-Taylor method and in-situ observations. We also added ET estimates for open water, assumed to be equal to PET (Guerschman et al., 2022; Zhang et al., 2019), which is one component of landscape- and basin-scale ET budgets.

As crop coefficients (*Kc*) vary across different ecosystems and soil conditions (Allen et al., 2005; Liu et al., 2017), the NDWI-CWS model uses calibrated crop coefficients in Equation 5 using California's ET measurements to further improve model performance, instead of the determined values used for applications in Italy (Maselli et al., 2014). Using the globally convergent shuffled-complex-evolution algorithm (SCE-UA, Duan et al., 1992), the Kc_{Veg} values for woody and non-woody vegetations, as well as Kc_{Soil} were automatedly calibrated by minimizing the root-mean-square error (RMSE) of 8-day ET between model estimates and in-situ ET measurements across all years from 18 flux towers in California (Figure 1 and Table 1, described in Section 2.5 below).

2.3 Modeling experiments and evaluation

We designed four modeling experiments with different formulas for available water and crop coefficients (Table 1), to examine their impacts on ET simulation and to choose the best model setting for our study area. Experiment 1 employed the identical setting in the original CWS model, which uses P/PET-based AW for woody and non-woody vegetated areas. The second experiment (named NDWI-woody) switched to the NDWI-based AW (Equation 7) for woody areas, but kept using P/PET-based AW for non-woody, to test whether our NDWI-based AW improves ET simulations in deep-rooted woody areas. As opposed to Expt 2, the NDWI-non-woody (Expt 3) used NDWI-based AW for non-woody areas to examine whether or not NDWI-based AW is applicable in non-woody areas (e.g. grasses). Finally, the NDWI-CWS model (as described above, labeled as Expt 4 here) was similar to the NDWI-forest setting. Rather than using the default crop coefficients in Expt 1-3, calibrated coefficients (woody $Kc_{Veg} = 0.59$, non-woody $Kc_{Veg} = 1.00$, and soil $Kc_{Soil} = 0.30$) were used in the NDWI-CWS model. Experiments 2-4 used P/PET-based AW to denote the water availability for soil evaporation in Equation 5.

Two sources of "ground-truth" ET datasets were used to evaluate modeling ET at both point and catchment scales. One was direct ET measurements from 18 flux towers in California (9 sites inside the Sierra Nevada, Figures 1 and S1d). The other dataset was indirectly estimated based on water balance at 58 catchments (Figures 1 and S1d) with natural-flow data (Q, mm). The water-balance approach is often used as an accurate way to validate ET estimates at large scales (N. Ma et al., 2020; Rodell et al., 2004). Long-term water-year ET was calculated as P – Q – ΔS, where the long-term (≥ 10 years) catchment-scale terrestrial water storage ΔS (mm) approaches zero, and thus this comparably minor term was ignored in this study (Cheng et al., 2021; Guerschman et al., 2022; Liu et al., 2016; Ma et al., 2021). The catchment-scale evaluation implicitly includes the impacts of complex but often unmeasured water movement, e.g. lateral flow, providing an overall ET performance at the catchment management scale. To evaluate our models' performances compared to "ground-truth" ET datasets and other modeling ET datasets, we used the RMSE, coefficient of determination (R^2), and mean bias difference (MBD) with negative values denoting underestimation, and values closer to zero denoting better agreement.

2.4 Estimates of root-zone water storage

As we hypothesized that NDWI-based water availability is relevant to water stored in the deep root zone, which is important in sustaining ET in forests in our study area during dry periods, and episodic or multi-year droughts, we further calculated root-zone water storage (*RZWS*, mm) for analyzing its relationship to water availability. Using a water-balance approach (Dralle et al., 2021; McCormick et al., 2021; Wang-Erlandsson et al., 2016), we first calculated the root-zone water deficit (*D*, mm) on day *t* as the running, accumulated difference (*A*, mm) between outgoing water flux (F_{out}, mm) and incoming water flux (F_{in}, mm) over the previous day, as shown in Equations 8 and 9,

$$A_{t-1\to t} = F_{out,t-1} - F_{in,t-1} = ET_{t-1} - (P_{t-1} - \Delta SWE_{t-1}) \quad (8)$$

$$D_t = max(0, D_{t-1} + A_{t-1\to t}) \quad (9)$$

where, to obtain a lower bound of *D* estimates, we conservatively used a lower-bound of F_{out}, which consists of ET, with runoff and other outgoing fluxes being ignored, following previous studies (Dralle et al., 2021; McCormick et al., 2021; Wang-Erlandsson et al., 2016). However, since snowpack accumulation and ablation play an important role in regulating incoming water flux in the Sierra Nevada (Bales et al., 2006; Henn et al., 2020), we specifically proposed to calculate F_{in} as the effective incoming water, which is difference between precipitation and snow water equivalent change (i.e. ΔSWE, mm; with a positive value denoting

increased snowpack storage in one day). Compared to a snow-cover-threshold-based correction used in previous study (Dralle et al., 2021), quantitively accounting for SWE change can better represent seasonal snow dynamics, the portion of precipitation stored as snowpack, and the role of melted snow in recharging root-zone storage, potentially providing more-robust estimates of daily root-zone water storage.

The daily root-zone water deficit (D_t) at each pixel is tracked continuously with an initial D on the first day of our calculation period WY2004-2020 being assumed zero (i.e. $D_{t=1} = 0$ on Oct. 1, 2003) (Dralle et al., 2021; McCormick et al., 2021). The maximum value of D_t throughout our study period is defined as the root-zone water storage capacity ($RZWS_{max}$, mm). Thus, the daily root-zone water storage ($RZWS$) was calculated by:

$$RZWS_t = RZWS_{max} - D_t \quad (10)$$

In this study, we masked out the pixels with long-term averaged $ET - P > 0$ to eliminate the areas that may have unmeasured incoming fluxes, e.g. water subsidies from lateral flow (Cui et al., 2022a; Maxwell and Condon, 2016), following Dralle et al. (2021) and McCormick et al. (2021). Of note, modeled daily ET is used as input for root-zone-water-storage calculation, and the masking procedure does not impact the site-scale and catchment-scale ET estimates. To investigate the relationship between water availability for ET versus root-zone water storage and surface soil moisture, we deseasonalized time-series data to remove their own strong seasonal signals, which may result in spurious correlations (Sriwongsitanon et al., 2016). The deseasonalization procedure includes three steps: a) normalizing time-series data to be between 0 and 1 range, b) computing the average values of normalized data as seasonal patterns, and c) calculating deseasonalized data as the residue between normalized data and seasonal patterns.

2.5 Data sources and processing

Here we describe the sources and processing procedures of remote-sensing MODIS data and ground-based meteorological data that were used as model inputs to estimate daily ET during WY2003-2020. Following that we describe the ET measurements from flux towers used for model calibration and point-scale evaluation, plus their in-situ soil moisture measurements. Auxiliary datasets include natural streamflow data used for catchment-scale ET evaluation, six other ET products (two regional and four global products) as comparisons to our model, and a snow product used as inputs for estimating root-zone water storage.

2.5.1 Remote-sensing MODIS data

The NDVI and NDWI values were derived based on surface spectral reflectance from MODIS satellite sensors, with a temporal resolution of 8 days and a spatial resolution of 500 m (MYD09A1 product, https://lpdaac.usgs.gov/products/myd09a1v006/). Annual landcover types based on International Geosphere-Biosphere Programme (IGBP) classification from MODIS MCD12Q1 product (https://lpdaac.usgs.gov/products/mcd12q1v006/) were used to reclassify our study area into woody, non-woody, and open water (Table S2). Using the Google Earth Engine platform (Gorelick et al., 2017), we masked out cloud-contaminated pixels and calculated 8-day time-series data of NDVI and NDWI, which were then linearly interpolated to a daily basis (Battista et al., 2018; Chiesi et al., 2013; Maselli et al., 2014).

2.5.2 Ground meteorological data

Daily minimum and maximum temperature and precipitation were obtained from the Parameter-elevation Relationships on Independent Slopes Model (PRISM, https://prism.oregonstate.edu/), which was developed using ground measurements at 13,000 sites and showed good agreement with ground rain-gauge measurements (Daly et al., 2008). Although PRISM has limitations in high-elevation complex terrain due to rain-gauge undercatch during snowfall (Cui et al., 2022b), PRISM is still considered one of the best gridded gauge-based datasets in the U.S. (Pirmoradian et al., 2022). We also used rain-gauge measurements from 180 sites in the Sierra Nevada, with elevations ranging from 142 to 3263 m (Text S1 and Figures S3a,b). Evaluation against in-situ gauge measurements showed that PRISM generally aligns well with gauge measurements (Figure S3c), though its performance at the high-elevation band around (2900 m) is slightly reduced, compared to two lower-elevation bands (500 and 1700 m; Figures S3d-f). To match the spatial resolution of 500 m in our study, we bilinearly interpolated the 800-m PRISM data, following previous water-balance-related studies in California (Cui et al., 2022a; Goulden and Bales, 2019; Roche et al., 2022). With these meteorological data, we used the mountain microclimate MTCLIM algorithm (Bohn et al., 2013; Kimball et al., 1997; Martínez et al., 2022; Thornton et al., 2000) to estimate incoming shortwave solar radiation, and then calculate daily PET using the Priestley-Taylor method.

2.5.3 ET measurements from flux towers

Eddy covariance measurements from 18 flux towers in California (including nine sites inside the Sierra Nevada; see Figures 1 and S1d, Table 2) were retrieved from the AmeriFlux (https://ameriflux.lbl.gov/) and Sierra Critical Zone Observatory

(https://www.ess.uci.edu/~california/). Since there are only 9 flux-tower sites with available data inside the Sierra Nevada, including the other 9 flux towers in southern California can not only increase our limited number of flux-tower sites, but also can help calibrate and evaluate the model more broadly (Cui et al., 2022a; Goulden and Bales, 2019). The 18 flux towers are located in varying landscapes (including evergreen needleleaf forests, mixed forests, savannas, shrublands, grasslands, and desert barren vegetation). Reclassification of the flux towers into 13 woody and five non-woody sites was based on ground-level land-cover metadata and remote-sensing percent woody cover estimated using the 10-m WorldCover product (Zanaga et al., 2021), with sites with percent woody cover ≥ 40% classified as woody (Table 2 and Figure S4). Following the data processing procedure described in Rungee et al. (2019) and Goulden et al. (2012), we first automatically filled 30-min data gaps using regression models and linear interpolations. Second, gap-filled 30-min data were aggregated to daily values, and the energy balance was closed using linear regression of turbulent fluxes and available energy forced through the original 30-min data (Goulden et al., 2012; Rungee et al., 2019; Twine et al., 2000). Afterward, daily time series were then quality filtered to remove suspicious points by visual inspection. In total, we collected 52,500 site-day ET data from the 18 flux towers, which were also aggregated to an 8-day basis for calibrating our NDWI-CWS model. The 27,100 site-day data from the nine sites inside the Sierra Nevada were specifically used for evaluating model performance in the mountains. In addition, for each of these nine flux-tower sites we averaged their daily soil water content (SWC, %) over shallow soil depths (≤ 30 cm below surface), as the soil-moisture sensors across the nine sites are placed at different depths ranging from 5 to 90 cm (Baldocchi et al., 2004; Goldstein et al., 2000; Sadeghi et al., 2022).

2.5.4 Other ET datasets

Six modeled ET products (four biophysical models, one machine-learning model, and one statistical model) were used to benchmark our NDWI-CWS model. First was an operational MODIS-based global ET product at 500-m resolution and 8-day intervals (https://developers.google.com/earth-engine/datasets/catalog/MODIS_006_MOD16A2), using the MOD16 algorithm (Mu et al., 2011, 2007; Running et al., 2017). Another MODIS-based global 500-m ET product at 8-day intervals was Penman-Monteith-Leuning Version 2 (PML2, https://developers.google.com/earth-engine/datasets/catalog/CAS_IGSNRR_PML_V2_v017), which uses a coupled diagnostic biophysical model (Zhang et al., 2019). The third was a daily global product from the Global Land Evaporation Amsterdam Model (GLEAM) at a 0.25°spatial resolution, which uses a data assimilation technique for estimating water availability (Martens et al., 2017). The fourth product was monthly ET at 1-km resolution developed for California (https://code.earthengine.google.com/?asset=users/daviddralle/bessv2), using a biophysical model named BESS (Baldocchi et al., 2019). For the remaining two models, one was FLUXCOM, using machine learning to merge energy flux measurements from flux towers and MODIS remote sensing data (Jung et al., 2019). FLUXCOM provides latent heat flux (LE) and sensible heat flux (H) at 0.0833° resolution and 8-day intervals (from 2001 to 2015), which were used to calculate ET and evaporative fraction ($EF = \frac{LE}{LE+H}$). The other product was from the Center for Ecosystem Climate Solutions (CECS, https://cecs.ess.uci.edu/data-atlas/), providing monthly ET data at a 30-m resolution for California using a statistical approach. CECS ET was estimated based on the high correlation between ET measurements and Landsat-based NDVI (Goulden and Bales, 2019, 2014). For model comparison, we bilinearly interpolated data from GLEAM, BESS, and FLUXCOM data to match the common 500-m resolution, and aggregated the CECS data to the 500-m resolution for our analyses. We also accumulated daily flux-tower ET measurements and estimates from our NDWI-CWS model to 8-day and monthly scales to match the time scales of these six ET datasets.

2.5.5 Auxiliary datasets

We collected long-term natural-streamflow data from 58 streamflow gages, including 26 gages obtained from the California Data Exchange Center (CDEC, https://cdec.water.ca.gov/) and 32 gages from the U.S. Geological Survey (USGS). Monthly natural-flow data from 26 CDEC gages were reconstructed by accounting for flow changes induced by upstream operations, e.g. diversions and reservoir storage (Huang and Kadir, 2016; Maurer et al., 2022). For long-term water-balance-based ET comparison, we filtered out streamflow gages with < 10 of years data during our study period. We selected 32 unimpaired gages from the USGS GAGES-II dataset (Falcone, 2017, 2011) from all USGS gages inside the Sierra Nevada, by filtering the dataset to include only gages with data record coverage of at least 10 years and no upstream dams. As a result, we collected natural-flow data from outlet gages of 58 catchments encompassing most of the Sierra Nevada

(Table S1; Figures 1 and S1d). Drainage areas were determined based on the GAGES-II dataset, ranging from 2 to 22,977 km2. The natural-flow data were aggregated to a water-year basis for our analyses.

Additionally, we collected the daily UA SWE product at a 4-km resolution (Broxton et al., 2019), which assimilates in-situ snow measurements with PRISM data. The UA SWE product has a good performance in forested areas (Cho et al., 2020), which is important for our study. The daily SWE data were bilinearly interpolated to 500-m resolution, the same as the spatial resolution of our NDWI-CWS ET, for estimating root-zone water storage.

3 Results

3.1 ET estimates from NDWI-CWS model

First, we illustrated the daily variables for estimating daily ET in woody versus non-woody vegetation using two flux-tower sites (Figure 3). The 2015-m elevation woody site US-CZ3 showed higher precipitation and lower temperature compared to the 400-m elevation non-woody site US-CZ1 (Figures 3a,h). Vegetation greenness (NDVI) at US-CZ3 was generally higher than at US-CZ1, reflecting a higher fractional vegetation cover. US-CZ1 showed a seasonal pattern with relatively higher fractional vegetation cover values during winter and early spring, and lower dry-summer values (Figures 3b,i), with relatively constant year-round values at US-CZ3. The water availability based on NDWI for woody US-CZ3 showed relatively lower values during dry summer than during spring. Due to vegetation difference, water availability at non-woody US-CZ1 was calculated differently based on P/PET, exhibiting a clear seasonal pattern with low values during the rain-free summer. The canopy water stress factor CWS exhibited a similar pattern as water availability for both sites. Annual PET (1925 mm) at US-CZ1 reflected higher temperatures compared to that (1800 mm) at US-CZ3 (Figures 3c,j). As shown by both daily flux-tower measurements and modeled estimates, the observed annual ET at US-CZ3 (595 mm) was larger than that at US-CZ1 (343 mm). Correlations between daily ET measurements and modeled estimates were ≥0.6 for the two sites. The statistically significant increases in daily ET measurements after precipitation events were also captured by the NDWI-CWS model (Figure S5). In-situ measurements show lower ET during dry summer at the non-woody site, versus peak ET during the growing season in summer at the woody site. Although our NDWI-CWS model yielded higher ET estimates during the dry season (summer) of WY2013, it does not exhibit a consistent overestimation bias during dry seasons, as shown in Figure S6. We also analyzed variable anomalies by removing seasonality from data. At the woody US-CZ3 site (Figures 3d-g), wetter soil moisture (SWC) and its anomalies during spring season did not show a noticeable correlation to anomalies of evaporation efficiency (ET/PET), NDWI-based AW, CWS, and ET. However, at the non-woody US-CZ1 site (Figures 3k-n), the wet-dry-pattern of soil-moisture anomalies during spring season showed strong positive correlations to anomalies of evaporation efficiency (R=0.81), P/PET-based AW (0.81), CWS (0.81), and ET (0. 57) from our model, indicating that P/PET-based AW is relevant to the variability of soil moisture.

Second, at an 8-day temporal scale, we compared NDWI-CWS ET with observed 8-day ET at the nine sites inside the Sierra Nevada (Figure 4), showing a good agreement (mean R2=0.66). Albeit there was general agreement with in-situ measurements, noticeable discrepancies at certain sites (e.g. US-Blo and US-Ton) also existed in NDWI-CWS and FLUXCOM models. Both may note capture the variability of measured ET during growing seasons, and underestimate peak ET at some sites (e.g. US-Blo and US-Ton with negative MBDs). When compared to measured ET at the nine sites, both NDWI-CWS and FLUXCOM yielded similar R2 values of 0.68 and 0.70 during the growing seasons versus non-growing seasons, respectively, indicating relatively consistent performance through all seasons. At the woody forest site with the longest record (US-CZ3, 10 years), both NDWI-CWS and FLUXCOM performed well in depicting the measured ET patterns during growing seasons. The NDWI-CWS model yielded a higher R2 of 0.65 than FLUXCOM (0.58), but also had a larger MBD of 1.38 mm than FLUXCOM (0.30 mm). At US-Ton, FLUXCOM yielded a higher R2 of 0.75 than the NDWI-CWS model (0.68), indicating the advantage of its machine learning for leveraging flux-tower data. Regarding ET anomaly (Figure S7), the NDWI-CWS model had a higher correlation of 0.6 than FLUXCOM (0.49) at US-CZ3. Overall, across the nine Sierra sites, ET anomalies from both NDWI-CWS and FLUXCOM were positively correlated to those from flux-tower observations, with R values of 0.47 and 0.46, respectively, indicating both models can somehow capture ET variability. Regarding the nine California sites outside the Sierra Nevada (Figure S8), NDWI-CWS model estimates showed good agreement at the woody forest US-SCf site (R2 of 0.54, not used in FLUXCOM's training), whereas FLUXCOM showed noticeable underestimation with R2 of 0.02 and MBD of -11.15 mm. For five woody sites with shrublands (US-SO3, US-SO4, US-SO2, US-SCw, and US-SCc), the

mean R2 values for NDWI-CWS and FLUXCOM models respectively were 0.33 and 0.19 (Figure S8), indicating NDWI-CWS model has a better performance in ET at shrublands than does FLUXCOM. In terms of ET anomaly across the nine sites outside the Sierra Nevada (Figure S9), NDWI-CWS yielded a larger correlation (R of 0.43) with observation than FLUXCOM (R of 0.27). Across all the 18 sites in California, NDWI-CWS (FLUXCOM) had a larger mean R2 value of 0.63 (0.50) at seven woody forested sites than the mean R2 value of 0.33 (0.07) at five woody shrubland sites, showing that NDWI-CWS (FLUXCOM) has a better performance in ET at woody forested sites than at woody shrubland sites.

Third, from a climatology view, spatial patterns of monthly ET (Figure 5a) show higher values in the western versus eastern Sierra, reflecting less water due to the rain shadow east of the Sierra crest. Monthly woody ET is higher than non-woody ET, but is lower than open-water ET (Figures 5a,b). The PET indicated by open-water ET peaks at 252 mm in July, coincident with peak woody ET (94 mm, Figure 5b). However, non-woody ET peaks one month earlier (45 mm in June), and declines during the summer. This simulated seasonal variation is consistent with in-situ ET measurements (Figures 3c,j). Annual ET totals for open water, woody, and non-woody are 1642, 634, and 353 mm, respectively. Summer ET contributes 53%, 53%, and 42% of annual totals for open water, woody, and non-woody, respectively. In terms of elevational patterns below 1000 m (Figure 5c), both woody and non-woody ET increases with elevation, coinciding with the general increase in precipitation (Figure S1e). However for areas above 1000 m elevation, despite precipitation well in excess of their ET values, the ET values generally decrease with elevation, reflecting apparent energy limitations (Guo et al., 2022).

3.2 Comparison across modeling experiments and products

3.2.1 Point-scale comparison against ET measurements from flux towers

Comparisons across four modeling experiments and six other ET products at three temporal scales (1-day, 8-day, and monthly) indicate that in most cases NDWI-CWS simulations match flux-tower ET measurements better than other simulations (i.e. three other modeling experiments and six gridded ET products), particularly for woody sites (Table 3). For 1-day ET, using NDWI-based AW for woody areas (NDWI-woody) improved R2 to 0.44 from 0.36 (original CWS). However, using NDWI-based AW for non-woody areas (NDWI-non-woody) yielded a smaller R2 of 0.18. Our NDWI-CWS using calibrated crop coefficients (Table 1) showed the smallest RMSE of 0.87 mm, the largest R2 of 0.46, and a closer MBD to zero (-0.01 mm), indicating that the calibrated NDWI-CWS further improves results compared to NDWI-woody. The GLEAM data shows the lowest R2 of 0.01, indicating that its original coarse-resolution data cannot capture the variability of in-situ flux-tower data.

Similarly, for 8-day ET in seven Sierra woody sites (Table 3), NDWI-woody and original CWS showed comparable R2 values of 0.54, however NDWI-woody yielded a smaller RMSE of 6.79 mm than original CWS (8.15). NDWI-CWS showed an R2 value of 0.57, and FLUXCOM yielded an R2 of 0.65, a larger value than those from PML2 (0.50), MOD16 (0.26), and GLEAM (0.01). FLUXCOM yielded the highest R2, indicating that its machine-learning approach takes advantage of flux-tower measurements. Using 8-day ET from two Sierra non-woody sites, NDWI-CWS and original CWS yielded comparable R2 values of 0.67 and 0.68, respectively. However, NDWI- CWS had a lower MBD (0.79 mm) than original CWS (2.33 mm), demonstrating a reduction in model overestimation. MOD16 yielded the largest R2 of 0.73, but showed underestimation with a negative MBD of -1.38 mm. The GLEAM yielded the lowest R2 of 0.10, reflecting its limited ability to capture the variability of in-situ flux-tower data. Across all 18 sites, FLUXCOM showed a relatively lower R2 of 0.50 compared to its performance inside Sierra Nevada, again indicating its relatively lower performance at the nine sites outside Sierra. Our NDWI-CWS showed the highest R2 of 0.59 across 18 sites in California.

Regarding monthly ET comparison across 18 sites in California (Table 3), our NDWI-CWS showed the best performance with the lowest RMSE of 16.99 mm, the largest R2 of 0.71, and the most-unbiased MBD of 0.09 mm. For the Sierra woody sites, NDWI-CWS achieved the second-highest R2 of 0.74, which was lower than FLUXCOM (0.78), but higher than those from MOD16 (0.0.43), PML (0.48), GLEAM (0.02), BESS (0.57), and CECS (0.65). For the Sierra non-woody sites, MOD16 had the highest R2 (0.81), followed by NDWI-CWS (0.75) and FLUXCOM (0.69). Generally, a longer-temporal-scale (monthly) evaluation yields larger R2 values compared to 1-day and 8-day scales. Among the six off-the-shelf products, FLUXCOM has the best ET estimates inside the Sierra Nevada.

Further evaluation using Taylor diagrams (Taylor, 2001) at the nine sites inside the Sierra Nevada (Figure 6) again suggested that both NDWI-CWS and FLUXCOM have better performance in woody sites (Figures 6a-e) than the other models. Although

FLUXCOM data were not evaluated at US-xTE and US-xSP (FLUXCOM data ended in 2015 not covering the in-situ measurements, Figure 4). For example, at US-CZ3 site (Figure 6c) NDWI-CWS showed a larger correlation R of 0.93 and a lower RMSE of 13.53 mm than did the other three modeling experiments and six ET products. The standard deviation (34.47 mm) of NDWI-CWS ET agreed with that (32.15 mm) of flux-tower measurements, resulting in a visually closer distance to the observed ET (Figure 6c). Among the six ET products, FLUXCOM ET showed a larger correlation R of 0.90 than MOD16 (0.51), PML (0.79), CECS (0.86), GLEAM (-0.01), and BESS (0.67). Regarding the two non-woody sites (Figures 6f,h), NDWI-CWS and FLUXCOM yielded comparable ET estimates at US-CZ1, while MOD16 yielded the best estimates at US-Var. The NDWI-non-woody and GLEAM showed inferior performances compared to others.

3.2.2 Catchment-scale comparison against water-balance-based ET

With long-term annual water-balance-based ET (i.e. $P - Q$) estimates at 58 catchments (Table 4 and Figure 7), our NDWI-CWS shows reasonable agreements (RMSE of 113.01 mm, R2 of 0.42, and MBD of 26.85 mm), compared to other ET estimates. For the other three modeling experiments, NDWI-woody simulated a larger R2 (0.40) than did the original CWS (0.35), but showed a larger RMSE of 140.08 versus 106.21 mm (Figure 7a). It is worth noting that NDWI-non-woody yielded a low R2 (0.12, Figure 7b), consistent with the findings using point-scale flux-tower ET measurements (Table 3), indicating that NDWI-based AW is not applicable for non-woody areas. Among the six ET products, PML2 and MOD16 showed R2 values of 0.38 and 0.37, respectively, although PML2 had a slight overestimation (MBD of 40.47 mm) and MOD16 yielded a notable underestimation (MBD of -216.99 mm, Figure 7c), which is consistent with previous finding that MOD16 underestimates ET (Biederman et al., 2017; Goulden et al., 2012). Both GLEAM and BESS yielded low R2 values of 0.14 and 0.17, respectively (Figure 7d). The BESS ET showed a relatively homogenous pattern, in other words, it did not capture the ET-increase pattern in high-ET catchments. FLUXCOM and CECS showed comparable R2 values of 0.37, respectively, although FLUXCOM had a slight overestimation (MBD of 30.40 mm) and CECS yielded an underestimation (MBD of -70.97 mm, Figure 7e). The noticeable underestimation from CECS appeared in the Lake Tahoe catchment (gage TRF), which has the largest percentage (21.3%, Table S1) of open water, since CECS excludes ET estimates in open-water areas. Among the 10 gridded ET estimates, our NDWI-CWS shows the overall best performance, which has the largest R2 value at the catchment scale (Figure 7f).

3.3 Root-zone water storage and soil moisture

Using root-zone water storage capacity (*RZWSmax*) calculated using NDWI-CWS ET, precipitation, and SWE (Figure S10), we found that woody areas have a statistically significant larger root-zone water storage capacity (mean±std of 601±327 mm), which is approximately double the mean value in non-woody areas (285±283 mm, Figure 8). This coincides with woody ET being higher than non-woody. The root-zone water storage capacity shows a spatial pattern with higher values in western than eastern Sierra (Figure S11). This can be explained by that larger root-zone water storage capacity is needed in more-vegetated western Sierra to sustain ET during dry periods, since plants size their root depth and root-zone water storage capacity to adapt to prevailing hydroclimate (Schenk and Jackson, 2005; Stocker et al., 2023; Wang-Erlandsson et al., 2016), i.e. dry summer season or drought for Sierra. Water supply is another important factor that regulates root-zone water-storage capacity. The higher precipitation in woody areas (Figure S12a) supports larger woody ET and water storage in woody root zones. Precipitation can refill the root-zone water storage over one year or multiple years. In ≥ 85% of non-woody and woody areas (Figure S12b), annual precipitation exceeds root-zone water-storage capacity. In some areas, overdrafted root-zone water storage during drought may take multiple years to replenish (Figures S12f,g).

At an annual scale, the NDWI-based water availability showed a larger correlation (0.57) with root-zone water storage (RZWS, Figure 9a) than did the P/PET-based water availability (0.38), using deseasonalized values (Figure S13). The correlation between NDWI-based water availability and root-zone water storage was even higher (0.74) for the dry summer season, during which P/PET-based water availability shows a poor correlation (0.27), since its short time scale (30 days) cannot account for the moisture carry over through seasons or years. On the contrary, we observed larger correlations between P/PET-based water availability and surface soil moisture than that for NDWI-based water availability (Figures 9b and S13). The correlations between P/PET-based water availability and soil moisture were 0.66 and 0.60 for the annual scale and summer season, respectively, which were both higher than those for NDWI-based water availability. We also examined correlations between water

availability and evaporation efficiency (ET/PET), and evaporative fraction (Figure S15), which are both proxies for ET water stress. P/PET-based water availability showed stronger positive correlations with ET/PET and evaporative fraction at an annual scale, but weaker correlations during dry summer (Figures 9c,d). In contrast, NDWI-based water availability showed larger positive correlations to ET/PET and evaporative fraction during dry summer than at an annual scale (Figures 9c,d), showing that it better reflects water stress during dry summer. A map comparison (Figure S16) shows that AW captures wet anomalies in woody areas and dry anomalies in non-woody areas, compared to evaporative fraction. These results suggested that NDWI-based and P/PET-based water availability are relevant to ET water stress. NDWI-based water availability can indicate deep root-zone water storage, and much so during dry summer. Instead, surface soil moisture can be represented by P/PET-based water availability.

4 Discussion

4.1 Distinct water sources for sustaining ET in vegetation areas during dry seasons

It is known that deep-rooted woody vegetation (e.g. forest tree) and non-woody vegetation (e.g. grass) use water from different sources, reflecting their different life strategies (Baldocchi et al., 2004). Through hydraulic lift (Ishikawa and Bledsoe, 2000), deep roots of forest trees tap water from root-zone water storage (Lewis and Burgy, 1964). In our case, deep-rooted Sierra forests can withdraw water from root-zone water storage to sustain their ET demands during dry summer growing seasons and multi-year droughts (Bales et al., 2018; Cui et al., 2022a; Goulden and Bales, 2019; Guo et al., 2022; Klos et al., 2018), when water inputs from precipitation, snowmelt, and surface soil moisture are not sufficient. The ability of forest trees to withstand severe water deficits during dry conditions is also strengthened by their physiological and structural adjustments, e.g. water-loss control by stomatal closure (Ambrose, 2018; Harrison et al., 1971) and reducing hydraulic conductivity (Eamus and Prior, 2001). Previous studies suggest that the canopy water content indicated by NDWI change is a good indicator of tree mortality (Goodwin et al., 2008; Van Gunst et al., 2016). Meanwhile, recent work suggested that NDWI change correlates to subsurface water overdraft during a multi-year drought in the Sierra Nevada (Cui et al., 2022a; Goulden and Bales, 2019). Since we have found a high correlation between NDWI-based water availability and root-zone water storage, and much so for the dry summer growing season, taking into account the role of root-zone water storage using NDWI-based water availability improves woody ET estimates. This explains why our NDWI-CWS model shows better agreement with both woody ET measurements from flux towers, and long-term catchment-scale water-balance components, compared to the original CWS model, which only considers available water from short-term precipitation using P/PET-based water availability.

In contrast, non-woody vegetation in mountains has a relatively shallow root system with limited access to deep root-zone water storage (Krishnan et al., 2012). For example, shallow-rooted grasses (Jackson et al., 1996) are unable to withdraw water from deep sources (Baldocchi et al., 2004), and rely on soil moisture to maintain their ET (Sun et al., 2013; Wolf et al., 2013). Additionally, it was reported that ET in grassland ecosystems is sensitive to surface soil moisture, but not to deep root-zone water storage (Krishnan et al., 2012; Kurc and Small, 2004). As also indicated by the poor performance of our modeling experiment NDWI-non-woody, which used NDWI-based water availability for non-woody and showed substantial ET overestimation, it is not appropriate to estimate ET in non-woody areas using deep root-zone water storage. Since we have observed a strong correlation between P/PET-based water availability and surface soil moisture, our NDWI-CWS model uses the P/PET-based water availability for non-woody ET and soil evaporation, reflecting the correct dominant water source (i.e. surface soil moisture regulated by short-term precipitation) for non-woody vegetations.

Though MODIS-based ET models have adopted some approaches to indicate water stress from soil moisture, e.g. by vapor pressure deficit (Mu et al., 2011, 2007) and P/PET-based water availability (Maselli et al., 2014, 2009), the important role of deep root-zone water storage in woody ET modeling was often omitted. Our root-zone water storage estimates suggested higher values in woody than in non-woody areas, consistent with observed greater storage capacity in densely forested areas (Callahan et al., 2022; Tague, 2022). Given the close relationship between NDWI and root-zone water storage found in this study, as well as in a previous study using a semi-distributed hydrologic model (Sriwongsitanon et al., 2016), we suggest taking the advantage of remote-sensing NDWI data to explicitly account for this critical water component in modeling woody ET. This is not limited to regions with a Mediterranean climate, but is also important for other water-limited regions and areas with deep root-zone water storage, deserving further investigation.

4.2 Model performance and uncertainty

For the mountainous areas in California's Sierra Nevada, both point-scale and catchment-scale evaluations demonstrate that our NDWI-CWS generally produces better ET estimates, compared to the six other ET products. Consistent with the findings in Goulden et al. (2012), we found that the global MOD16 product significantly underestimates ET in the Mediterranean Sierra Nevada. The global-scale MODIS-based PML2 tends to overestimate ET in our study area. Similar to MOD16, PML2 does not use soil moisture to constrain ET, which can further improve ET estimates in water-limited regions (Brust et al., 2021). One of the challenges is the lack of observed global dataset of dynamic rooting-depth soil moisture (Zhang et al., 2019), particularly for deep-rooted forests that can assess deep soil moisture and groundwater (Yang et al., 2016). Though the global-scale GLEAM product uses a data assimilation method and estimates soil moisture in root-zone up to 250-cm depth using a water-balance algorithm (Martens et al., 2017), its original coarse-resolution (0.25°) data cannot capture the variability of in-situ flux-tower data in the Sierra Nevada, which has steep, complex terrain. These discrepancies deserve attention if global-scale biophysical ET products are used for regional studies and applications, particularly in Mediterranean climates where inconsistent seasonal variations between water stress and vegetation index exist but were not explicitly addressed (Chiesi et al., 2013; Maselli et al., 2014). The global-scale FLUXCOM product shows a good performance in the Sierra Nevada, e.g. the lowest RMSE for basin-scale water-balance evaluation and largest R2 value for point-scale evaluation at woody sites inside the Sierra (Tables 3 and 4), indicating that its machine-learning approach takes the advantage of flux-tower measurements at 224 sites around the world (Jung et al., 2020; Tramontana et al., 2016). At a regional scale, FLUXCOM uses only six California sites, and machine-learning approaches may be affected by the representativeness of training data (Pan et al., 2020; Zhang et al., 2023). Benefiting from the relatively dense regional data from 18 California sites, our calibrated NDWI-CWS model yielded a larger R2 than did FLUXCOM, compared to data at 18 flux towers. Additionally, our NDWI-CWS mode explicitly accounts for the important role of deep root-zone water storage in supporting vegetation ET. Similar to other above-mentioned global-scale ET products that cannot explicitly account for the water stored in deep root zones in some deep-rooted forested areas, FLUXCOM represents water availability based on a soil-water balance model with water-storage capacity being assumed up to 100 mm (O'Sullivan et al., 2020; Tramontana et al., 2016), much lower than the documented water-storage capacity in our study area (Fellows and Goulden, 2017; Goulden and Bales, 2019; McCormick et al., 2021). This may affect the global-scale FLUXCOM's performance in Mediterranean-climate California. In terms of the regional product developed for California, BESS ET showed a noticeable underestimation in mountain woody areas. This is understandable, as the BESS product focused on broader statewide values, particularly ET in irrigated agricultural croplands of California's Central Valley. Of note, different from the original CWS model, our NDWI-CWS did not explicitly address ET in croplands, which only account for 0.4% area of our mountainous Sierra Nevada. The California CECS product does not account for open-water ET, which may constrain its catchment-scale water accounting in areas with a high portion of open water. In another aspect, CECS ET is based on 30-m Landsat data, allowing fine-scale applications such as forest treatment planning and management. As data fusion techniques can combine the advantages of the high-frequency revisit cycle of MODIS data and the fine resolution of Landsat data (Chiesi et al., 2019; He et al., 2019; Yang et al., 2022), it is worth further developing our NDWI-CWS model towards the use of MODIS-Landsat-fused data in future studies.

Despite the overall promising performance of the NDWI-CWS model, there still exist some uncertainties in this study. First is the parameterization of the maximum crop coefficients. Of note, using the default crop coefficients determined in Italy for the original CWS model, we observed that our NDWI-woody modeling experiment significantly improved the woody ET estimates and catchment-scale water-balance agreement. Since crop coefficients vary across different ecosystems, soil conditions, and latitude (Allen et al., 2005; Liu et al., 2017), and precipitation and canopy water moisture also affect crop coefficients (Guerschman et al., 2009; Yebra et al., 2013), we further chose to calibrate the crop coefficients to improve NDWI-CWS model performance in our application in California's Sierra Nevada, although potentially sacrificing its general applicability.

Our automatic calibration process using California's flux-tower data across all years provides an example of model generalization for other Mediterranean-climate regions, such as the Mediterranean Basin, Central Chile, and Southwestern Australia. In these regions, vegetation relies heavily on deep root-zone water storage to adapt to the mismatch between energy and water availability. Vegetation itself can be used as an indicator of water

availability (Dralle et al., 2020), which is represented using remote-sensing NDWI for deep-rooted vegetation. Building on the original CWS model developed for Mediterranean Italy (Maselli et al., 2014, 2009), our NDWI-CWS model further provides more-accurate ET estimates for our study area, in relatively data-rich California. To obtain high-quality regional ET estimates, it is suggested to calibrate the NDWI-CWS model using local flux-tower data. We used Mediterranean-climate California as the study area to develop the NDWI-CWS model, since deep root-zone water storage is recognized as an important source of water supply during dry summers and multi-year droughts (Cui et al., 2022a; Dralle et al., 2020; Goulden and Bales, 2019; Hahm et al., 2019), and multiple regional ET datasets, relatively dense flux-tower data, and catchment-scale water-balance data are available for model evaluation. It is the best study area for assessing understanding and predictive ability for drought-vulnerable Mediterranean-climate areas. Though this study did not examine the NDWI-CWS model across the U.S., globally, or in other climate zones, a broader evaluation of the globally focused NDWI-CWS model in other data-rich regions would be very interesting and a topic for future studies.

Second, in this study, the NDWI-based AW and subsequent CWS for woody vegetation from NDWI-CWS model have larger low-bounds (0.5 and 0.75), compared to those (0 and 0.5) values based on P/PET for non-woody vegetation. Different low-bound values are based on the understanding that woody vegetation is more resistant to water stress than non-woody vegetation because their roots can access deep root-zone water storage (Paço et al., 2009; Wilschut et al., 2022; H. Xu et al., 2018). Our modeling comparisons through different settings (Expt 1-4) have supported that using NDWI-based AW and subsequent CWS is more suitable for woody vegetation. However, for applications, there may be uncertainties when evaluating water stress simply using NDWI-based (woody) versus P/PET-based (non-woody) AW and CWS, due to their different low-bound values.

Third is the uncertainty of precipitation data in high elevations of the Sierra Nevada, where systematic bias caused by gauge undercatch during snowfall may lead to precipitation underestimation (Cui et al., 2022b; Rasmussen et al., 2012). Generally, this may not raise an issue for our ET modeling, which only uses the ratio of cumulative P to PET to denote water availability. During wet winters, precipitation underestimation is relatively larger, but the PET is small, resulting in larger P/PET-based water availability. This can adequately represent that ET is not limited by available water during energy-limited winters. For hot dry summers in absence of snowfall, precipitation underestimation does not emerge. However, regarding catchment-scale water balance evaluation, precipitation underestimation may help explain the positive mean bias in our NDWI-CWS ET estimates, similar to the finding in Roche et al. (2022). In addition, given the uncertainty in precipitation (Roche et al., 2022) and streamflow data (Huang and Kadir, 2016), our NDWI-CWS ET was principally in line with catchment-scale ET estimates with R2 of 0.42. We consider this as a reasonable agreement, compared to the R2 values of 0.27-0.36 for evaluating catchment-scale ET from a hydrological model, MOD16, and PML2 in Australia (Guerschman et al., 2022).

For the original CWS model, we also found that selecting an appropriate longer duration value (180 days) in Equation 3 for woody vegetation can improve its performance of ET prediction (Text S2). However, compared to its P/PET-based water availability, NDWI-based water availability still shows a higher correlation to root-zone water storage during the high-ET summer season. Considering the important role of root-zone water storage in supporting deep-rooted vegetation during the summer growing season, we recommend using water availability based on remote-sensed NDWI data to better reflect the dynamics of root-zone water storage.

4.3 Perspectives on water resources and forest management

As one of the most uncertain water-balance components (Fisher et al., 2017; Huang and Kadir, 2016), accurate ET estimates are critical for water-yield estimates in regional headwater mountains, which are essential to downstream populations and ecosystems (Bales et al., 2006; Rohatyn et al., 2018; Viviroli et al., 2007). This is particularly important when considering dramatic disturbances (e.g. wildfire, forest thinning, afforestation, and drought-induced mortality) to mountain forests. For example, destructive wildfire significantly decreases woody ET and thus increases water yield (Q. Ma et al., 2020; Williams et al., 2022). As our NDWI-CWS model digests the MODIS-based NDVI and NDWI data, reflecting forest conditions altered by wildfire, its reliable ET monitoring can detect water-balance-component changes induced by wildfire. As an example, our ET estimates detected a large ET decrease after the 2014 King Fire in the American River basin (Figure S17). The warmer and drier condition associated with climate change is leading to wildfires of increasing severity and extent (Williams et al., 2019), and has doubled the number of trees burned globally compared to two decades ago (Tyukavina et al., 2022), increasing

the need of accurate forest ET estimates for more efficient water resources planning and management. Thus, embedding forest-disturbance-sensitive NDWI information in models provides a new opportunity to reliably monitor ET in woody forest areas under the ongoing climate warming.

Accurate woody ET estimates also enable the reliable monitoring of water deficit, which is biologically meaningful (Stephenson, 1998), spatially variable across vegetation distribution, and linked to drought-induced forest mortality (Cui et al., 2022a). Water excess stored in root-zone water storage during wet seasons and years is critical for deep-rooted forest survival in dry seasons and multi-year droughts (Goulden and Bales, 2019), buffering the temporal variability of precipitation (Baldocchi et al., 2019; Garcia and Tague, 2015; Miller et al., 2010). In an indirect approach, we suggest that NDWI-based water availability can be used to infer the temporal variability of root-zone water storage, since remote-sensed NDWI reflects forest canopy water that responds to root-zone water storage changes. Further, in a direct approach, we can continuously track root-zone water deficit and estimate root-zone water storage using the daily ET estimates from the NDWI-CWS model. Information on root-zone water storage dynamics is helpful to forest management, and much so in preparation for future megadroughts (Williams et al., 2020).

5 Conclusions

Overall, we have three main conclusions from this regional study in the relatively data-rich, Mediterranean-climate California. First, compared to different modeling experiments and products, ET estimates from our NDWI-CWS model generally agreed best with flux-tower measurements, particularly to the seven forest flux towers in the Sierra Nevada. Meanwhile, for catchment-scale ET from long-term water-balance measurements, the NDWI-CWS model outperformed others. Together, the results suggest our NDWI-CWS model provides reliable ET estimates for California's Sierra Nevada.

Second, with the improved ET estimates from our NDWI-CWS model, we further calculated the root-zone water storage including snow dynamics. We found that our NDWI-based water availability is highly correlated with deep root-zone water storage, and much so (correlation R of 0.74) during dry summers. In contrast, P/PET-based water availability shows a relatively larger correction (R of 0.66) to surface soil moisture.

Third, the superior model performance and the relationships mentioned above collectively highlight that using remote-sensing NDWI-based water availability to account for water sourced from root-zone water storage improves ET estimates in the deep-rooted woody areas (e.g. forest, woodland, and shrubland). Denoting soil moisture based on P/PET-based water availability is suitable for non-woody vegetation with shallow roots (e.g. grassland). It is recommended to explicitly account for the distinct roles of root-zone water storage and soil moisture in ET modeling. More accurate monitoring of ET and root-zone water storage can be helpful for more efficient water resources and forest management, in the context of increasing wildfire and drought risks caused by ongoing climate warming.

Acknowledgments

This research was supported by the U.S. Bureau of Reclamation WaterSMART Program (Sustain and Manage America's Resources for Tomorrow, contract No. R19AP00281), the California Department of Water Resources (No. 4600013732), California's Strategic Growth Council (CCR20021) Climate Change Research Program, the 100 Talents Plan Foundation of Sun Yat-sen University (37000-12230030), and the National Natural Science Foundation of China (42301012). Sources of all data used in this study are described in the paper. Additionally, the time-series ET product from our model is at https://snrsis.ucmerced.edu/SierraET/, which is also visualized via a dashboard at https://snrsis.ucmerced.edu/u/SierraET_Viewer. The authors also thank the editor and four reviewers for their constructive comments and suggestions.

Supplemental Material

The Supplemental Material for this article can be found below.

References

Allen, R.G., Pereira, L.S., Raes, D., Smith, M., others, 1998. Crop evapotranspiration-Guidelines for computing crop water requirements-FAO Irrigation and drainage. FAO - Food Agric. Organ. U. N. Rome 300, D05109.

Allen, R.G., Pereira, L.S., Smith, M., Raes, D., Wright, J.L., 2005. FAO-56 Dual Crop Coefficient Method for Estimating Evaporation from Soil and Application Extensions. J. Irrig. Drain. Eng. 131, 2–13. https://doi.org/10.1061/(ASCE)0733-9437(2005)131:1(2)

Ambrose, A.R., 2018. Leaf- and crown-level adjustments help giant sequoias maintain favorable water status during severe drought. For. Ecol. Manag. 11. https://doi.org/10.1016/j.foreco.2018.01.012

Anderson, L.O., Malhi, Y., Aragão, L.E.O.C., Ladle, R., Arai, E., Barbier, N., Phillips, O., 2010. Remote sensing detection of droughts in Amazonian forest canopies. New Phytol. 187, 733–750. https://doi.org/10.1111/j.1469-8137.2010.03355.x

Bai, Y., Zhang, J., Zhang, S., Koju, U.A., Yao, F., Igbawua, T., 2017. Using precipitation, vertical root distribution, and satellite-retrieved vegetation information to parameterize

water stress in a Penman-Monteith approach to evapotranspiration modeling under Mediterranean climate. J. Adv. Model. Earth Syst. 9, 168–192. https://doi.org/10.1002/2016MS000702

Baldocchi, D., Dralle, D., Jiang, C., Ryu, Y., 2019. How Much Water Is Evaporated Across California? A Multiyear Assessment Using a Biophysical Model Forced With Satellite Remote Sensing Data. Water Resour. Res. 55, 2722–2741. https://doi.org/10.1029/2018WR023884

Baldocchi, D., Falge, E., Gu, L., Olson, R., Hollinger, D., Running, S., Anthoni, P., Bernhofer, C., Davis, K., Evans, R., Fuentes, J., Goldstein, A., Katul, G., Law, B., Lee, X., Malhi, Y., Meyers, T., Munger, W., Oechel, W., U, K.T.P., Pilegaard, K., Schmid, H.P., Valentini, R., Verma, S., Vesala, T., Wilson, K., Wofsy, S., 2001. FLUXNET: A New Tool to Study the Temporal and Spatial Variability of Ecosystem-Scale Carbon Dioxide, Water Vapor, and Energy Flux Densities. Bull. Am. Meteorol. Soc. 82, 2415–2434. https://doi.org/10.1175/1520-0477(2001)082<2415:FANTTS>2.3.CO;2

Baldocchi, D.D., Xu, L., Kiang, N., 2004. How plant functional-type, weather, seasonal drought, and soil physical properties alter water and energy fluxes of an oak–grass savanna and an annual grassland. Agric. For. Meteorol. 123, 13–39. https://doi.org/10.1016/j.agrformet.2003.11.006

Bales, R., Goulden, M.L., Hunsaker, C.T., Conklin, M.H., Hartsough, P.C., O'Geen, A.T., Hopmans, J.W., Safeeq, M., 2018. Mechanisms controlling the impact of multi-year drought on mountain hydrology. Sci. Rep. 8, 690. https://doi.org/10.1038/s41598-017-19007-0

Bales, R.C., Hopmans, J.W., O'Geen, A.T., Meadows, M., Hartsough, P.C., Kirchner, P., Hunsaker, C.T., Beaudette, D., 2011. Soil Moisture Response to Snowmelt and Rainfall in a Sierra Nevada Mixed-Conifer Forest. Vadose Zone J. 10, 786–799. https://doi.org/10.2136/vzj2011.0001

Bales, R.C., Molotch, N.P., Painter, T.H., Dettinger, M., Rice, R., Dozier, J., 2006. Mountain hydrology of the western United States. Water Resour. Res. 42. https://doi.org/10.1029/2005WR004387

Bastiaanssen, W.G.M., Menenti, M., Feddes, R.A., Holtslag, A.A.M., 1998. A remote sensing surface energy balance algorithm for land (SEBAL). 1. Formulation. J. Hydrol. 212–213, 198–212. https://doi.org/10.1016/S0022-1694(98)00253-4

Battista, P., Chiesi, M., Fibbi, L., Gardin, L., Rapi, B., Romanelli, S., Romani, M., Sabatini, F., Salerni, E., Perini, C., Maselli, F., 2018. Simulation of Soil Water Content in Mediterranean Ecosystems by Biogeochemical and Remote Sensing Models. Water 10, 665. https://doi.org/10.3390/w10050665

Biederman, J.A., Scott, R.L., Bell, T.W., Bowling, D.R., Dore, S., Garatuza-Payan, J., Kolb, T.E., Krishnan, P., Krofcheck, D.J., Litvak, M.E., Maurer, G.E., Meyers, T.P., Oechel, W.C., Papuga, S.A., Ponce-Campos, G.E., Rodriguez, J.C., Smith, W.K., Vargas, R., Watts, C.J., Yepez, E.A., Goulden, M.L., 2017. CO2 exchange and evapotranspiration across dryland ecosystems of southwestern North America. Glob. Change Biol. 23, 4204–4221. https://doi.org/10.1111/gcb.13686

Bogena, H. r., Montzka, C., Huisman, J. a., Graf, A., Schmidt, M., Stockinger, M., von Hebel, C., Hendricks-Franssen, H. j., van der Kruk, J., Tappe, W., Lücke, A., Baatz, R., Bol, R., Groh, J., Pütz, T., Jakobi, J., Kunkel, R., Sorg, J., Vereecken, H., 2018. The TERENO-Rur Hydrological Observatory: A Multiscale Multi-Compartment Research Platform for the Advancement of Hydrological Science. Vadose Zone J. 17, 180055. https://doi.org/10.2136/vzj2018.03.0055

Bohn, T.J., Livneh, B., Oyler, J.W., Running, S.W., Nijssen, B., Lettenmaier, D.P., 2013. Global evaluation of MTCLIM and related algorithms for forcing of ecological and hydrological models. Agric. For. Meteorol. 176, 38–49. https://doi.org/10.1016/j.agrformet.2013.03.003

Broxton, P.,.X. Zeng, Dawson, N., 2019. Daily 4 km Gridded SWE and Snow Depth from Assimilated In-Situ and Modeled Data over the Conterminous US, Version 1. https://doi.org/10.5067/0GGPB220EX6A

Brust, C., Kimball, J.S., Maneta, M.P., Jencso, K., He, M., Reichle, R.H., 2021. Using SMAP Level-4 soil moisture to constrain MOD16 evapotranspiration over the contiguous USA. Remote Sens. Environ. 255, 112277. https://doi.org/10.1016/j.rse.2020.112277

Callahan, R.P., Riebe, C.S., Sklar, L.S., Pasquet, S., Ferrier, K.L., Hahm, W.J., Taylor, N.J., Grana, D., Flinchum, B.A., Hayes, J.L., Holbrook, W.S., 2022. Forest vulnerability to drought controlled by bedrock composition. Nat. Geosci. 1–6. https://doi.org/10.1038/s41561-022-01012-2

Cheng, M., Jiao, X., Li, B., Yu, X., Shao, M., Jin, X., 2021. Long time series of daily evapotranspiration in China based on the SEBAL model and multisource images and validation. Earth Syst. Sci. Data 13, 3995–4017. https://doi.org/10.5194/essd-13-3995-2021

Chiesi, M., Battista, P., Fibbi, L., Gardin, L., Pieri, M., Rapi, B., Romani, M., Sabatini, F., Maselli, F., 2019. Spatio-temporal fusion of NDVI data for simulating soil water content in heterogeneous Mediterranean areas. Eur. J. Remote Sens. 52, 88–95. https://doi.org/10.1080/22797254.2018.1557501

Chiesi, M., Rapi, B., Battista, P., Fibbi, L., Gozzini, B., Magno, R., Raschi, A., Maselli, F., 2013. Combination of ground and satellite data for the operational estimation of daily evapotranspiration. Eur. J. Remote Sens. 46, 675–688. https://doi.org/10.5721/EuJRS20134639

Cho, E., Jacobs, J.M., Vuyovich, C.M., 2020. The Value of Long-Term (40 years) Airborne Gamma Radiation SWE Record for Evaluating Three Observation-Based Gridded SWE Data Sets by Seasonal Snow and Land Cover Classifications. Water Resour. Res. 56, e2019WR025813. https://doi.org/10.1029/2019WR025813

Consoli, S., Vanella, D., 2014. Mapping crop evapotranspiration by integrating vegetation indices into a soil water balance model. Agric. Water Manag. 143, 71–81. https://doi.org/10.1016/j.agwat.2014.06.012

Cui, G., Bales, R., Rice, R., Anderson, M., Avanzi, F., Hartsough, P., Conklin, M., 2020. Detecting Rain–Snow-Transition Elevations in Mountain Basins Using Wireless Sensor Networks. J. Hydrometeorol. 21, 2061–2081. https://doi.org/10.1175/JHM-D-20-0028.1

Cui, G., Ma, Q., Bales, R., 2022a. Assessing multi-year-drought vulnerability in dense Mediterranean-climate forests using water-balance-based indicators. J. Hydrol. 606, 127431. https://doi.org/10.1016/j.jhydrol.2022.127431

Cui, G., Rice, R., Anderson, M., Avanzi, F., Hartsough, P., Guo, W., Conklin, M., Bales, R., 2022b. Precipitation estimates and orographic gradients using snow, temperature, and humidity measurements from a wireless-sensor network. Water Resour. Res. 58, e2021WR029954. https://doi.org/10.1029/2021WR029954

Daly, C., Halbleib, M., Smith, J.I., Gibson, W.P., Doggett, M.K., Taylor, G.H., Curtis, J., Pasteris, P.P., 2008. Physiographically sensitive mapping of climatological temperature and precipitation across the conterminous United States. Int. J. Climatol. 28, 2031–2064. https://doi.org/10.1002/joc.1688

Dralle, D.N., Hahm, W.J., Chadwick, K.D., McCormick, E., Rempe, D.M., 2021. Technical note: Accounting for snow in the estimation of root zone water storage capacity from precipitation and evapotranspiration fluxes. Hydrol. Earth Syst. Sci. 25, 2861–2867. https://doi.org/10.5194/hess-25-2861-2021

Dralle, D.N., Jesse Hahm, W., Rempe, D.M., Karst, N., Anderegg, L.D.L., Thompson, S.E., Dawson, T.E., Dietrich, W.E., 2020. Plants as sensors: vegetation response to rainfall predicts root-zone water storage capacity in Mediterranean-type climates. Environ. Res. Lett. 15, 104074. https://doi.org/10.1088/1748-9326/abb10b

Duan, Q., Sorooshian, S., Gupta, V., 1992. Effective and efficient global optimization for conceptual rainfall-runoff models. Water Resour. Res. 28, 1015–1031. https://doi.org/10.1029/91WR02985

Eamus, D., Prior, L., 2001. Ecophysiology of trees of seasonally dry tropics: Comparisons among phenologies, in: Advances in Ecological Research. Academic Press, pp. 113–197. https://doi.org/10.1016/S0065-2504(01)32012-3

Falcone, J.A., 2017. U.S. Geological Survey GAGES-II time series data from consistent sources of land use, water use, agriculture, timber activities, dam removals, and other historical anthropogenic influences. https://doi.org/10.5066/F7HQ3XS4

Falcone, J.A., 2011. GAGES-II: Geospatial Attributes of Gages for Evaluating Streamflow (Report). Reston, VA. https://doi.org/10.3133/70046617

Feldman, A.F., Short Gianotti, D.J., Dong, J., Akbar, R., Crow, W.T., McColl, K.A., Konings, A.G., Nippert, J.B., Tumber-Dávila, S.J., Holbrook, N.M., Rockwell, F.E., Scott, R.L., Reichle, R.H., Chatterjee, A., Joiner, J., Poulter, B., Entekhabi, D., 2023. Remotely Sensed Soil Moisture Can Capture Dynamics Relevant to Plant Water Uptake. Water Resour. Res. 59, e2022WR033814. https://doi.org/10.1029/2022WR033814

Fellows, A.W., Goulden, M.L., 2017. Mapping and understanding dry season soil water drawdown by California montane vegetation. Ecohydrology 10, e1772. https://doi.org/10.1002/eco.1772

Fisher, J.B., Melton, F., Middleton, E., Hain, C., Anderson, M., Allen, R., McCabe, M.F., Hook, S., Baldocchi, D., Townsend, P.A., Kilic, A., Tu, K., Miralles, D.D., Perret, J., Lagouarde, J.-P., Waliser, D., Purdy, A.J., French, A., Schimel, D., Famiglietti, J.S., Stephens, G., Wood, E.F., 2017. The future of evapotranspiration: Global requirements for ecosystem functioning, carbon and climate feedbacks, agricultural management, and water resources. Water Resour. Res. 53, 2618–2626. https://doi.org/10.1002/2016WR020175

Gaertner, B.A., Zegre, N., Warner, T., Fernandez, R., He, Y., Merriam, E.R., 2019. Climate, forest growing season, and evapotranspiration changes in the central Appalachian Mountains, USA. Sci. Total Environ. 650, 1371–1381. https://doi.org/10.1016/j.scitotenv.2018.09.129

Gao, B., 1996. NDWI—A normalized difference water index for remote sensing of vegetation liquid water from space. Remote Sens. Environ. 58, 257–266. https://doi.org/10.1016/S0034-4257(96)00067-3

Gao, Y., Yu, G., Yan, H., Zhu, X., Li, S., Wang, Q., Zhang, J., Wang, Y., Li, Y., Zhao, L., Shi, P., 2014. A MODIS-based Photosynthetic Capacity Model to estimate gross primary production in Northern China and the Tibetan Plateau. Remote Sens. Environ. 148, 108–118. https://doi.org/10.1016/j.rse.2014.03.006

Garcia, E.S., Tague, C.L., 2015. Subsurface storage capacity influences climate–evapotranspiration interactions in three western United States catchments. Hydrol. Earth Syst. Sci. 19, 4845–4858. https://doi.org/10.5194/hess-19-4845-2015

Glenn, E.P., Nagler, P.L., Huete, A.R., 2010. Vegetation Index Methods for Estimating Evapotranspiration by Remote Sensing. Surv. Geophys. 31, 531–555. https://doi.org/10.1007/s10712-010-9102-2

Goldstein, A.H., Hultman, N.E., Fracheboud, J.M., Bauer, M.R., Panek, J.A., Xu, M., Qi, Y., Guenther, A.B., Baugh, W., 2000. Effects of climate variability on the carbon dioxide, water, and sensible heat fluxes above a ponderosa pine plantation in the Sierra Nevada (CA). Agric. For. Meteorol. 101, 113–129. https://doi.org/10.1016/S0168-1923(99)00168-9

Goodwin, N.R., Coops, N.C., Wulder, M.A., Gillanders, S., Schroeder, T.A., Nelson, T., 2008. Estimation of insect infestation dynamics using a temporal sequence of Landsat data. Remote Sens. Environ. 112, 3680–3689. https://doi.org/10.1016/j.rse.2008.05.005

Gorelick, N., Hancher, M., Dixon, M., Ilyushchenko, S., Thau, D., Moore, R., 2017. Google Earth Engine: Planetary-scale geospatial analysis for everyone. Remote Sens. Environ., Big Remotely Sensed Data: tools, applications and experiences 202, 18–27. https://doi.org/10.1016/j.rse.2017.06.031

Goulden, M.L., Anderson, R.G., Bales, R.C., Kelly, A.E., Meadows, M., Winston, G.C., 2012. Evapotranspiration along an elevation gradient in California's Sierra Nevada. J. Geophys. Res. Biogeosciences 117. https://doi.org/10.1029/2012JG002027

Goulden, M.L., Bales, R.C., 2019. California forest die-off linked to multi-year deep soil drying in 2012–2015 drought. Nat. Geosci. 12, 632–637. https://doi.org/10.1038/s41561-019-0388-5

Goulden, M.L., Bales, R.C., 2014. Mountain runoff vulnerability to increased evapotranspiration with vegetation expansion. Proc. Natl. Acad. Sci. 111, 14071–14075. https://doi.org/10.1073/pnas.1319316111

Guerschman, J.P., McVicar, T.R., Vleeshower, J., Van Niel, T.G., Peña-Arancibia, J.L., Chen, Y., 2022. Estimating actual evapotranspiration at field-to-continent scales by calibrating the CMRSET algorithm with MODIS, VIIRS, Landsat and Sentinel-2 data. J. Hydrol. 605, 127318. https://doi.org/10.1016/j.jhydrol.2021.127318

Guerschman, J.P., Van Dijk, A.I.J.M., Mattersdorf, G., Beringer, J., Hutley, L.B., Leuning, R., Pipunic, R.C., Sherman, B.S., 2009. Scaling of potential evapotranspiration with MODIS data reproduces flux observations and catchment water balance observations across Australia. J. Hydrol. 369, 107–119. https://doi.org/10.1016/j.jhydrol.2009.02.013

Guo, W., Safeeq, M., Liu, H., Wu, X., Cui, G., Ma, Q., Goulden, M.L., Lindeskog, M., Bales, R.C., 2022. Mechanisms Controlling Carbon Sinks in Semi-Arid Mountain Ecosystems. Glob. Biogeochem. Cycles 36, e2021GB007186. https://doi.org/10.1029/2021GB007186

Hahm, W.J., Dralle, D.N., Rempe, D.M., Bryk, A.B., Thompson, S.E., Dawson, T.E., Dietrich, W.E., 2019. Low Subsurface Water Storage Capacity Relative to Annual Rainfall Decouples Mediterranean Plant Productivity and Water Use From Rainfall Variability. Geophys. Res. Lett. 46, 6544–6553. https://doi.org/10.1029/2019GL083294

Hardisky, M.A., Klemas, V., Smart, R., 1983. The influence of soil salinity, growth form, and leaf moisture on-the spectral radiance of. Photogramm Eng Remote Sens 49, 77–83.

Harrison, A.T., Small, E., Mooney, H.A., 1971. Drought Relationships and Distribution of Two Mediterranean-Climate California Plant Communities. Ecology 52, 869–875. https://doi.org/10.2307/1936035

He, M., Kimball, J.S., Yi, Y., Running, S.W., Guan, K., Moreno, A., Wu, X., Maneta, M., 2019. Satellite data-driven modeling of field scale evapotranspiration in croplands using the MOD16 algorithm framework. Remote Sens. Environ. 230, 111201. https://doi.org/10.1016/j.rse.2019.05.020

Henn, B., Musselman, K.N., Lestak, L., Ralph, F.M., Molotch, N.P., 2020. Extreme Runoff Generation From Atmospheric River Driven Snowmelt During the 2017 Oroville Dam Spillways Incident. Geophys. Res. Lett. 47, e2020GL088189. https://doi.org/10.1029/2020GL088189

Herrero, J., Polo, M.J., 2016. Evaposublimation from the snow in the Mediterranean mountains of Sierra Nevada (Spain). The Cryosphere 10, 2981–2998. https://doi.org/10.5194/tc-10-2981-2016

Hong, S., Hendrickx, J.M.H., Borchers, B., 2009. Up-scaling of SEBAL derived evapotranspiration maps from Landsat (30m) to MODIS (250m) scale. J. Hydrol. 370, 122–138. https://doi.org/10.1016/j.jhydrol.2009.03.002

Huang, G., Kadir, T., 2016. Estimates of natural and unimpaired flows for the Central Valley of California: Water years 1922–2014 (No. DWR-1384). California Department of Water Resources, Sacramento, CA, USA.

Ishikawa, C.M., Bledsoe, C.S., 2000. Seasonal and diurnal patterns of soil water potential in the rhizosphere of blue oaks: evidence for hydraulic lift. Oecologia 125, 459–465. https://doi.org/10.1007/s004420000470

Jackson, R.B., Canadell, J., Ehleringer, J.R., Mooney, H.A., Sala, O.E., Schulze, E.D., 1996. A global analysis of root distributions for terrestrial biomes. Oecologia 108, 389–411. https://doi.org/10.1007/BF00333714

Jensen, M.E., Haise, H.R., 1963. Estimating Evapotranspiration from Solar Radiation. J. Irrig. Drain. Div. 89, 15–41. https://doi.org/10.1061/JRCEA4.0000287

Jiang, C., Ryu, Y., 2016. Multi-scale evaluation of global gross primary productivity and evapotranspiration products derived from Breathing Earth System Simulator (BESS). Remote Sens. Environ. 186, 528–547. https://doi.org/10.1016/j.rse.2016.08.030

Jiménez-Muñoz, J.C., Sobrino, J.A., Plaza, A., Guanter, L., Moreno, J., Martinez, P., 2009. Comparison Between Fractional Vegetation Cover Retrievals from Vegetation Indices and Spectral Mixture Analysis: Case Study of PROBA/CHRIS Data Over an Agricultural Area. Sensors 9, 768–793. https://doi.org/10.3390/s90200768

Jin, S., Sader, S.A., 2005. Comparison of time series tasseled cap wetness and the normalized difference moisture index in detecting forest disturbances. Remote Sens. Environ. 94, 364–372. https://doi.org/10.1016/j.rse.2004.10.012

Jones, D.P., Graham, R.C., 1993. Water-Holding Characteristics of Weathered Granitic Rock in Chaparral and Forest Ecosystems. Soil Sci. Soc. Am. J. 57, 256–261. https://doi.org/10.2136/sssaj1993.03615995005700010044x

Jung, M., Koirala, S., Weber, U., Ichii, K., Gans, F., Camps-Valls, G., Papale, D., Schwalm, C., Tramontana, G., Reichstein, M., 2019. The FLUXCOM ensemble of global land-atmosphere energy fluxes. Sci. Data 6, 74. https://doi.org/10.1038/s41597-019-0076-8

Jung, M., Reichstein, M., Bondeau, A., 2009. Towards global empirical upscaling of FLUXNET eddy covariance observations: validation of a model tree ensemble approach using a biosphere model. Biogeosciences 6, 2001–2013. https://doi.org/10.5194/bg-6-2001-2009

Jung, M., Reichstein, M., Ciais, P., Seneviratne, S.I., Sheffield, J., Goulden, M.L., Bonan, G., Cescatti, A., Chen, J., de Jeu, R., Dolman, A.J., Eugster, W., Gerten, D., Gianelle, D., Gobron, N., Heinke, J., Kimball, J., Law, B.E., Montagnani, L., Mu, Q., Mueller, B., Oleson, K., Papale, D., Richardson, A.D., Roupsard, O., Running, S., Tomelleri, E., Viovy, N., Weber, U., Williams, C., Wood,

E., Zaehle, S., Zhang, K., 2010. Recent decline in the global land evapotranspiration trend due to limited moisture supply. Nature 467, 951–954. https://doi.org/10.1038/nature09396

Jung, M., Schwalm, C., Migliavacca, M., Walther, S., Camps-Valls, G., Koirala, S., Anthoni, P., Besnard, S., Bodesheim, P., Carvalhais, N., Chevallier, F., Gans, F., Goll, D.S., Haverd, V., Köhler, P., Ichii, K., Jain, A.K., Liu, J., Lombardozzi, D., Nabel, J.E.M.S., Nelson, J.A., O'Sullivan, M., Pallandt, M., Papale, D., Peters, W., Pongratz, J., Rödenbeck, C., Sitch, S., Tramontana, G., Walker, A., Weber, U., Reichstein, M., 2020. Scaling carbon fluxes from eddy covariance sites to globe: synthesis and evaluation of the FLUXCOM approach. Biogeosciences 17, 1343–1365. https://doi.org/10.5194/bg-17-1343-2020

Kelly, A.E., Goulden, M.L., 2016. A montane Mediterranean climate supports year-round photosynthesis and high forest biomass. Tree Physiol. 36, 459–468. https://doi.org/10.1093/treephys/tpv131

Kimball, J.S., Running, S.W., Nemani, R., 1997. An improved method for estimating surface humidity from daily minimum temperature. Agric. For. Meteorol. 85, 87–98. https://doi.org/10.1016/S0168-1923(96)02366-0

Klos, P.Z., Goulden, M.L., Riebe, C.S., Tague, C.L., O'Geen, A.T., Flinchum, B.A., Safeeq, M., Conklin, M.H., Hart, S.C., Berhe, A.A., Hartsough, P.C., Holbrook, W.S., Bales, R.C., 2018. Subsurface plant-accessible water in mountain ecosystems with a Mediterranean climate. WIREs Water 5, e1277. https://doi.org/10.1002/wat2.1277

Krishnan, P., Meyers, T.P., Scott, R.L., Kennedy, L., Heuer, M., 2012. Energy exchange and evapotranspiration over two temperate semi-arid grasslands in North America. Agric. For. Meteorol., Land-Atmosphere Interactions: Advances in Measurement, Analysis, and Modeling – A Tribute to T. Andrew Black 153, 31–44. https://doi.org/10.1016/j.agrformet.2011.09.017

Kurc, S.A., Small, E.E., 2004. Dynamics of evapotranspiration in semiarid grassland and shrubland ecosystems during the summer monsoon season, central New Mexico. Water Resour. Res. 40. https://doi.org/10.1029/2004WR003068

Lewis, D.C., Burgy, R.H., 1964. The Relationship between oak tree roots and groundwater in fractured rock as determined by tritium tracing. J. Geophys. Res. 69, 2579–2588. https://doi.org/10.1029/JZ069i012p02579

Li, X., Liu, S., Xiao, Q., Ma, M., Jin, R., Che, T., Wang, W., Hu, X., Xu, Z., Wen, J., Wang, L., 2017. A multiscale dataset for understanding complex eco-hydrological processes in a heterogeneous oasis system. Sci. Data 4, 170083. https://doi.org/10.1038/sdata.2017.83

Liu, C., Sun, G., McNulty, S.G., Noormets, A., Fang, Y., 2017. Environmental controls on seasonal ecosystem evapotranspiration/potential evapotranspiration ratio as determined by the global eddy flux measurements. Hydrol. Earth Syst. Sci. 21, 311–322. https://doi.org/10.5194/hess-21-311-2017

Liu, M., Zhang, B., He, X., 2022. Climate Rather Than Vegetation Changes Dominate Changes in Effective Vegetation Available Water Capacity. Water Resour. Res. 58. https://doi.org/10.1029/2021WR030319

Liu, W., Wang, L., Zhou, J., Li, Y., Sun, F., Fu, G., Li, X., Sang, Y.-F., 2016. A worldwide evaluation of basin-scale evapotranspiration estimates against the water balance method. J. Hydrol. 538, 82–95. https://doi.org/10.1016/j.jhydrol.2016.04.006

Ma, N., Szilagyi, J., Jozsa, J., 2020. Benchmarking large-scale evapotranspiration estimates: A perspective from a calibration-free complementary relationship approach and FLUXCOM. J. Hydrol. 590, 125221. https://doi.org/10.1016/j.jhydrol.2020.125221

Ma, N., Szilagyi, J., Zhang, Y., 2021. Calibration-Free Complementary Relationship Estimates Terrestrial Evapotranspiration Globally. Water Resour. Res. 57, e2021WR029691. https://doi.org/10.1029/2021WR029691

Ma, Q., Bales, R.C., Rungee, J., Conklin, M.H., Collins, B.M., Goulden, M.L., 2020. Wildfire controls on evapotranspiration in California's Sierra Nevada. J. Hydrol. 590, 125364. https://doi.org/10.1016/j.jhydrol.2020.125364

Martens, B., Miralles, D.G., Lievens, H., van der Schalie, R., de Jeu, R.A.M., Fernández-Prieto, D., Beck, H.E., Dorigo, W.A., Verhoest, N.E.C., 2017. GLEAM v3: satellite-based land evaporation and root-zone soil moisture. Geosci. Model Dev. 10, 1903–1925. https://doi.org/10.5194/gmd-10-1903-2017

Martínez, B., Sánchez-Ruiz, S., Campos-Taberner, M., García-Haro, F.J., Gilabert, M.A., 2022. Exploring Ecosystem Functioning in Spain with Gross and Net Primary Production Time Series. Remote Sens. 14, 1310. https://doi.org/10.3390/rs14061310

Maselli, F., Argenti, G., Chiesi, M., Angeli, L., Papale, D., 2013. Simulation of grassland productivity by the combination of ground and satellite data. Agric. Ecosyst. Environ. 165, 163–172. https://doi.org/10.1016/j.agee.2012.11.006

Maselli, F., Papale, D., Chiesi, M., Matteucci, G., Angeli, L., Raschi, A., Seufert, G., 2014. Operational monitoring of daily evapotranspiration by the combination of MODIS NDVI and ground meteorological data: Application and evaluation in Central Italy. Remote Sens. Environ. 152, 279–290. https://doi.org/10.1016/j.rse.2014.06.021

Maselli, F., Papale, D., Puletti, N., Chirici, G., Corona, P., 2009. Combining remote sensing and ancillary data to monitor the gross productivity of water-limited forest ecosystems. Remote Sens. Environ. 113, 657–667. https://doi.org/10.1016/j.rse.2008.11.008

Maurer, T., Avanzi, F., Glaser, S.D., Bales, R.C., 2022. Drivers of drought-induced shifts in the water balance through a Budyko approach. Hydrol. Earth Syst. Sci. 26, 589–607. https://doi.org/10.5194/hess-26-589-2022

Maxwell, R.M., Condon, L.E., 2016. Connections between groundwater flow and transpiration partitioning. Science 353, 377–380. https://doi.org/10.1126/science.aaf7891

McCormick, E.L., Dralle, D.N., Hahm, W.J., Tune, A.K., Schmidt, L.M., Chadwick, K.D., Rempe, D.M., 2021. Widespread woody plant use of water stored in bedrock. Nature 597, 225–229. https://doi.org/10.1038/s41586-021-03761-3

Michel, D., Jiménez, C., Miralles, D.G., Jung, M., Hirschi, M., Ershadi, A., Martens, B., McCabe, M.F., Fisher, J.B., Mu, Q., Seneviratne, S.I., Wood, E.F., Fernández-Prieto, D., 2016. The WACMOS-ET project; Part 1: Tower-scale evaluation of four remote-sensing-based evapotranspiration algorithms. Hydrol. Earth Syst. Sci. 20, 803–822. https://doi.org/10.5194/hess-20-803-2016

Miguez-Macho, G., Fan, Y., 2021. Spatiotemporal origin of soil water taken up by vegetation. Nature 1–5. https://doi.org/10.1038/s41586-021-03958-6

Miller, G.R., Chen, X., Rubin, Y., Ma, S., Baldocchi, D.D., 2010. Groundwater uptake by woody vegetation in a semiarid oak savanna. Water Resour. Res. 46. https://doi.org/10.1029/2009WR008902

Miralles, D.G., Holmes, T.R.H., De Jeu, R. a. M., Gash, J.H., Meesters, A.G.C.A., Dolman, A.J., 2011. Global land-surface evaporation estimated from satellite-based observations. Hydrol. Earth Syst. Sci. 15, 453–469. https://doi.org/10.5194/hess-15-453-2011

Mu, Q., Heinsch, F.A., Zhao, M., Running, S.W., 2007. Development of a global evapotranspiration algorithm based on MODIS and global meteorology data. Remote Sens. Environ. 111, 519–536. https://doi.org/10.1016/j.rse.2007.04.015

Mu, Q., Zhao, M., Running, S.W., 2011. Improvements to a MODIS global terrestrial evapotranspiration algorithm. Remote Sens. Environ. 115, 1781–1800. https://doi.org/10.1016/j.rse.2011.02.019

Novick, K.A., Biederman, J.A., Desai, A.R., Litvak, M.E., Moore, D.J.P., Scott, R.L., Torn, M.S., 2018. The AmeriFlux network: A coalition of the willing. Agric. For. Meteorol. 249, 444–456. https://doi.org/10.1016/j.agrformet.2017.10.009

Oki, T., Kanae, S., 2006. Global Hydrological Cycles and World Water Resources. Science 313, 1068–1072. https://doi.org/10.1126/science.1128845

O'Sullivan, M., Smith, W.K., Sitch, S., Friedlingstein, P., Arora, V.K., Haverd, V., Jain, A.K., Kato, E., Kautz, M., Lombardozzi, D., Nabel, J.E.M.S., Tian, H., Vuichard, N., Wiltshire, A., Zhu, D., Buermann, W., 2020. Climate‐Driven Variability and Trends in Plant Productivity Over Recent Decades Based on Three Global Products. Glob. Biogeochem. Cycles 34, e2020GB006613. https://doi.org/10.1029/2020GB006613

Paço, T.A., David, T.S., Henriques, M.O., Pereira, J.S., Valente, F., Banza, J., Pereira, F.L., Pinto, C., David, J.S., 2009. Evapotranspiration from a Mediterranean evergreen oak savannah: The role of trees and pasture. J. Hydrol. 369, 98–106. https://doi.org/10.1016/j.jhydrol.2009.02.011

Pan, S., Pan, N., Tian, H., Friedlingstein, P., Sitch, S., Shi, H., Arora, V.K., Haverd, V., Jain, A.K., Kato, E., Lienert, S., Lombardozzi, D., Nabel, J.E.M.S., Ottlé, C., Poulter, B., Zaehle, S., Running, S.W., 2020. Evaluation of global terrestrial evapotranspiration using state-of-the-art approaches in remote sensing, machine learning and land surface modeling. Hydrol. Earth Syst. Sci. 24, 1485–1509. https://doi.org/10.5194/hess-24-1485-2020

Pirmoradian, R., Hashemi, H., Fayne, J., 2022. Performance evaluation of IMERG and TMPA daily precipitation products over CONUS (2000–2019). Atmospheric Res. 279, 106389. https://doi.org/10.1016/j.atmosres.2022.106389

Poyatos, R., Granda, V., Flo, V., Adams, M.A., Adorján, B., Aguadé, D., Aidar, M.P.M., Allen, S., Alvarado-Barrientos, M.S., Anderson-Teixeira, K.J., Aparecido, L.M., Arain, M.A., Aranda, I., Asbjornsen, H., Baxter, R., Beamesderfer, E., Berry, Z.C., Berveiller, D., Blakely, B., Boggs, J., Bohrer, G., Bolstad, P.V., Bonal, D., Bracho, R., Brito, P., Brodeur, J., Casanoves, F., Chave, J., Chen, H., Cisneros, C., Clark, K., Cremonese, E., Dang, H., David, J.S., David, T.S., Delpierre, N., Desai, A.R., Do, F.C., Dohnal, M., Domec, J.-C., Dzikiti, S., Edgar, C., Eichstaedt, R., El-Madany, T.S., Elbers, J., Eller, C.B., Euskirchen, E.S., Ewers, B., Fonti, P., Forner, A., Forrester, D.I., Freitas, H.C., Galvagno, M., Garcia-Tejera, O., Ghimire, C.P., Gimeno, T.E., Grace, J., Granier, A., Griebel, A., Guangyu, Y., Gush, M.B., Hanson, P.J., Hasselquist, N.J., Heinrich, I., Hernandez-Santana, V., Herrmann, V., Hölttä, T., Holwerda, F., Irvine, J., Isarangkool Na Ayutthaya, S., Jarvis, P.G., Jochheim, H., Joly, C.A., Kaplick, J., Kim, H.S., Klemedtsson, L., Kropp, H., Lagergren, F., Lane, P., Lang, P., Lapenas, A., Lechuga, V., Lee, M., Leuschner, C., Limousin, J.-M., Linares, J.C., Linderson, M.-L., Lindroth, A., Llorens, P., López-Bernal, Á., Loranty, M.M., Lüttschwager, D., Macinnis-Ng, C., Maréchaux, I., Martin, T.A., Matheny, A., McDowell, N., McMahon, S., Meir, P., Mészáros, I., Migliavacca, M., Mitchell, P., Mölder, M., Montagnani, L., Moore, G.W., Nakada, R., Niu, F., Nolan, R.H., Norby, R., Novick, K., Oberhuber, W., Obojes, N., Oishi, A.C., Oliveira, R.S., Oren, R., Ourcival, J.-M., Paljakka, T., Perez-Priego, O., Peri, P.L., Peters, R.L., Pfautsch, S., Pockman, W.T., Preisler, Y., Rascher, K., Robinson, G., Rocha, H., Rocheteau, A., Röll, A., Rosado, B.H.P., Rowland, L., Rubtsov, A.V., Sabaté, S., Salmon, Y., Salomón, R.L., Sánchez-Costa, E., Schäfer, K.V.R., Schuldt, B., Shashkin, A., Stahl, C., Stojanović, M., Suárez, J.C., Sun, G., Szatniewska, J., Tatarinov, F., Tesař, M., Thomas, F.M., Tor-ngern, P., Urban, J., Valladares, F., van der Tol, C., van Meerveld, I., Varlagin, A., Voigt, H., Warren, J., Werner, C., Werner, W., Wieser, G., Wingate, L., Wullschleger, S., Yi, K., Zweifel, R., Steppe, K., Mencuccini, M., Martínez-Vilalta, J., 2021. Global transpiration data from sap flow measurements: the SAPFLUXNET database. Earth Syst. Sci. Data 13, 2607–2649. https://doi.org/10.5194/essd-13-2607-2021

Priestley, C.H.B., Taylor, R.J., 1972. On the Assessment of Surface Heat Flux and Evaporation Using Large-Scale Parameters. Mon. Weather Rev. 100, 81–92.

https://doi.org/10.1175/1520-0493(1972)100<0081:OTAOSH>2.3.CO;2
Purdy, A.J., Fisher, J.B., Goulden, M.L., Colliander, A., Halverson, G., Tu, K., Famiglietti, J.S., 2018. SMAP soil moisture improves global evapotranspiration. Remote Sens. Environ. 219, 1–14. https://doi.org/10.1016/j.rse.2018.09.023
Rao, L.Y., G. Sun, C. R. Ford, J. M. Vose, 2011. Modeling Potential Evapotranspiration of Two Forested Watersheds in the Southern Appalachians. Trans. ASABE 54, 2067–2078. https://doi.org/10.13031/2013.40666
Rasmussen, R., Baker, B., Kochendorfer, J., Meyers, T., Landolt, S., Fischer, A.P., Black, J., Thériault, J.M., Kucera, P., Gochis, D., Smith, C., Nitu, R., Hall, M., Ikeda, K., Gutmann, E., 2012. How Well Are We Measuring Snow: The NOAA/FAA/NCAR Winter Precipitation Test Bed. Bull. Am. Meteorol. Soc. 93, 811–829. https://doi.org/10.1175/BAMS-D-11-00052.1
Rempe, D.M., Dietrich, W.E., 2018. Direct observations of rock moisture, a hidden component of the hydrologic cycle. Proc. Natl. Acad. Sci. 115, 2664–2669. https://doi.org/10.1073/pnas.1800141115
Roche, J.W., Ma, Q., Rungee, J., Bales, R.C., 2020. Evapotranspiration Mapping for Forest Management in California's Sierra Nevada. Front. For. Glob. Change 3, 69. https://doi.org/10.3389/ffgc.2020.00069
Roche, J.W., Wilson, K.N., Ma, Q., Bales, R.C., 2022. Water balance for gaged watersheds in the Central Sierra Nevada, California and Nevada, United States. Front. For. Glob. Change 5, 861711. https://doi.org/10.3389/ffgc.2022.861711
Rodell, M., Famiglietti, J.S., Chen, J., Seneviratne, S.I., Viterbo, P., Holl, S., Wilson, C.R., 2004. Basin scale estimates of evapotranspiration using GRACE and other observations. Geophys. Res. Lett. 31. https://doi.org/10.1029/2004GL020873
Rohatyn, S., Rotenberg, E., Ramati, E., Tatarinov, F., Tas, E., Yakir, D., 2018. Differential Impacts of Land Use and Precipitation on "Ecosystem Water Yield." Water Resour. Res. 54, 5457–5470. https://doi.org/10.1029/2017WR022267
Rosenberry, D.O., Winter, T.C., Buso, D.C., Likens, G.E., 2007. Comparison of 15 evaporation methods applied to a small mountain lake in the northeastern USA. J. Hydrol. 340, 149–166. https://doi.org/10.1016/j.jhydrol.2007.03.018
Rungee, J., Bales, R., Goulden, M., 2019. Evapotranspiration response to multiyear dry periods in the semiarid western United States. Hydrol. Process. 33, 182–194. https://doi.org/10.1002/hyp.13322
Running, S., Mu, Q., Zhao, M., 2017. MOD16A2 MODIS/Terra Net Evapotranspiration 8-Day L4 Global 500m SIN Grid V006. NASA EOSDIS Land Process. DAAC. https://doi.org/10.5067/MODIS/MOD16A2.006
Sadeghi, M., Hatch, T., Huang, G., Bandara, U., Ghorbani, A., Dogrul, E.C., 2022. Estimating soil water flux from single-depth soil moisture data. J. Hydrol. 610, 127999. https://doi.org/10.1016/j.jhydrol.2022.127999
Schenk, H.J., Jackson, R.B., 2005. Mapping the global distribution of deep roots in relation to climate and soil characteristics. Geoderma, Deep regolith: exploring the lower reaches of soil 126, 129–140. https://doi.org/10.1016/j.geoderma.2004.11.018
Sexstone, G.A., Clow, D.W., Fassnacht, S.R., Liston, G.E., Hiemstra, C.A., Knowles, J.F., Penn, C.A., 2018. Snow Sublimation in Mountain Environments and Its Sensitivity to Forest Disturbance and Climate Warming. Water Resour. Res. 54, 1191–1211. https://doi.org/10.1002/2017WR021172
Sriwongsitanon, N., Gao, H., Savenije, H.H.G., Maekan, E., Saengsawang, S., Thianpopirug, S., 2016. Comparing the Normalized Difference Infrared Index (NDII) with root zonestorage in a lumped conceptual model. Hydrol. Earth Syst. Sci. 20, 3361–3377. https://doi.org/10.5194/hess-20-3361-2016
Stephenson, N., 1998. Actual evapotranspiration and deficit: biologically meaningful correlates of vegetation distribution across spatial scales. J. Biogeogr. 25, 855–870. https://doi.org/10.1046/j.1365-2699.1998.00233.x
Stocker, B.D., Tumber-Dávila, S.J., Konings, A.G., Anderson, M.C., Hain, C., Jackson, R.B., 2023. Global patterns of water storage in the rooting zones of vegetation. Nat. Geosci. 1–7. https://doi.org/10.1038/s41561-023-01125-2
Sun, L., Liang, S., Yuan, W., Chen, Z., 2013. Improving a Penman–Monteith evapotranspiration model by incorporating soil moisture control on soil evaporation in semiarid areas. Int. J. Digit. Earth 6, 134–156. https://doi.org/10.1080/17538947.2013.783635
Tague, C., 2022. The bedrock of forest drought. Nat. Geosci. 1–2. https://doi.org/10.1038/s41561-022-01015-z
Taylor, K.E., 2001. Summarizing multiple aspects of model performance in a single diagram. J. Geophys. Res. Atmospheres 106, 7183–7192. https://doi.org/10.1029/2000JD900719
Teuling, A.J., Seneviratne, S.I., Stöckli, R., Reichstein, M., Moors, E., Ciais, P., Luyssaert, S., van den Hurk, B., Ammann, C., Bernhofer, C., Dellwik, E., Gianelle, D., Gielen, B., Grünwald, T., Klumpp, K., Montagnani, L., Moureaux, C., Sottocornola, M., Wohlfahrt, G., 2010. Contrasting response of European forest and grassland energy exchange to heatwaves. Nat. Geosci. 3, 722–727. https://doi.org/10.1038/ngeo950
Teuling, A.J., Seneviratne, S.I., Williams, C., Troch, P.A., 2006. Observed timescales of evapotranspiration response to soil moisture. Geophys. Res. Lett. 33. https://doi.org/10.1029/2006GL028178
Teuling, A.J., Van Loon, A.F., Seneviratne, S.I., Lehner, I., Aubinet, M., Heinesch, B., Bernhofer, C., Grünwald, T., Prasse, H., Spank, U., 2013. Evapotranspiration amplifies European summer drought. Geophys. Res. Lett. 40, 2071–2075. https://doi.org/10.1002/grl.50495
Thornton, P.E., Hasenauer, H., White, M.A., 2000. Simultaneous estimation of daily solar radiation and humidity from observed temperature and precipitation: an application over complex terrain in Austria. Agric. For.

Meteorol. 104, 255–271. https://doi.org/10.1016/S0168-1923(00)00170-2

Tramontana, G., Jung, M., Schwalm, C.R., Ichii, K., Camps-Valls, G., Ráduly, B., Reichstein, M., Arain, M.A., Cescatti, A., Kiely, G., Merbold, L., Serrano-Ortiz, P., Sickert, S., Wolf, S., Papale, D., 2016. Predicting carbon dioxide and energy fluxes across global FLUXNET sites with regression algorithms. Biogeosciences 13, 4291–4313. https://doi.org/10.5194/bg-13-4291-2016

Trujillo, E., Molotch, N.P., Goulden, M.L., Kelly, A.E., Bales, R.C., 2012. Elevation-dependent influence of snow accumulation on forest greening. Nat. Geosci. 5, 705–709. https://doi.org/10.1038/ngeo1571

Twine, T.E., Kustas, W.P., Norman, J.M., Cook, D.R., Houser, P.R., Meyers, T.P., Prueger, J.H., Starks, P.J., Wesely, M.L., 2000. Correcting eddy-covariance flux underestimates over a grassland. Agric. For. Meteorol. 103, 279–300. https://doi.org/10.1016/S0168-1923(00)00123-4

Tyukavina, A., Potapov, P., Hansen, M.C., Pickens, A.H., Stehman, S.V., Turubanova, S., Parker, D., Zalles, V., Lima, A., Kommareddy, I., Song, X.-P., Wang, L., Harris, N., 2022. Global Trends of Forest Loss Due to Fire From 2001 to 2019. Front. Remote Sens. 3. https://doi.org/10.3389/frsen.2022.825190

Van Gunst, K.J., Weisberg, P.J., Yang, J., Fan, Y., 2016. Do denser forests have greater risk of tree mortality: A remote sensing analysis of density-dependent forest mortality. For. Ecol. Manag., Special Section: Forests, Roots and Soil Carbon 359, 19–32. https://doi.org/10.1016/j.foreco.2015.09.032

Vinukollu, R.K., Wood, E.F., Ferguson, C.R., Fisher, J.B., 2011. Global estimates of evapotranspiration for climate studies using multi-sensor remote sensing data: Evaluation of three process-based approaches. Remote Sens. Environ. 115, 801–823. https://doi.org/10.1016/j.rse.2010.11.006

Viviroli, D., Dürr, H.H., Messerli, B., Meybeck, M., Weingartner, R., 2007. Mountains of the world, water towers for humanity: Typology, mapping, and global significance. Water Resour. Res. 43. https://doi.org/10.1029/2006WR005653

Viviroli, D., Weingartner, R., 2004. The hydrological significance of mountains: from regional to global scale. Hydrol. Earth Syst. Sci. 8, 1017–1030. https://doi.org/10.5194/hess-8-1017-2004

Wang, K., Dickinson, R.E., 2012. A review of global terrestrial evapotranspiration: Observation, modeling, climatology, and climatic variability. Rev. Geophys. 50. https://doi.org/10.1029/2011RG000373

Wang-Erlandsson, L., Bastiaanssen, W.G.M., Gao, H., Jägermeyr, J., Senay, G.B., van Dijk, A.I.J.M., Guerschman, J.P., Keys, P.W., Gordon, L.J., Savenije, H.H.G., 2016. Global root zone storage capacity from satellite-based evaporation. Hydrol. Earth Syst. Sci. 20, 1459–1481. https://doi.org/10.5194/hess-20-1459-2016

Williams, A.P., Abatzoglou, J.T., Gershunov, A., Guzman-Morales, J., Bishop, D.A., Balch, J.K., Lettenmaier, D.P., 2019. Observed Impacts of Anthropogenic Climate Change on Wildfire in California. Earths Future 7, 892–910. https://doi.org/10.1029/2019EF001210

Williams, A.P., Cook, E.R., Smerdon, J.E., Cook, B.I., Abatzoglou, J.T., Bolles, K., Baek, S.H., Badger, A.M., Livneh, B., 2020. Large contribution from anthropogenic warming to an emerging North American megadrought. Science 368, 314–318. https://doi.org/10.1126/science.aaz9600

Williams, A.P., Livneh, B., McKinnon, K.A., Hansen, W.D., Mankin, J.S., Cook, B.I., Smerdon, J.E., Varuolo-Clarke, A.M., Bjarke, N.R., Juang, C.S., Lettenmaier, D.P., 2022. Growing impact of wildfire on western US water supply. Proc. Natl. Acad. Sci. 119. https://doi.org/10.1073/pnas.2114069119

Wilschut, R.A., De Long, J.R., Geisen, S., Hannula, S.E., Quist, C.W., Snoek, B., Steinauer, K., Wubs, E.R.J., Yang, Q., Thakur, M.P., 2022. Combined effects of warming and drought on plant biomass depend on plant woodiness and community type: a meta-analysis. Proc. R. Soc. B Biol. Sci. 289, 20221178. https://doi.org/10.1098/rspb.2022.1178

Wilson, E.H., Sader, S.A., 2002. Detection of forest harvest type using multiple dates of Landsat TM imagery. Remote Sens. Environ. 80, 385–396. https://doi.org/10.1016/S0034-4257(01)00318-2

Wolf, S., Eugster, W., Ammann, C., Häni, M., Zielis, S., Hiller, R., Stieger, J., Imer, D., Merbold, L., Buchmann, N., 2013. Contrasting response of grassland versus forest carbon and water fluxes to spring drought in Switzerland. Environ. Res. Lett. 8, 035007. https://doi.org/10.1088/1748-9326/8/3/035007

Xiao, X., Hollinger, D., Aber, J., Goltz, M., Davidson, E.A., Zhang, Q., Moore, B., 2004. Satellite-based modeling of gross primary production in an evergreen needleleaf forest. Remote Sens. Environ. 89, 519–534. https://doi.org/10.1016/j.rse.2003.11.008

Xiao, X., Zhang, Q., Saleska, S., Hutyra, L., De Camargo, P., Wofsy, S., Frolking, S., Boles, S., Keller, M., Moore, B., 2005. Satellite-based modeling of gross primary production in a seasonally moist tropical evergreen forest. Remote Sens. Environ. 94, 105–122. https://doi.org/10.1016/j.rse.2004.08.015

Xu, H., Wang, X., Zhao, C., Yang, X., 2018. Diverse responses of vegetation growth to meteorological drought across climate zones and land biomes in northern China from 1981 to 2014. Agric. For. Meteorol. 262, 1–13. https://doi.org/10.1016/j.agrformet.2018.06.027

Xu, T., Guo, Z., Liu, S., He, X., Meng, Y., Xu, Z., Xia, Y., Xiao, J., Zhang, Y., Ma, Y., Song, L., 2018. Evaluating Different Machine Learning Methods for Upscaling Evapotranspiration from Flux Towers to the Regional Scale. J. Geophys. Res. Atmospheres 123, 8674–8690. https://doi.org/10.1029/2018JD028447

Yang, Y., Anderson, M., Gao, F., Xue, J., Knipper, K., Hain, C., 2022. Improved Daily Evapotranspiration Estimation Using Remotely Sensed Data in a Data Fusion System. Remote Sens. 14, 1772. https://doi.org/10.3390/rs14081772

Yang, Y., Anderson, M.C., Gao, F., Wood, J.D., Gu, L., Hain, C., 2021. Studying drought-induced forest mortality using high spatiotemporal resolution evapotranspiration data from thermal satellite imaging. Remote Sens. Environ. 265, 112640. https://doi.org/10.1016/j.rse.2021.112640

Yang, Y., Donohue, R.J., McVicar, T.R., 2016. Global estimation of effective plant rooting depth: Implications for hydrological modeling. Water Resour. Res. 52, 8260–8276. https://doi.org/10.1002/2016WR019392

Yebra, M., Van Dijk, A., Leuning, R., Huete, A., Guerschman, J.P., 2013. Evaluation of optical remote sensing to estimate actual evapotranspiration and canopy conductance. Remote Sens. Environ. 129, 250–261. https://doi.org/10.1016/j.rse.2012.11.004

Yu, G.-R., Wen, X.-F., Sun, X.-M., Tanner, B.D., Lee, X., Chen, J.-Y., 2006. Overview of ChinaFLUX and evaluation of its eddy covariance measurement. Agric. For. Meteorol. 137, 125–137. https://doi.org/10.1016/j.agrformet.2006.02.011

Yu, G.-R., Zhuang, J., Nakayama, K., Jin, Y., 2007. Root water uptake and profile soil water as affected by vertical root distribution. Plant Ecol. 189, 15–30. https://doi.org/10.1007/s11258-006-9163-y

Zanaga, D., Van De Kerchove, R., De Keersmaecker, W., Souverijns, N., Brockmann, C., Quast, R., Wevers, J., Grosu, A., Paccini, A., Vergnaud, S., Cartus, O., Santoro, M., Fritz, S., Georgieva, I., Lesiv, M., Carter, S., Herold, M., Li, L., Tsendbazar, N.-E., Ramoino, F., Arino, O., 2021. ESA WorldCover 10 m 2020 v100. https://doi.org/10.5281/zenodo.5571936

Zhang, K., Kimball, J.S., Nemani, R.R., Running, S.W., 2010. A continuous satellite-derived global record of land surface evapotranspiration from 1983 to 2006. Water Resour. Res. 46. https://doi.org/10.1029/2009WR008800

Zhang, L., Marshall, M., Vrieling, A., Nelson, A., 2023. The divergence of energy- and water-balance evapotranspiration estimates in humid regions. J. Hydrol. 624, 129971. https://doi.org/10.1016/j.jhydrol.2023.129971

Zhang, Y., Kong, D., Gan, R., Chiew, F.H.S., McVicar, T.R., Zhang, Q., Yang, Y., 2019. Coupled estimation of 500 m and 8-day resolution global evapotranspiration and gross primary production in 2002–2017. Remote Sens. Environ. 222, 165–182. https://doi.org/10.1016/j.rse.2018.12.031

Zhao, L., Xu, F., Xia, J., Wu, H., 2021. Applicability of 12 PET estimation methods in different climate regions in China. Hydrol. Res. 52, 636–657. https://doi.org/10.2166/nh.2021.128

Zhao, M., A, G., Liu, Y., Konings, A.G., 2022. Evapotranspiration frequently increases during droughts. Nat. Clim. Change 1–7. https://doi.org/10.1038/s41558-022-01505-3

Zhu, W., Tian, S., Wei, J., Jia, S., Song, Z., 2022. Multi-scale evaluation of global evapotranspiration products derived from remote sensing images: Accuracy and uncertainty. J. Hydrol. 611, 127982. https://doi.org/10.1016/j.jhydrol.2022.127982

Table 1. Modeling experiments with different settings of water availability (AW) and parameters.

Model Expt#	AW for woody	AW for non-woody	*Kc* parameters (woody; non-woody; soil)
1. Original CWS	$AW = \frac{\sum_{t-60}^{t} P}{\sum_{t-60}^{t} PET}$	$AW = \frac{\sum_{t-30}^{t} P}{\sum_{t-30}^{t} PET}$	Default (0.7;1.2;0.2)
2. NDWI-woody	$AW = \frac{1 + NDWI_t}{1 + NDWI_{max}}$	$AW = \frac{\sum_{t-30}^{t} P}{\sum_{t-30}^{t} PET}$	Default (0.7;1.2;0.2)
3. NDWI-non-woody	$AW = \frac{\sum_{t-60}^{t} P}{\sum_{t-60}^{t} PET}$	$AW = \frac{1 + NDWI_t}{1 + NDWI_{max}}$	Default (0.7;1.2;0.2)
4. NDWI-CWS	$AW = \frac{1 + NDWI_t}{1 + NDWI_{max}}$	$AW = \frac{\sum_{t-30}^{t} P}{\sum_{t-30}^{t} PET}$	Calibrated (0.63;1.00;0.30)

Table 2. Summary of 18 eddy-covariance flux-tower sites used in this study.

ID	Name	Lat, ◦	Lon, ◦	Elevation, m	IGBP land cover[a]	In Sierra	Years	Percent woody cover[b],%	Woody site
US-CZ4	Sierra Critical Zone-Shorthair	37.068	-118.987	2710	Evergreen Needleleaf Forests	Yes	2011-2012; 2015-2018	86.02	Yes
US-xTE	NEON Lower Teakettle (TEAK)	37.006	-119.006	2147	Evergreen Needleleaf Forests	Yes	2018-2020	98.09	Yes
US-CZ3	Sierra Critical Zone-P301	37.067	-119.195	2015	Evergreen Needleleaf Forests	Yes	2008-2019	99.08	Yes
US-Blo	Blodgett Forest	38.895	-120.633	1315	Evergreen Needleleaf Forests	Yes	2003-2007	93.57	Yes
US-xSP	NEON Soaproot Saddle (SOAP)	37.033	-119.262	1160	Evergreen Needleleaf Forests	Yes	2017-2020	86.13	Yes
US-CZ2	Sierra Critical Zone-Soaproot Saddle	37.031	-119.256	1160	Evergreen Needleleaf Forests	Yes	2010-2018	81.95	Yes
US-CZ1	Sierra Critical Zone-San Joaquin Experimental Range	37.109	-119.731	400	Savannas	Yes	2011-2019	24.02	No
US-Ton	Tonzi Ranch	38.431	-120.966	177	Woody Savannas	Yes	2003-2020	47.17	Yes
US-Var	Vaira Ranch- Ione	38.413	-120.951	129	Grasslands	Yes	2003-2020	14.79	No
US-SCf	Southern California Climate Gradient - Oak/Pine Forest	33.808	-116.772	1770	Mixed Forests	No	2006-2015	99.93	Yes
US-SO3	Sky Oaks- Young Stand	33.377	-116.623	1429	Closed Shrublands	No	2003-2006	99.61	Yes
US-SO4	Sky Oaks- New Stand	33.385	-116.641	1429	Closed Shrublands	No	2005-2006	98.13	Yes
US-SO2	Sky Oaks- Old Stand	33.374	-116.623	1394	Closed Shrublands	No	2003-2006	99.68	Yes
US-SCw	Southern California Climate Gradient - Pinyon/Juniper Woodland	33.605	-116.455	1281	Open Shrublands	No	2006-2018	97.15	Yes
US-SCc	Southern California Climate Gradient -Desert Chaparral	33.609	-116.451	1280	Open Shrublands	No	2007-2018	94.82	Yes
US-SCs	Southern California Climate Gradient - Coastal Sage	33.734	-117.696	470	Open Shrublands	No	2006-2018	20.36	No
US-SCg	Southern California Climate Gradient - Grassland	33.737	-117.695	465	Grasslands	No	2006-2018	29.03	No
US-SCd	Southern California Climate Gradient - Sonoran Desert	33.652	-116.372	275	Barren Sparse Vegetation	No	2006-2014	3.88	No

a: Metadata for each site was retrieved from AmeriFlux site information edited by the tower team. International Geosphere-Biosphere Programme (IGBP).
b: Percent woody cover was estimated using the European Space Agency (ESA) WorldCover 2020 product at a 10-m resolution, with tree and shrub being classified as woody areas (Figure S4).

Table 3. Evaluation of ET estimates from different modeling experiments and products using flux-tower observations. Performance metrics in the table are in the format of RMSE (R2; MBD), where MBD denotes mean bias difference.

Flow-tower data	Original CWS	NDWI-woody	NDWI-non-woody	NDWI-CWS	MOD16	PML2	FLUXCOM	GLEAM	BESS	CECS
1-day (18 sites)	0.95 (0.36;-0.14)	0.92 (0.44;0.08)	1.23 (0.18;0.09)	0.87 (0.46;-0.01)	--	--	--	1.53 (0.01;-1.01)	--	--
8-day (18 sites)	6.57 (0.46;-1.03)	6.12 (0.56;0.97)	9.21 (0.22;1.04)	5.62 (0.59;0.18)	7.64 (0.39;0.97)	6.23 (0.50;0.12)	6.73 (0.50;-2.58)	12.21 (0.02;-8.56)	--	--
8-day (7 Sierra woody sites)	8.15 (0.55;-4.21)	6.79 (0.55;0.04)	8.31 (0.55;-4.44)	6.71 (0.57;-0.89)	10.68 (0.26;-6.21)	7.22 (0.50;- 0.61)	6.22 (0.67;-0.98)	16.58 (0.01;-12.91)	--	--
8-day (2 Sierra non-woody sites)	5.85 (0.67;2.33)	5.85 (0.67;2.33)	10.40 (0.53;7.76)	5.32 (0.68;0.79)	5.17 (0.73;-1.38)	6.47 (0.52;1.10)	5.50 (0.67;1.32)	11.77 (0.10;-7.81)	--	--
Monthly (18 sites)	20.45 (0.58;-3.37)	18.71 (0.68;2.75)	29.73 (0.34;2.81)	16.99 (0.71;0.09)	24.42 (0.48;-8.90)	24.41 (0.48;6.24)	21.92 (0.57;-8.51)	40.07 (0.06;-26.14)	24.49 (0.47;-11.15)	26.18 (0.50;-14.13)
Monthly (7 Sierra woody sites)	25.22 (0.73;-12.26)	20.36 (0.73;-0.40)	25.77 (0.73;-12.91)	20.08 (0.74;-2.80)	34.06 (0.43;-15.14)	29.19 (0.48;7.47)	19.37 (0.78;-3.16)	53.78 (0.02;-37.25)	29.69 (0.57;-16.40)	22.92 (0.65;-8.85)
Monthly (2 Sierra non-woody sites)	17.66 (0.73;7.41)	17.66 (0.73;7.41)	34.95 (0.56;24.90)	15.68 (0.75;2.47)	14.93 (0.81;-4.15)	22.59 (0.50;6.40)	16.99 (0.69;4.32)	37.95 (0.17;-29.33)	17.81 (0.68;1.14)	23.31 (0.48;-2.81)

Table 4. Water-balance-based evaluation of ET from four modeling experiments and six products at 58 catchments in the Sierra Nevada.

Model experiment/ Product	RMSE[a], mm	R^2	MBD[b], mm
Original CWS	106.21	0.35	-39.08
NDWI-woody	131.05	0.40	49.14
NDWI-non-woody	140.08	0.12	61.26
NDWI-CWS	113.01	0.42	26.85
MOD16	236.4	0.38	-216.99
PML2	106.19	0.37	40.47
GLEAM	132.21	0.14	10.11
BESS	127.48	0.17	-66.47
FLUXCOM	102.86	0.37	30.40
CECS	141.25	0.37	-70.97

a: RMSE denotes root-mean-square error.
b: MBD denotes mean bias difference.

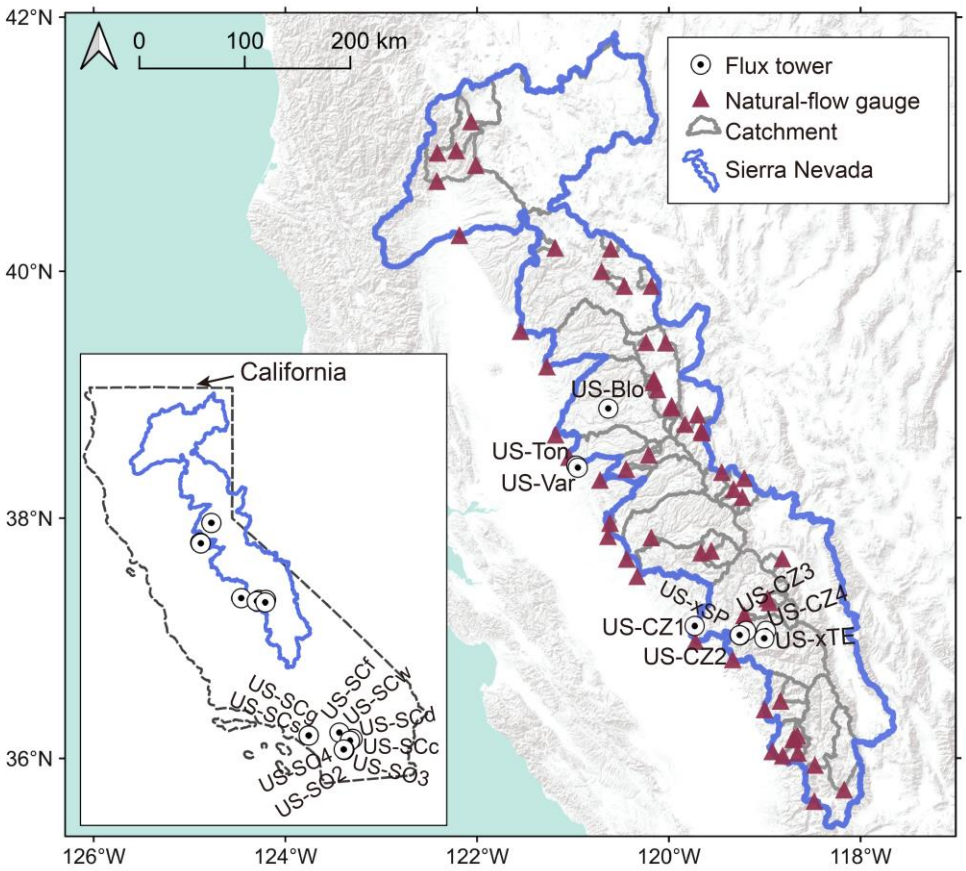

Figure 1. Map of the Sierra Nevada in Mediterranean California, showing the location of 18 flux-tower sites (Table 2) and 58 catchments (Table S1) with long-term natural streamflow data. The background terrain map is from the ESRI service.

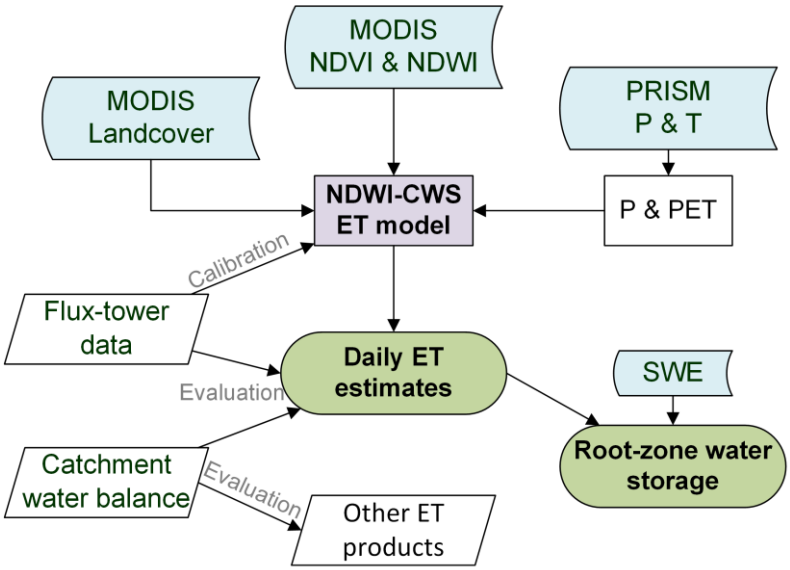

Figure 2. Flowchart of MODIS-based NDWI-CWS ET model, its evaluation processes, and subsequent estimates of root-zone water storage.

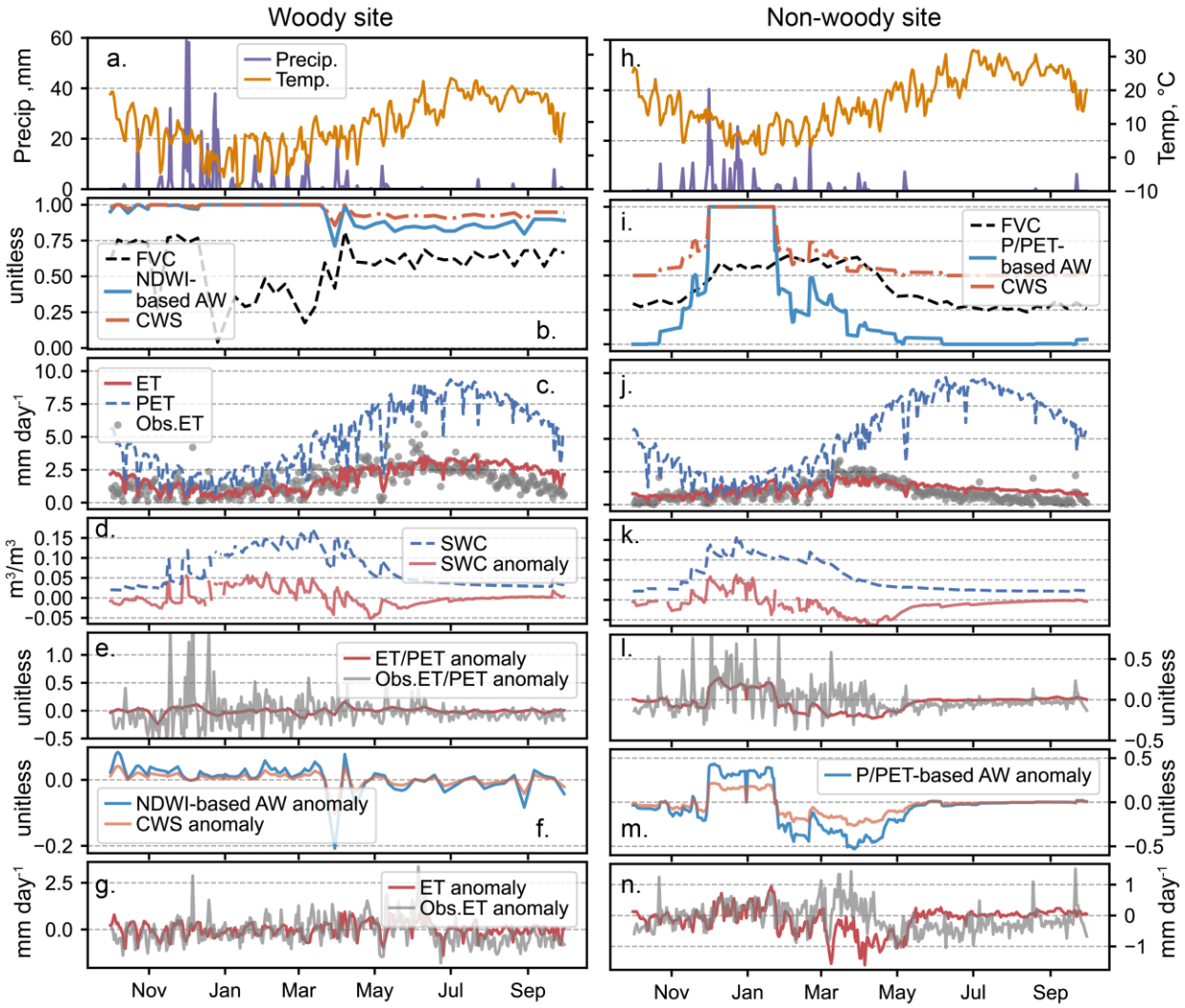

Figure 3. Examples of variables for estimating daily NDWI-CWS ET in WY2013. For a woody site (US-CZ3), left panels show (a) precipitation and temperature, (b) fractional vegetation cover (FVC), canopy-water-stress factor (CWS), NDWI-based water availability (AW), (c) observed ET, modeled ET, and potential ET (PET), (d) soil moisture (SWC) and its anomaly (removing seasonality from data), (e) the anomalies of ET/PET and observed ET/PET, (f) the anomalies of NDWI-based AW and CWS, and (g) the anomalies of observed ET and modeled ET. Similar to the woody site, right panels (h-n) show the variables for the non-woody site (US-CZ1). However, AW in panel (i) was calculated using P/PET instead of the NDWI-based method.

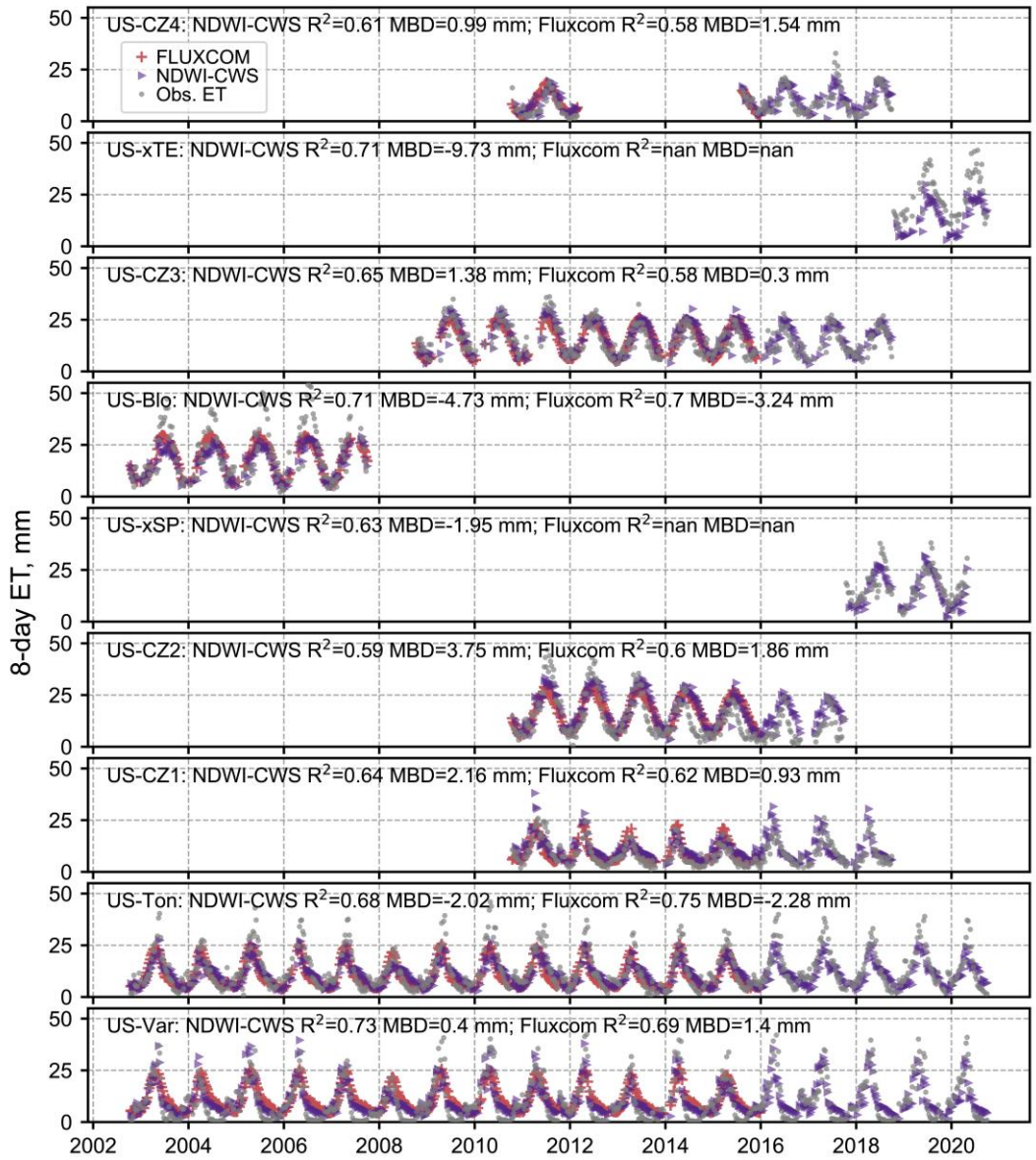

Figure 4. Comparison of 8-day ET from flux-tower observation (gray marker), NDWI-CWS model (purple marker), and FLUXCOM model (red marker, data end in 2015) at the nine sites inside the Sierra Nevada. Panels of the flux-tower sites from top to bottom are sorted by their elevation from highest to lowest. The nan stands for not a number, which appears when FLUXCOM data are not available.

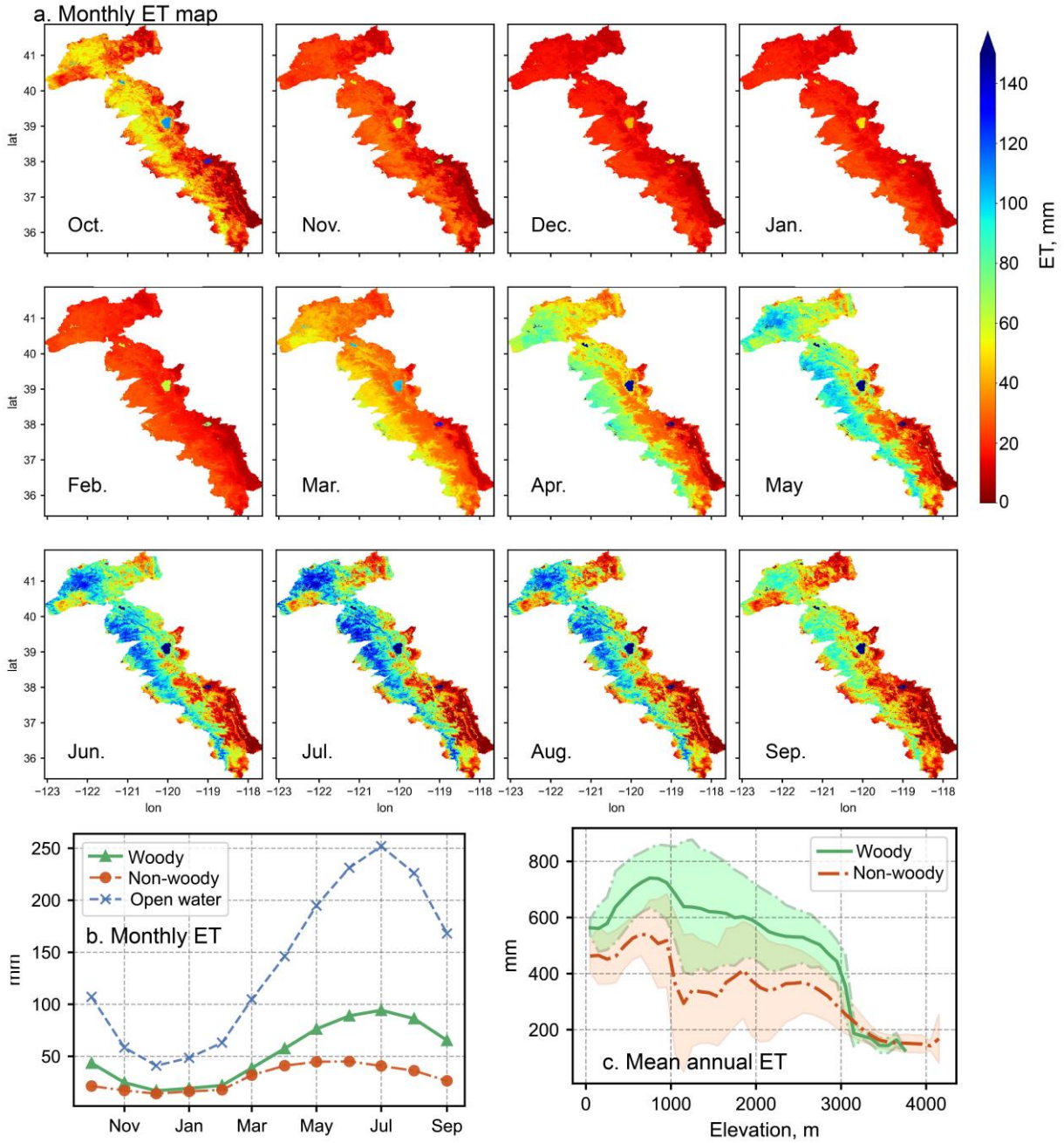

Figure 5. (a) Monthly ET map calculated as the mean value of each month during WY2003-2020. (b) Time series of mean monthly ET for the woody, non-woody, and open-water areas in the Sierra Nevada. (c) Mean annual ET versus elevation. Shaded area indicates one standard deviation from the mean value.

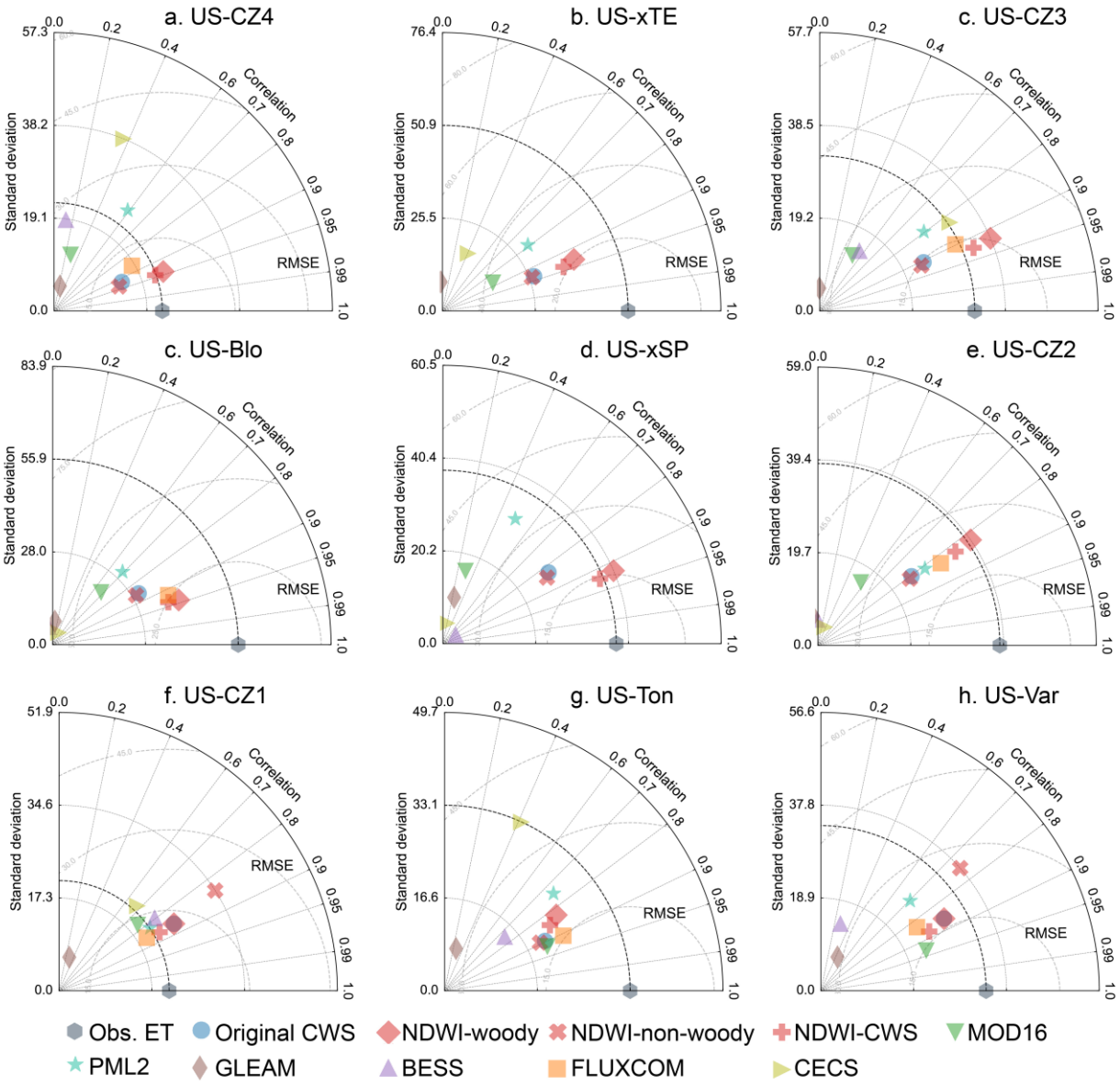

Figure 6. Taylor diagrams showing model performances (standard deviation, RMSE, and correlation coefficient) using monthly ET observation at nine sites inside the Sierra Nevada. Panels are sorted by site elevation. Note that results from FLUXCOM were not plotted at US-xTE and US-xSP, since FLUXCOM data ended in 2015 not covering the measured data at the two sites.

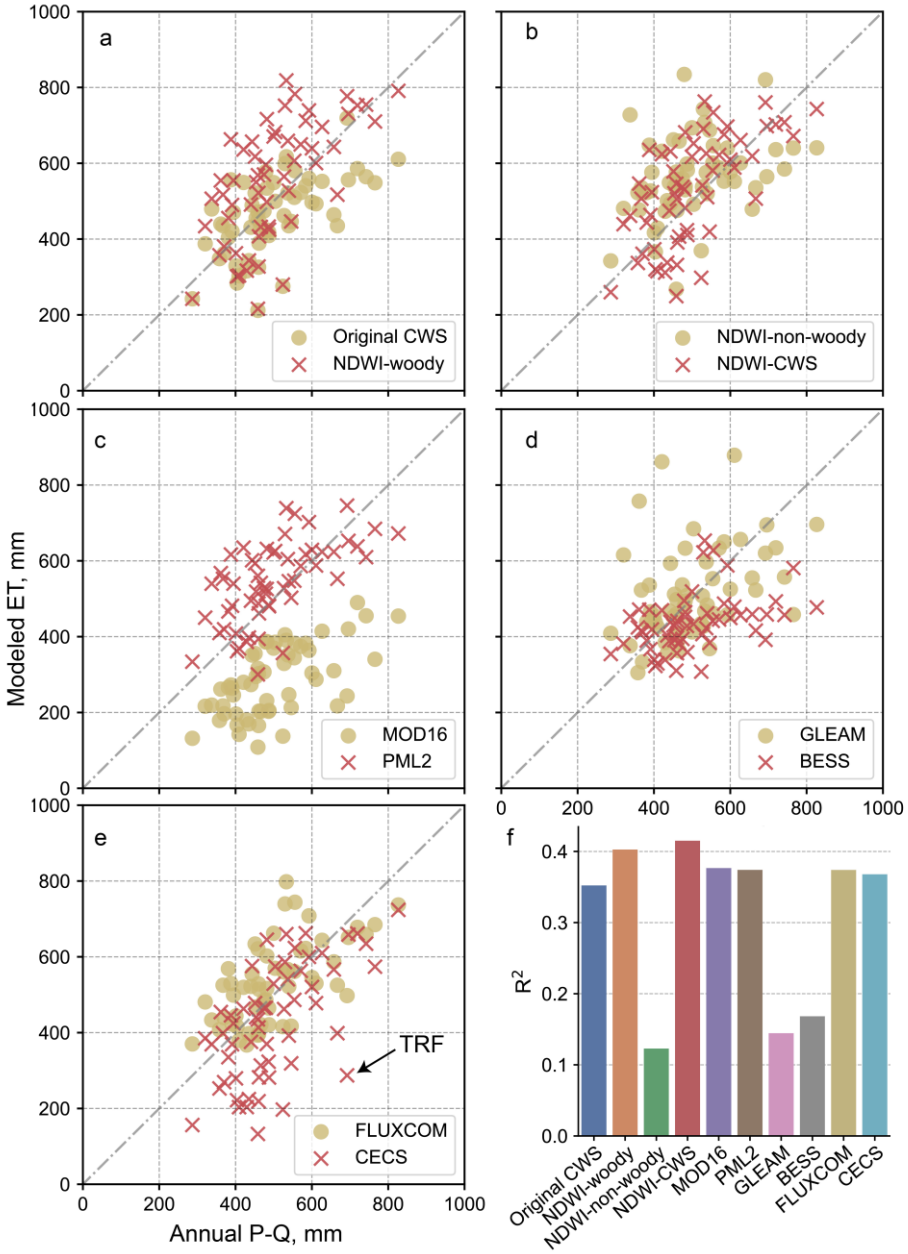

Figure 7. Scatterplot of annual ET from different models (panels a-e) versus that from P – Q at 58 catchments with long-term (≥ 10 years) measurements. Panel f shows the R2 value of each model.

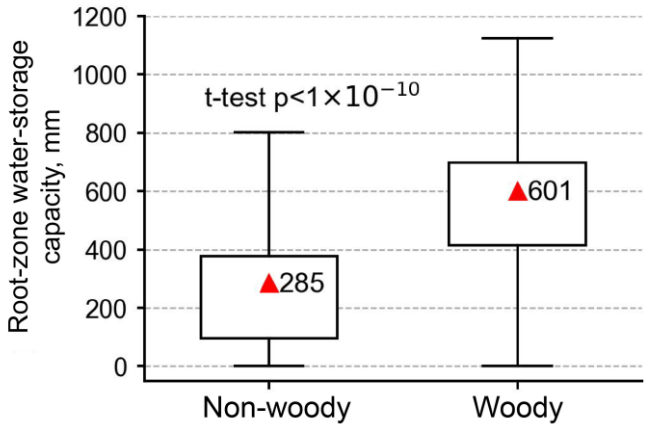

Figure 8. Comparison of root-zone water storage capacity between woody and non-woody areas. Red triangle in the boxplot denotes the labeled mean value. The p-value from the Student's T-test is labeled.

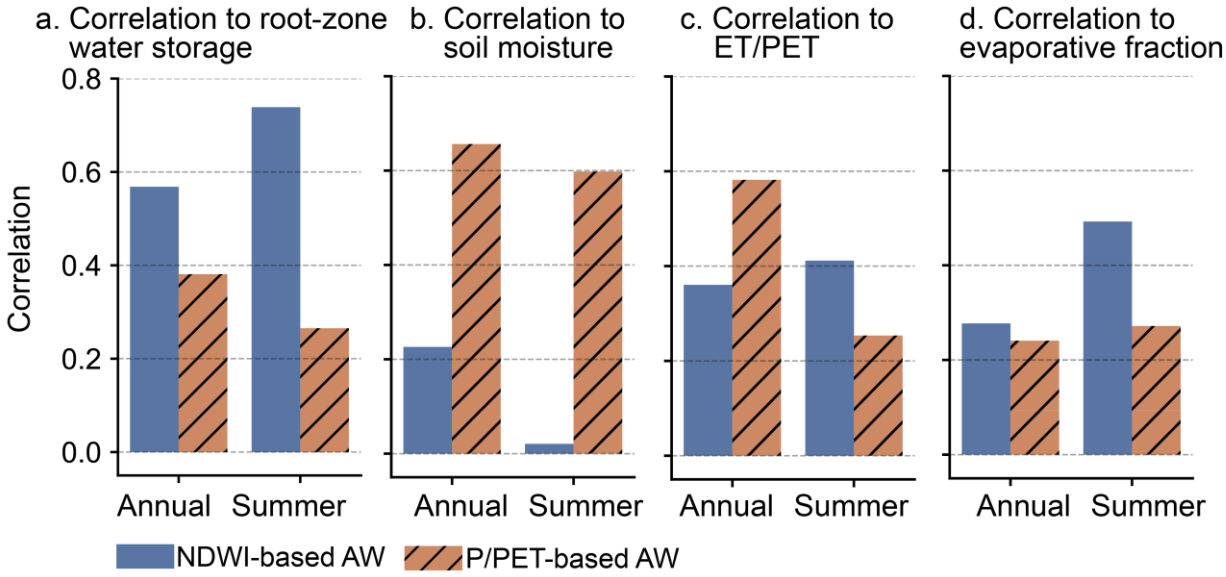

Figure 9. Correlation between deseasonalized values of AW and a) root-zone water storage, b) soil moisture measurements at flux-tower sites, c) evaporation efficiency (ET/PET), and d) evaporative fraction, which is the ratio of latent heat flux to the sum of latent and sensible heat fluxes from FLUXCOM product. "Annual" denotes correlation using annual data throughout our study period (Figures S13, S14, and S15), and "summer" denotes the correlation calculated only using summer data.

Supplemental Material

Text S1

We collected rain-gauge measurements from 180 sites spreading in the Sierra Nevada (Figure S3a) from the California Data Exchange Center (CDEC, https://cdec.water.ca.gov/). The sites, with elevations ranging from 142 to 3263 (Figure S3b), provide daily precipitation data with records spanning at least 10 years during water years 2004-2020. We used the gauge data to evaluate the PRISM gridded data at different elevation bands. In the comparison of long-term annual precipitation elevation versus elevation, PRISM generally aligns well with gauge measurements (R2=0.87 and a positive bias of 2.93%, Figure S3c). Both gauge and PRISM data indicated that precipitation generally increases with elevation below 1000 m and tends to decrease above 2750 m. Compared to annual data of eight gauges at a low-elevation band of 400-600 m, PRISM yielded a high R2 value of 0.97 with a positive bias of 1.62% (Figure S3d). Compared to annual data of 12 gauges at 1600-1800 m elevation, PRISM had an R2 value of 0.95 with a positive bias of 2.15% (Figure S3e). At the high-elevation band of 2800-3000 m, PRISM showed a lower R2 value of 0.82 with a negative bias of -5.37% (Figure S3f), indicating greater uncertainty at higher elevations than at lower elevations.

Text S2

In addition to the four modeling experiments in Table 1, it is worth exploring whether a longer duration in Equation 3 for woody vegetation can improve ET estimates in Mediterranean mountains. Thus, we tested the ET estimates from the original CWS with different durations ranging from 60 to 360 days (Table S3). We found that the original CWS model with a duration of 180 days (denoted as CWS-P/PET180) shows a good performance based on point-scale evaluation, e.g. an R2 value of 0.79 against monthly flux-tower data at seven woody sites inside the Sierra Nevada. Water-balance-based evaluation using 58 catchments (Table S4 and Figure S18) suggests that the CWS-P/PET180 model has a smaller value of R2 (0.40) than our NDWI-CWS model (0.42). The water availability using P/PET with a duration of 180 days has larger correlations (Figure S19; 0.694 on an annual scale and 0.693 for summer only) with root-zone water storage, than does the original CWS model with default 60 days (Equation 3). In comparison, the NDWI-based water availability has a larger correlation of 0.74 to root-zone water storage during the high-ET summer season (Figure 10a). Therefore, selecting an appropriate duration value can improve the performance of the original CWS model. Considering the important role of root-zone water storage in supporting deep-rooted vegetation during the summer growing season, we recommend using water availability based on remote-sensed NDWI data to better reflect the dynamics of root-zone water storage.

Table S1. Streamflow gages and characteristics of 58 catchments used for water-balance-based ET estimates. Twenty-six natural-flow gages from the California Data Exchange Center are labeled using letter ID, and the remaining 32 USGS gages without upstream dams are labeled using numerical ID.

Gage ID	Lat, ◦	Lon, ◦	River Basin	Area, km²	Annual P, mm	Annual Q, mm	Woody%	Non-woody%	Open water%
YRS	39.235	-121.274	YUBA R	2872	1639	943	55.1	44.6	0.3
11204100	36.024	-118.813	TULE R	249	1552	942	41.7	58.1	0.1
SDT	40.940	-122.416	SACRAMENTO R	1093	1531	947	65.9	33.9	0.1
MSS	40.958	-122.219	MC CLOUD R	1567	1429	947	55.9	43.8	0.3
11203580	36.048	-118.654	TULE R	52	1428	1007	71.4	28.2	0.3
10336660	39.107	-120.162	LAKE TAHOE	31	1353	1033	16.3	77.7	5.9
10336775	38.903	-119.969	LAKE TAHOE	60	1304	860	32.4	67.6	0.0
AMF	38.683	-121.183	AMERICAN R	4819	1295	669	43.5	55.9	0.6
MKM	38.313	-120.719	MOKELUMNE R	1407	1223	652	37.1	62.9	0.1

10336676	39.132	-120.157	LAKE TAHOE	25	1217	391	34.4	63.7	1.9
10336780	38.920	-119.973	LAKE TAHOE	95	1117	613	24.0	76.0	0.0
SNS	37.852	-120.637	STANISLAUS R	2537	1116	562	24.0	74.6	1.3
10308783	38.701	-119.657	CARSON R	11	1114	713	0.0	100.0	0.0
11202710	36.161	-118.708	TULE R	223	1113	752	71.7	28.3	0.0
10291500	38.239	-119.326	WALKER R	114	1105	702	0.3	99.7	0.0
FTO	39.522	-121.547	FEATHER R	9433	1082	545	39.2	59.0	1.8
11400500	40.187	-121.188	FEATHER R	168	1064	606	69.1	29.3	0.0
CSN	38.500	-121.044	COSUMNES R	1386	1051	332	51.0	48.9	0.1
TLG	37.666	-120.441	TUOLUMNE R	3983	1041	581	20.9	78.3	0.9
11401165	40.001	-120.703	FEATHER R	18	1026	659	64.5	35.5	0.0
10289500	38.174	-119.234	WALKER R	51	1026	359	0.0	100.0	0.0
WFC	38.769	-119.832	CARSON R	170	991	504	0.1	99.9	0.0
MRC	37.522	-120.331	MERCED R	2707	965	438	28.5	71.3	0.2
11367500	41.188	-122.065	Upper Sac. R	943	958	434	39.3	59.9	0.5
WWR	38.378	-119.449	WALKER R	465	936	527	0.3	99.7	0.0
11230500	37.339	-118.973	SAN JOAQUIN R	136	933	333	0.3	99.7	0.0
11264500	37.732	-119.559	MERCED R	470	932	167	1.0	98.9	0.1
11316800	38.403	-120.447	MOKELUMNE R	55	925	466	64.0	36.0	0.0
SJF	36.984	-119.724	SAN JOAQUIN R	4341	920	480	14.7	85.0	0.3
103087891	38.717	-119.660	CARSON R	2	919	177	0.0	100.0	0.0
SBB	40.289	-122.186	SACTO VLY NE	22977	900	425	28.5	71.0	0.5
TRF	39.428	-120.033	LAKE TAHOE	2415	895	203	12.1	66.6	21.3
11266500	37.716	-119.666	MERCED R	835	890	298	4.2	95.7	0.0
10343500	39.431	-120.238	Truckee R	27	885	227	38.2	61.8	0.0
KGF	36.831	-119.335	KINGS R	3997	881	500	12.3	87.6	0.1
SIS	40.718	-122.420	PIT R	16557	848	394	28.7	70.8	0.5
11284400	37.842	-120.185	TUOLUMNE R	42	848	292	67.2	32.8	0.0
11189500	35.737	-118.174	KERN R	1371	841	381	8.8	91.2	0.0
EFC	38.847	-119.703	CARSON R	921	836	349	3.3	96.7	0.0
11208600	36.484	-118.836	Kaweah R	428	834	295	34.0	65.8	0.2
11299600	37.961	-120.615	STANISLAUS R	37	827	294	0.0	100.0	0.0
11230200	37.306	-118.951	SAN JOAQUIN R	16	814	332	0.0	100.0	0.0

KWT	36.412	-119.003	KAWEAH R	1450	798	347	29.5	70.4	0.1
11186000	35.945	-118.478	KERN R	2191	746	460	7.1	92.9	0.0
DAV	39.883	-120.467	FEATHER R	113	710	322	30.4	62.1	7.5
10265150	37.669	-118.818	Owens R	186	691	257	0.4	99.3	0.3
11237500	37.198	-119.214	SAN JOAQUIN R	60	674	213	1.1	98.9	0.0
10336645	39.052	-120.119	LAKE TAHOE	20	667	188	19.3	79.3	1.4
11315000	38.519	-120.213	MOKELUMNE R	55	665	135	1.8	98.2	0.0
PSH	40.843	-122.016	PIT R	12739	650	259	19.2	80.6	0.2
SCC	36.061	-118.922	TULE R	1009	643	143	36.6	63.4	0.0
ANT	40.180	-120.607	FEATHER R	184	612	218	10.9	87.5	1.6
11201456	36.192	-118.658	TULE R	80	601	55	61.0	39.0	0.0
11202000	36.175	-118.696	TULE R	102	584	118	65.6	34.4	0.0
EWR	38.328	-119.214	WALKER R	905	568	139	0.1	99.6	0.2
KRI	35.639	-118.484	KERN R	5367	520	150	17.6	82.2	0.2
FRD	39.883	-120.183	FEATHER R	211	464	127	4.8	95.1	0.2
11237700	37.199	-119.215	SAN JOAQUIN R	60	436	78	1.1	98.9	0.0

Table S2. Landcover classification based on the International Geosphere-Biosphere Programme (IGBP) from MODIS.

Landcover	MODIS IGBP class
Woody	Evergreen Needleleaf Forests; Evergreen Broadleaf Forests; Deciduous Needleleaf Forests; Deciduous Broadleaf Forests; Mixed Forests; Closed Shrublands; Open Shrublands;Woody Savannas;
Non-woody[a]	Grasslands; Croplands; Savannas; Barren; Urban and Built-up Lands; Cropland/Natural Vegetation Mosaics
Open water	Permanent Wetlands; Permanent Snow and Ice; Water Bodies

a For simplicity, the nonforest area (54% area of our study domain using 2011 MODIS data) in this study includes croplands (0.4% area of our study domain), Urban and Built-up Lands (0.8%), and Barren (5%).

Table S3. Sensitivity analysis of results from the original CWS model with different time durations in Equation 3. Evaluations are based on flux-tower observations. Performance metrics in the table are in the format of RMSE (R2; MBD), where MBD denotes mean bias difference.

Flow-tower data	Default 60 days (Eq. 3)	120 days	180 days	240 days	300 days	360 days
Daily (18 sites)	0.95 (0.36;-0.14)	0.89 (0.43;-0.06)	0.87 (0.47;-0.01)	0.88 (0.46;0.002)	0.90 (0.42;-0.01)	0.91 (0.39;-0.04)
8-day (18 sites)	6.57 (0.46;-1.03)	5.94 (0.55;-0.39)	6.02 (0.56;0.20)	6.02 (0.56;0.34)	6.13 (0.53;0.10)	6.24 (0.50;-0.16)
8-day (7 Sierra woody sites)	8.15 (0.55;-4.21)	6.76 (0.64;-2.84)	6.19 (0.66;-1.65)	6.68 (0.60;-1.16)	7.33 (0.51;-1.45)	7.53 (0.48;-2.14)

Monthly (18 sites)	20.45 (0.58;-3.37)	18.17 (0.66;-1.67)	17.47 (0.70;-0.45)	18.84 (0.66;-0.52)	21.58 (0.56;-1.65)	22.92 (0.50;-3.0)
Monthly (7 Sierra woody sites)	25.22 (0.73;-12.26)	20.49 (0.78;-8.73)	18.84 (0.79;-5.8)	22.10 (0.71;-5.53)	27.66 (0.56;-7.74)	30.04 (0.49;-10.66)

Note: For example, in the original CWS model with a duration of 180 days, Equation 3 is changed to $AW = \frac{\sum_{t-180}^{t} P}{\sum_{t-180}^{t} PET}$,for woody vegetation.

Table S4. Water-balance-based evaluation of ET at 58 catchments in the Sierra Nevada.

Model experiment/ Product	RMSE, mm	R^2	MBD, mm
Original CWS	106.21	0.35	-39.08
CWS w P/PET 180 days	111.85	0.40	23.6
NDWI-CWS	113.01	0.42	26.85

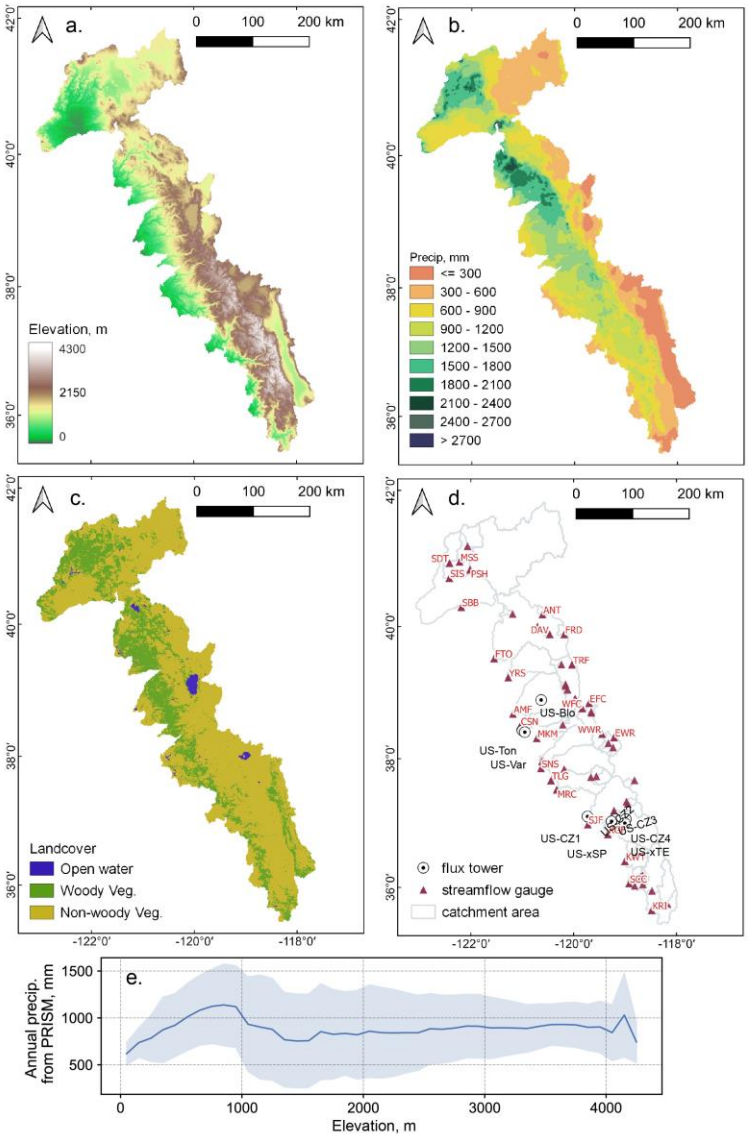

Figure S1. Maps of (a) elevation, (b) average water year precipitation using PRISM data for 2003-2020, (c) land cover, (d) flux towers and gages with available long-term natural-flow data in the Sierra Nevada, and (e) mean annual (water-year) precipitation from PRISM vs. elevation, with shaded area indicating one standard deviation from the mean.

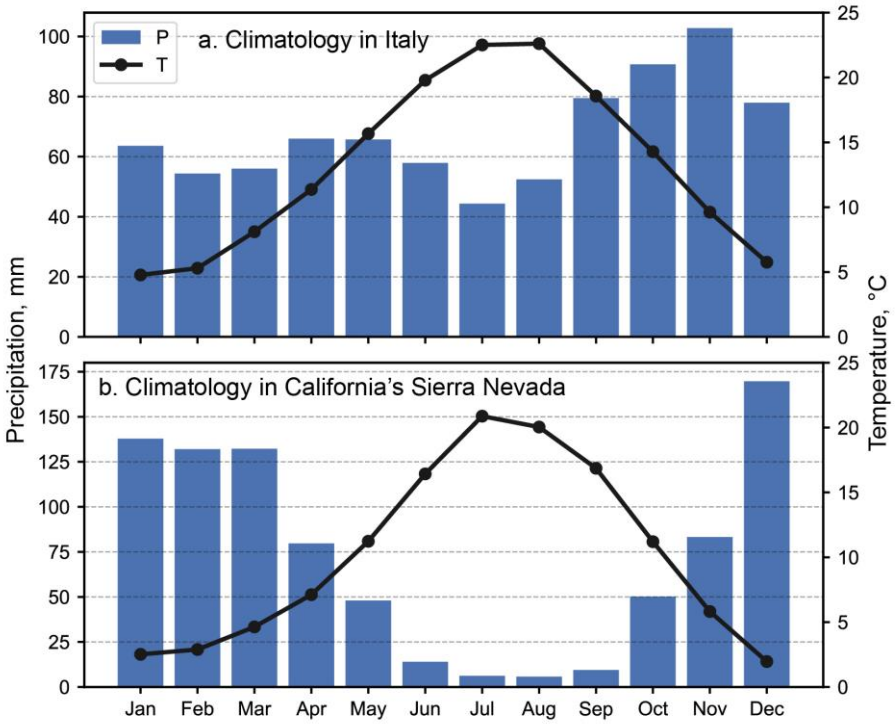

Figure S2. Monthly climatology of precipitation and temperature in (a) Italy where the original CWS model was applied; data are from (Worldbank, 2022). (b) Climatology in California's Sierra Nevada using PRISM data.

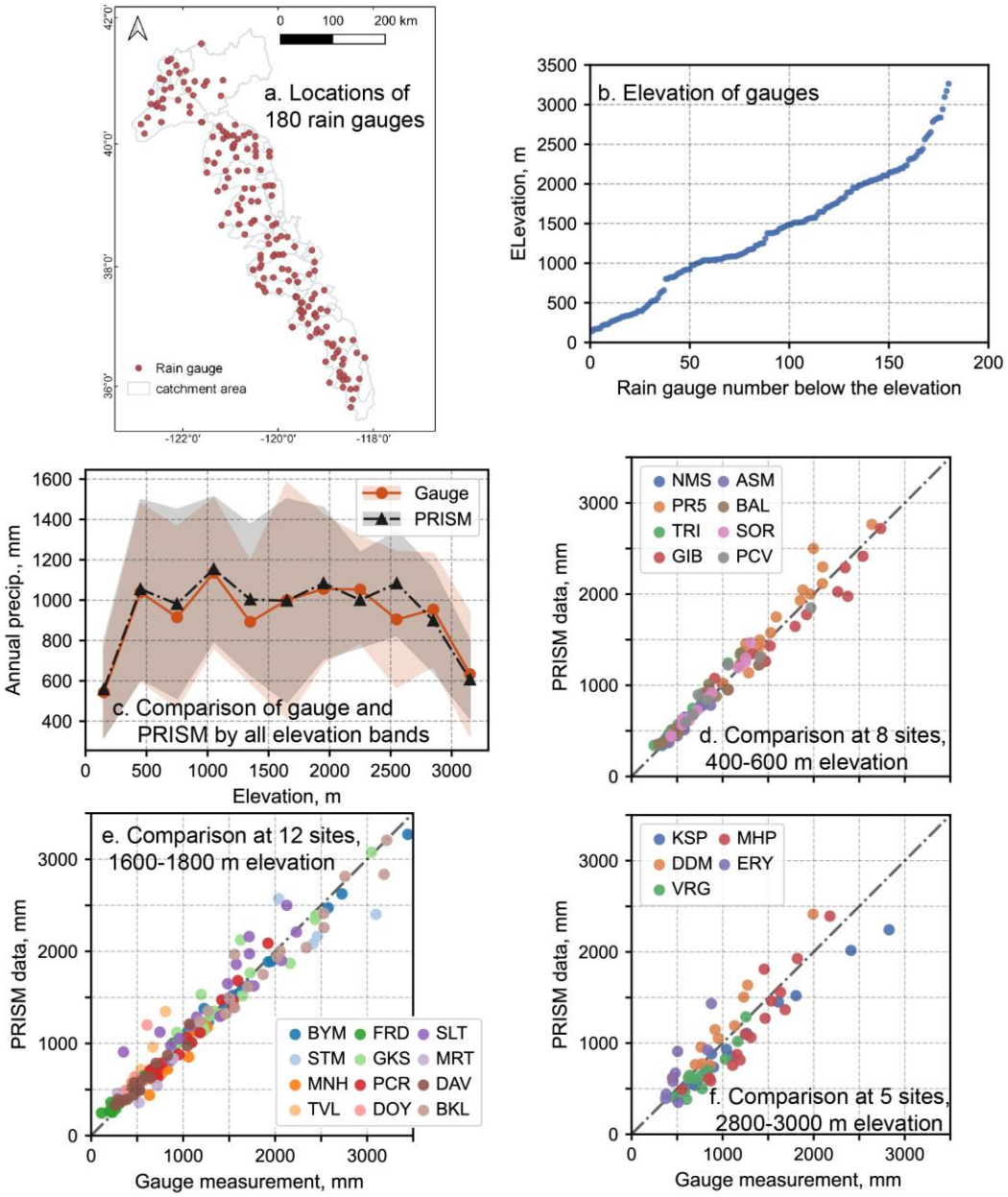

Figure S3. Comparison of rain-gauge measurements versus PRISM precipitation data: (a) map of 180 rain-gauge sites; (b) plot of site elevation; (c) long-term mean annual precipitation versus elevation at the 180 sites, banded by 300-meter elevation intervals; and panels d-f show the scatter plots of annual precipitation from gauge versus PRISM data at the elevation bands of 400-600 m, 1600-1800 m, and 2800-3000 m, respectively. Points with the same color represent annual precipitation for different water years at the same site.

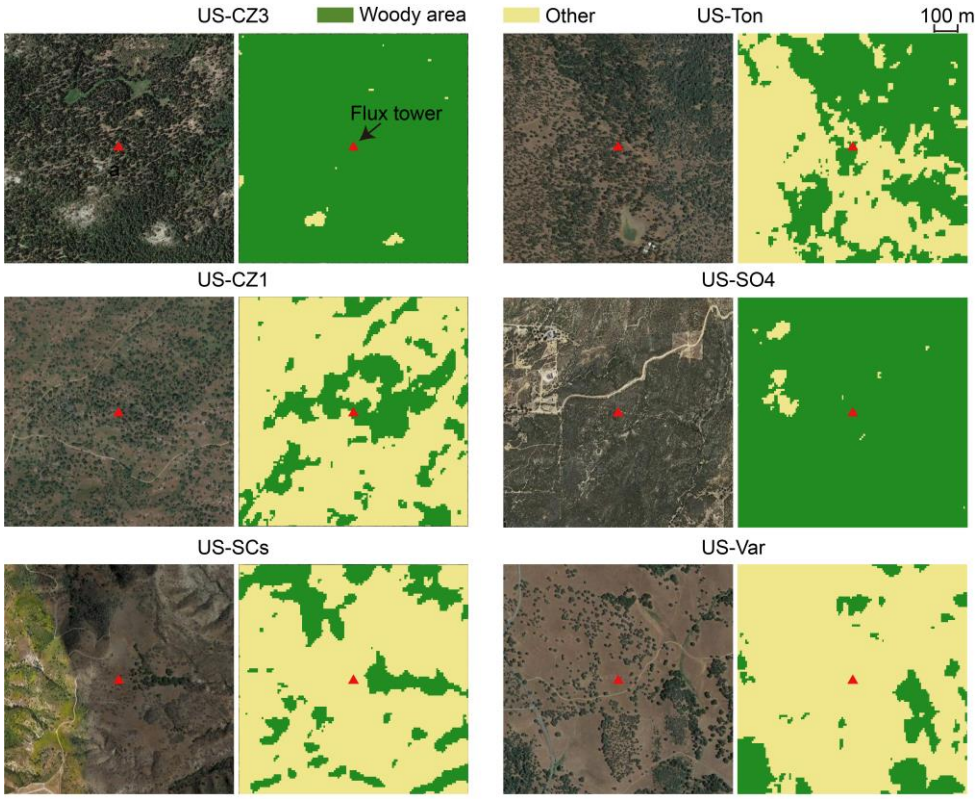

Figure S4. Satellite images and woody-area maps of six sites, showing a 1-km2 rectangular area around six flux towers (red triangles located at the center of the images). Images were retrieved from Google Satellite Map. The European Space Agency (ESA) WorldCover 2020 product at a 10-m resolution was used to classify woody areas (tree and shrub, colored green) and other areas (yellow), which were then used to estimate the percent woody cover for each site. Together with the land-cover metadata (Table 2), this study classified US-Ton (woody savannas) with percent woody cover of 47.17% (consistent with site information detailed in (Baldocchi et al., 2004; Kim et al., 2006; Ma et al., 2016)) as a woody site, and classified US-SCs (open shrublands) with percent woody cover of 20.36% as a non-woody site.

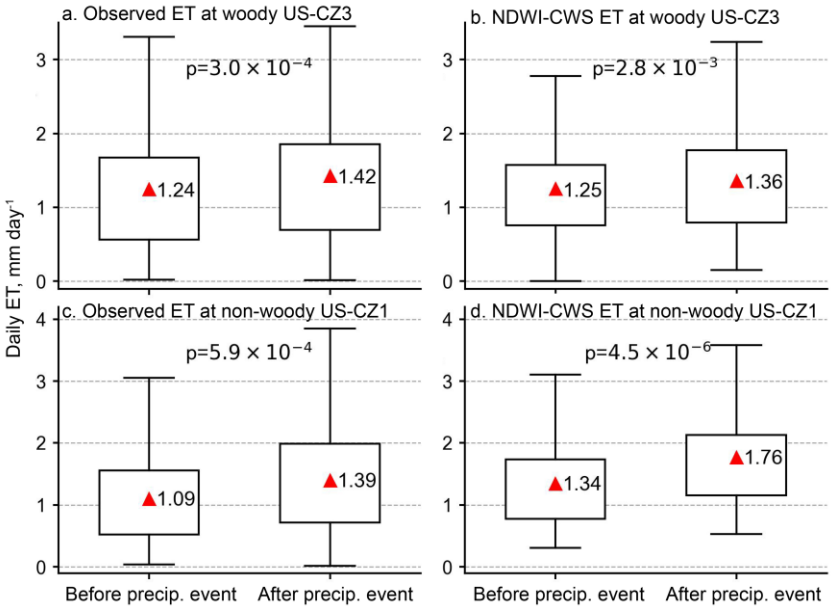

Figure S5. Comparison of daily ET during one week before and one week after heavy precipitation events. Top panels a and b show the comparison of observed ET data and NDWI-CWS ET estimates at the woody site US-CZ3, respectively. Similarly, bottom panels c and d show the comparison at the non-woody site US-CZ1. Heavy precipitation events during the study period were identified as consecutive days with precipitation larger than 0.254 mm and cumulative precipitation greater than 2 cm (Cui et al., 2023, 2022). Red triangle in the boxplot denotes the labeled mean value. The p-value from the Student's T-test is labeled.

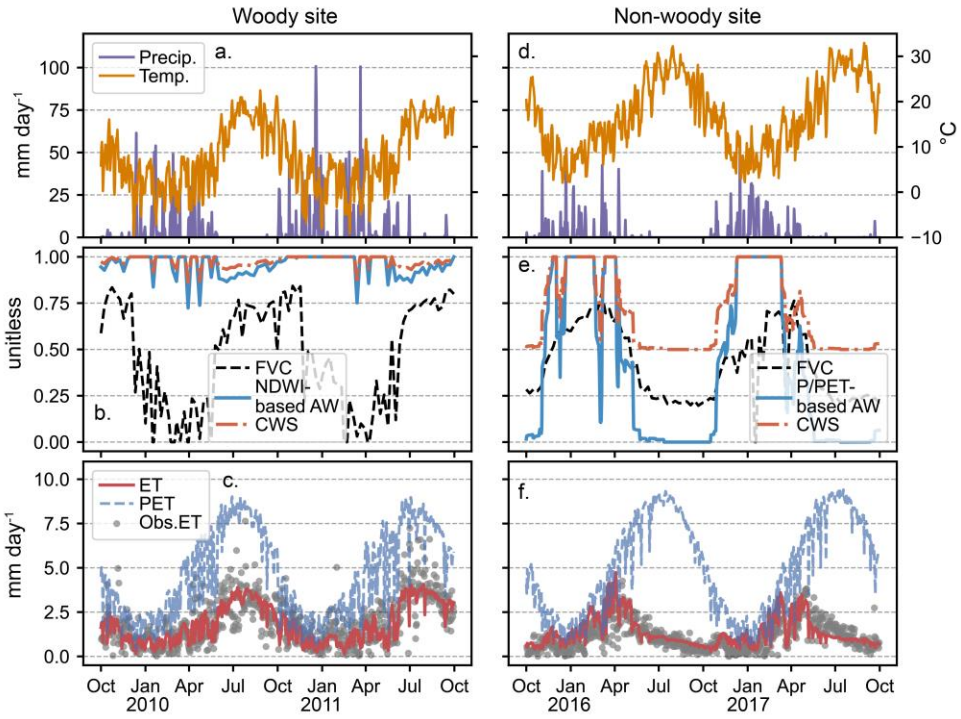

Figure S6. Variables for estimating daily NDWI-CWS ET. Left panels (a-c) show the variables and ET measurements for a woody site (US-CZ3) during WY2010-2011, and right panels (d-f) for a non-woody site (US-CZ1) during WY2016-2017.

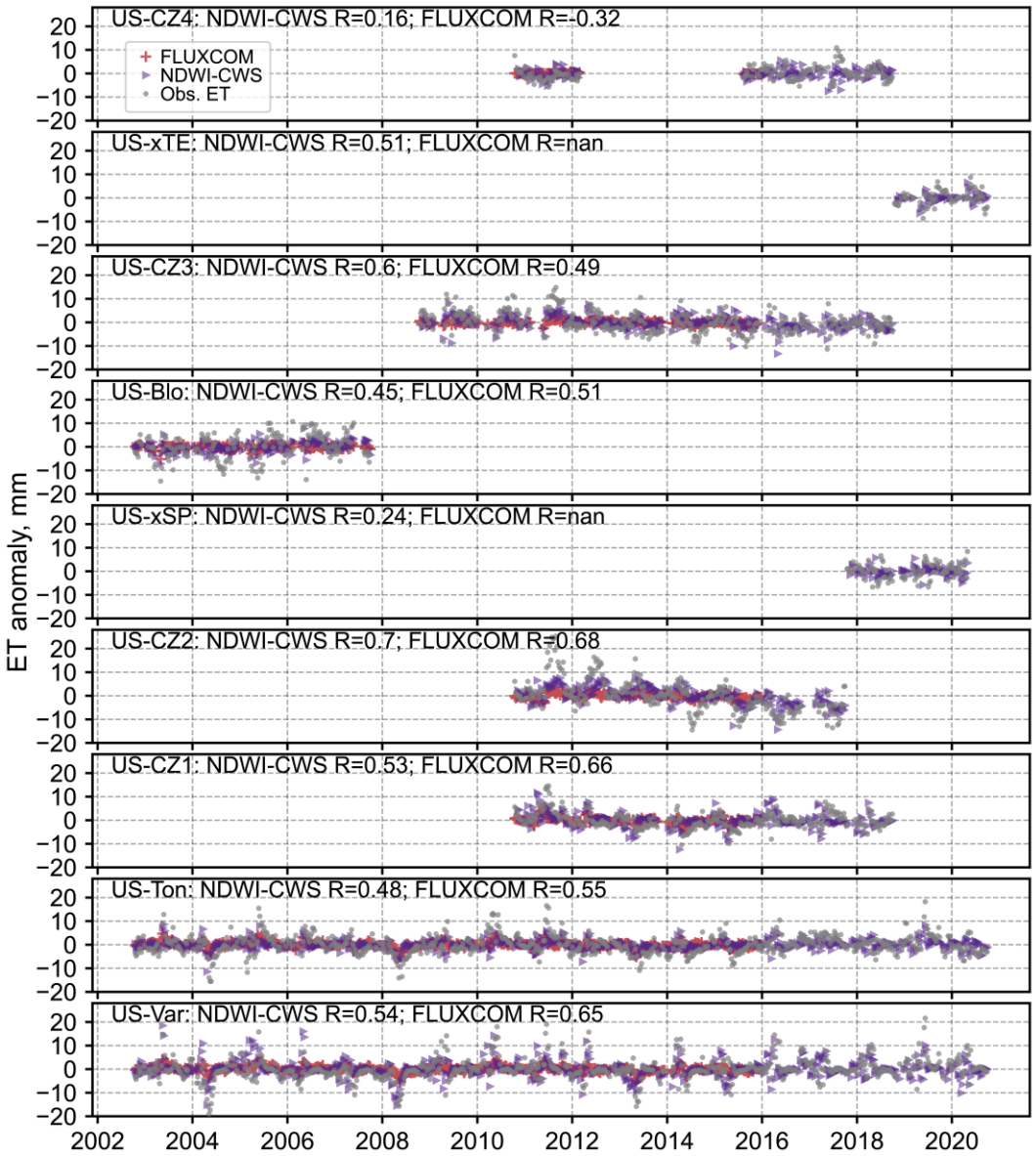

Figure S7. Comparison of 8-day ET anomaly (i.e., removing the seasonality signal from the data): flux-tower observation (gray marker), NDWI-CWS model (purple marker), and FLUXCOM model (red marker) at the nine sites inside the Sierra Nevada. Panels of the flux-tower sites from top to bottom are sorted by their elevation from highest to lowest.

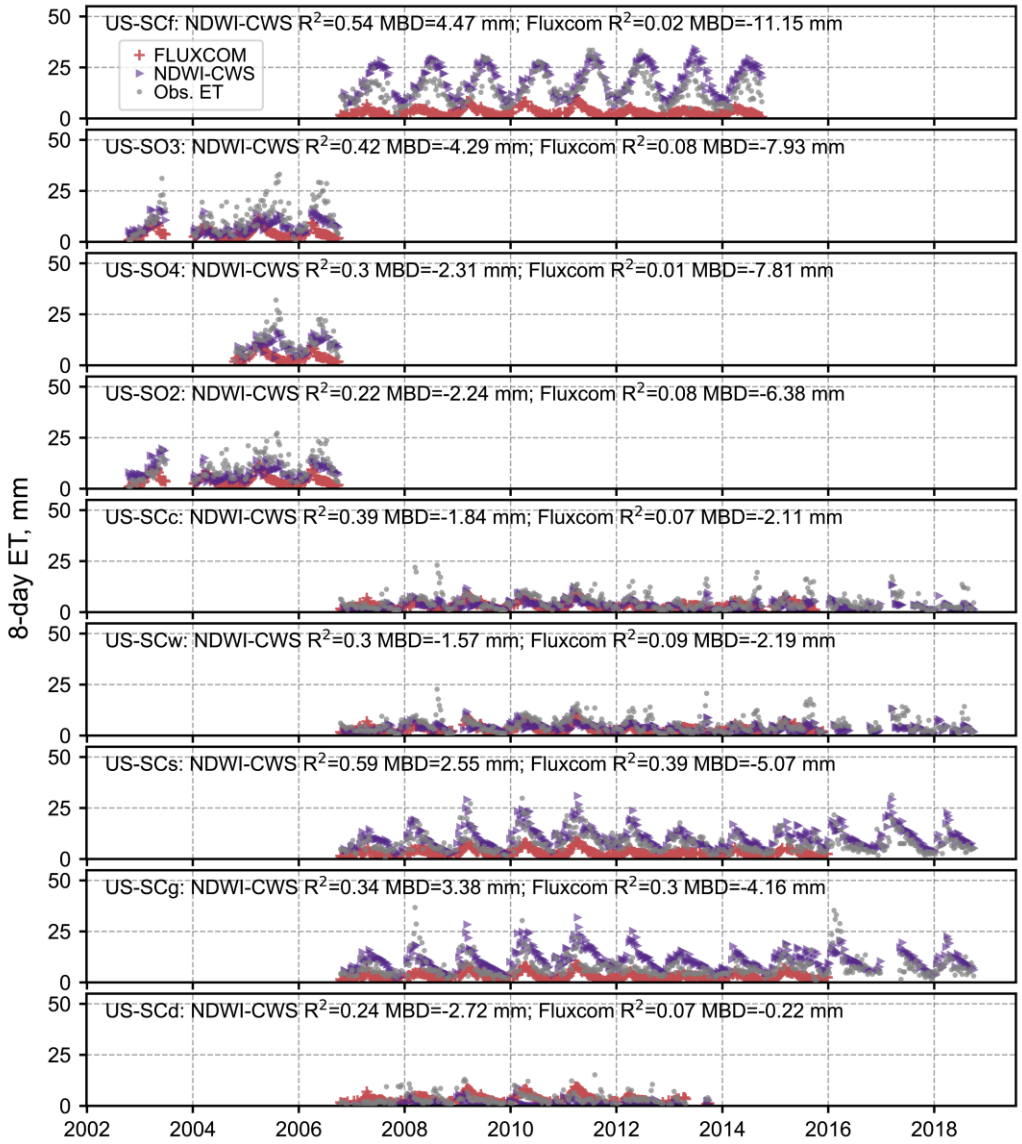

Figure S8. Comparison of 8-day ET from flux-tower observation, NDWI-CWS model, and FLUXCOM model at 9 sites in California but outside of the Sierra Nevada.

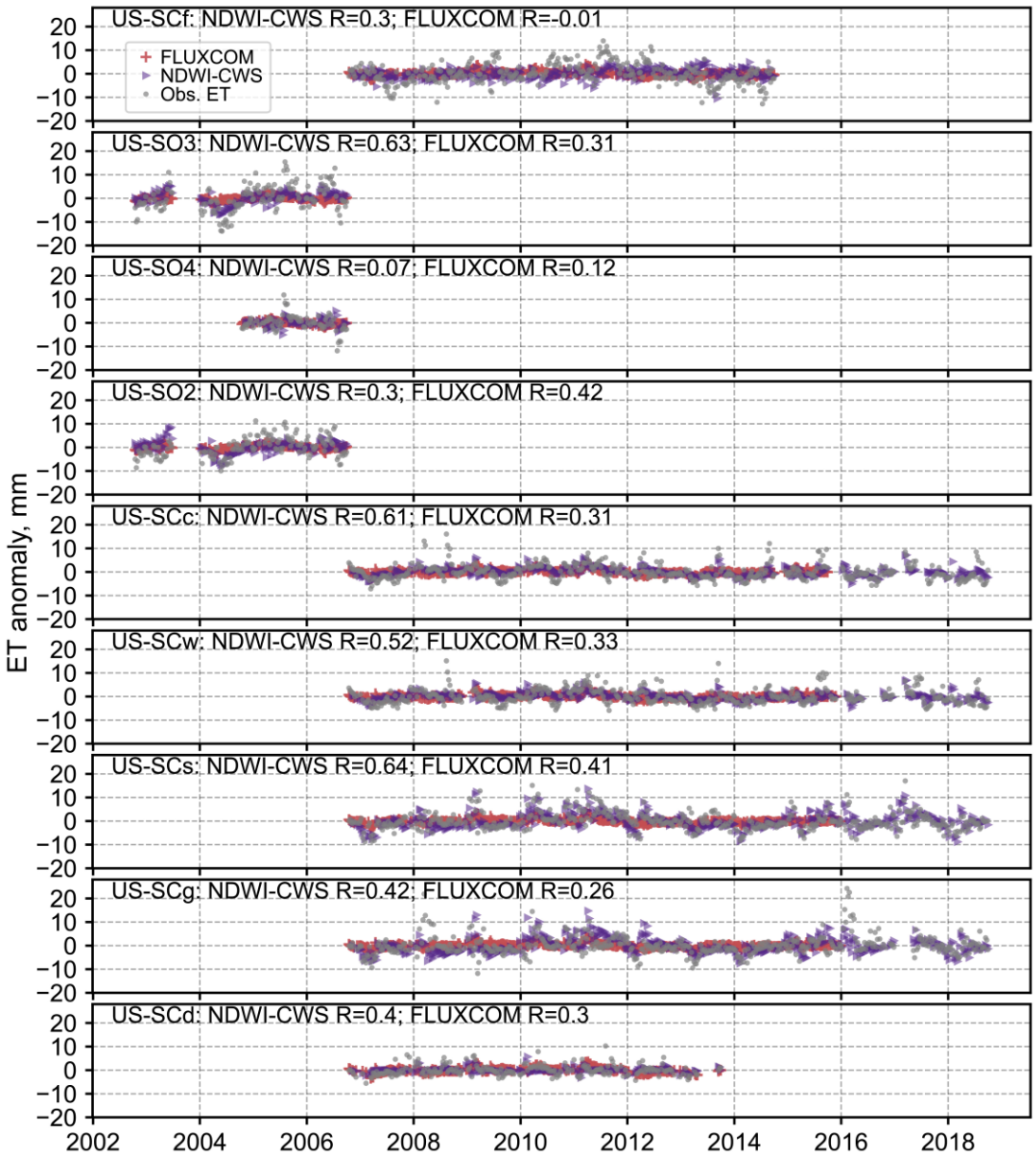

Figure S9. Comparison of 8-day ET anomaly: flux-tower observation (gray marker), NDWI-CWS model (purple marker), and FLUXCOM model (red marker) at 9 sites in California but outside of the Sierra Nevada.

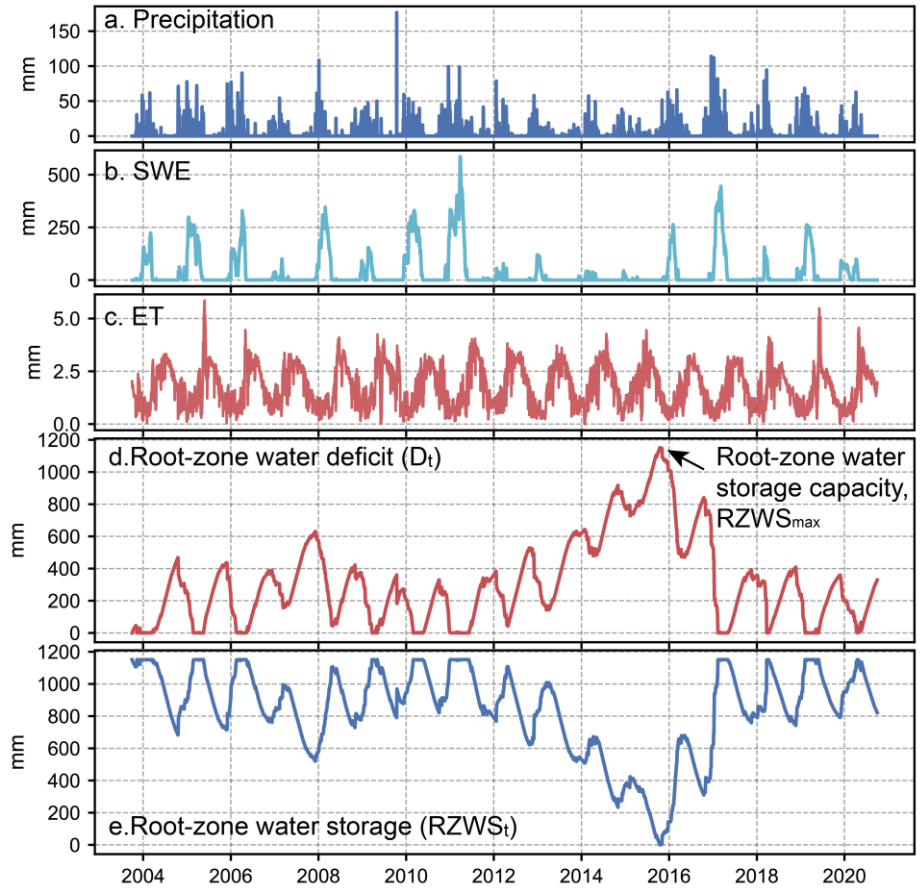

Figure S10. Example of daily water deficit (d), daily root-zone water storage (e), and root-zone water storage capacity (d) calculated using daily precipitation (a), snow water equivalent (b), and NDWI-CWS ET (c). Data at the US-CZ3 site are shown for this example.

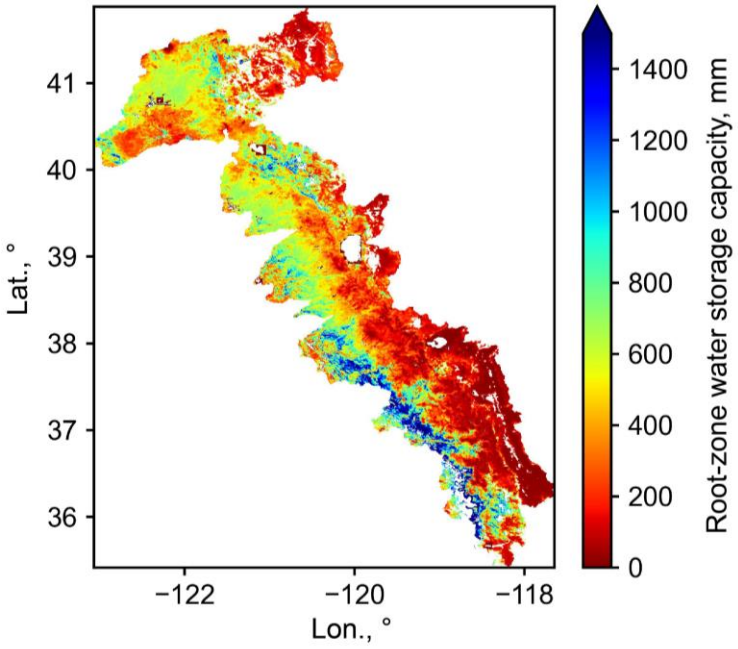

Figure S11. Map of root-zone water storage capacity $RZWS_{max}$.

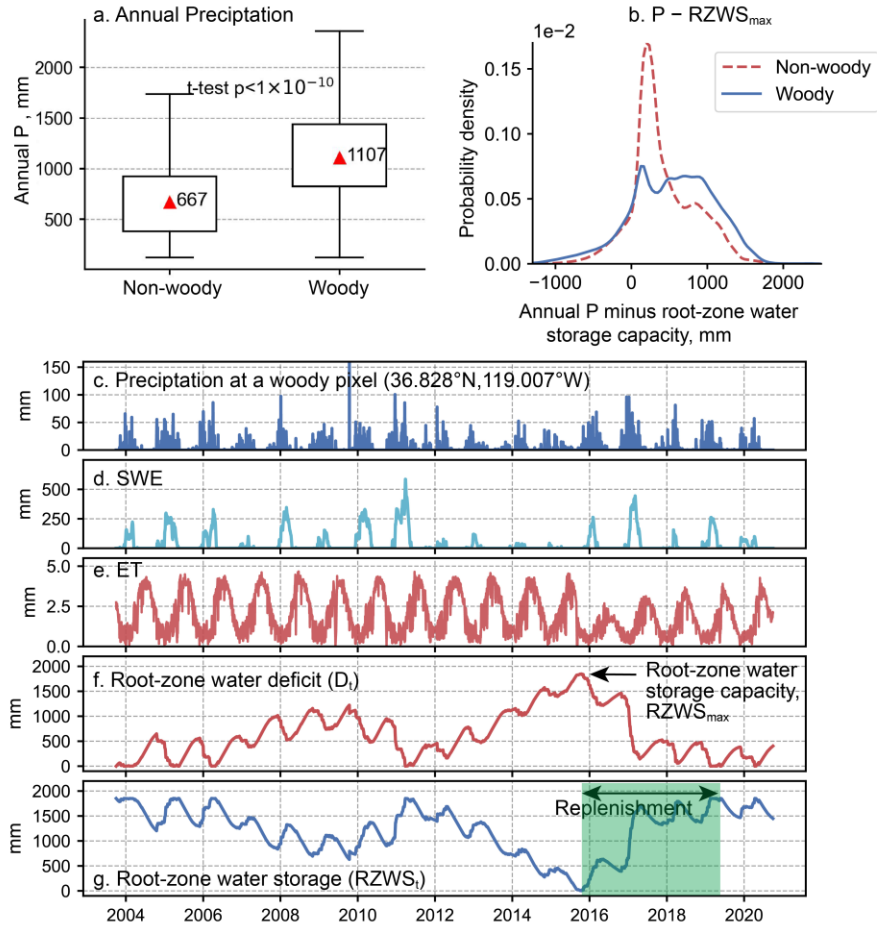

Figure S12. (a) Comparison of mean annual precipitation between woody and non-woody areas. Red triangle in the boxplot denotes the labeled mean value. The p-value from the Student T test is labeled. (b) Probability density of annual precipitation minus root-zone water storage capacity. Panels c-g are the same as Figure S9, but for a woody pixel at 36.828°N, 119.007°W. The green shaded area in panel g indicates the replenishment of root-zone water storage after the overdraft during the 2012-2015 drought.

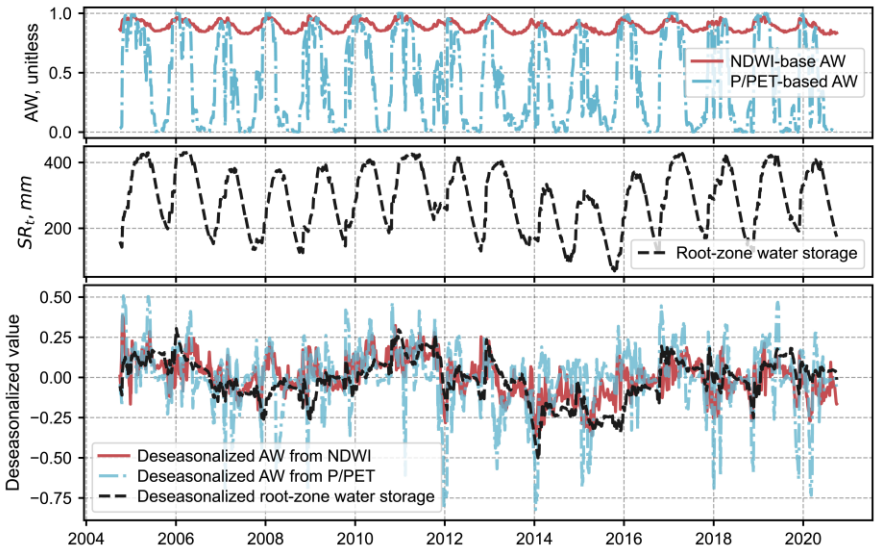

Figure S13. Deseasonalized values of domain-averaged AW calculated using NDWI and P/PET, versus deseasonalized root-zone water storage.

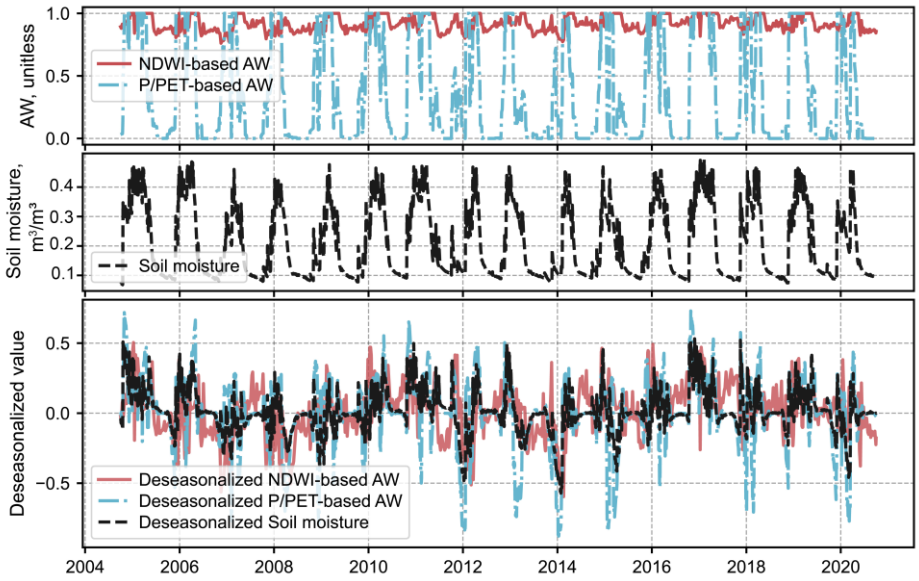

Figure S14. Deseasonalized values of daily AW calculated using NDWI and P/PET, versus deseasonalized soil moisture at the US-Ton flux-tower site.

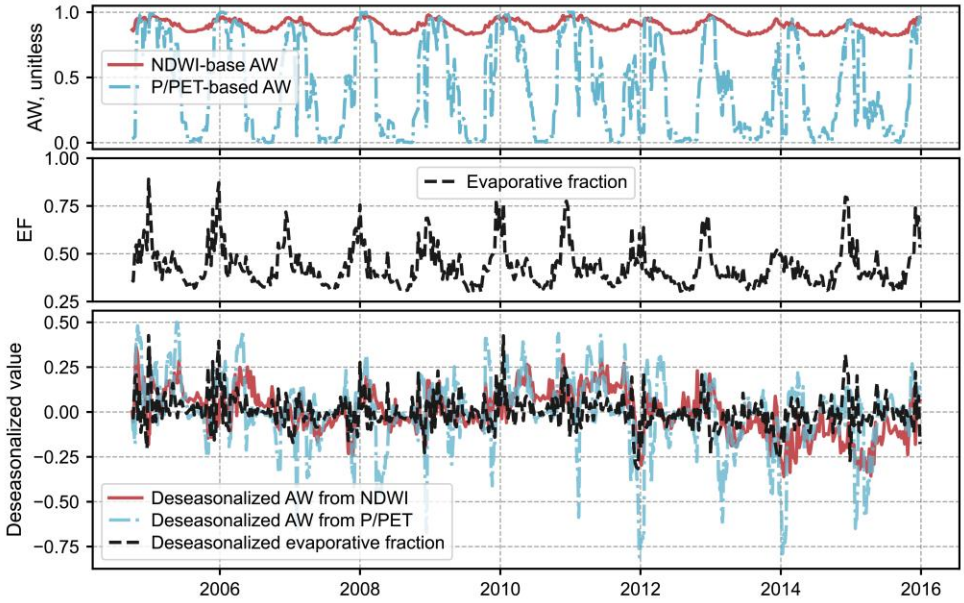

Figure S15. Deseasonalized values of domain-averaged AW calculated using NDWI and P/PET, versus deseasonalized evaporative fraction (EF, the ratio of latent heat flux to the sum of latent and sensible heat fluxes from FLUXCOM product).

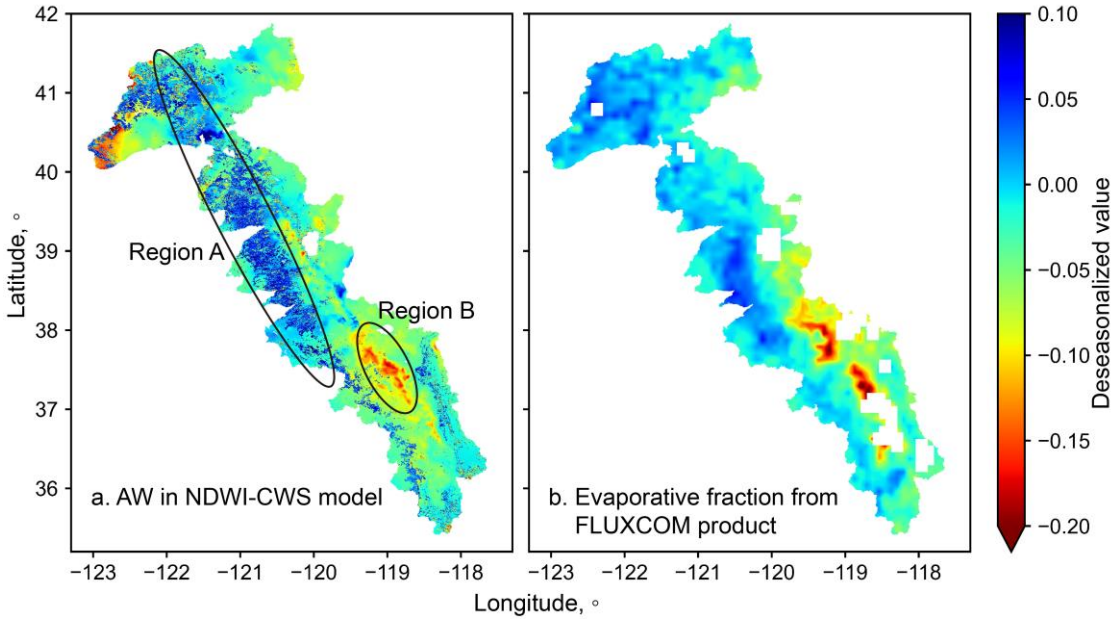

Figure S16. Maps of deseasonalized values of AW from NDWI-CWS model versus evaporative fraction from FLUXCOM product on June 18, 2012. The correlation between the two ET-water-stress-relevant variables is 0.36. Region A marks the woody areas with wet anomalies, and Region B for non-woody areas with dry anomalies.

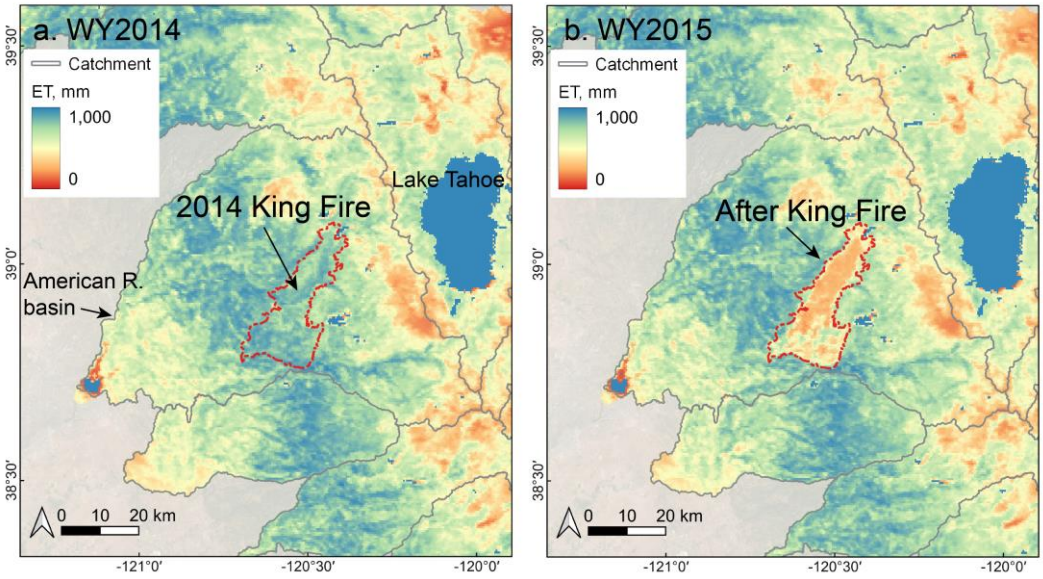

Figure S17. Annual NDWI-CWS ET comparison between a) WY2014 before the King Fire (boundary denoted by red dashed line; September 13, 2014 - October 31, 2014) and b) WY2015, one year after the King Fire.

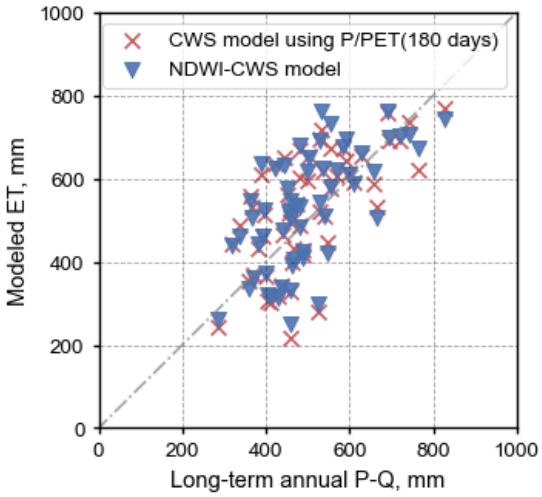

Figure S18. Scatterplot of annual ET from P – Q at 58 catchments with long-term (≥ 10 years) measurements versus ET estimates from 1) the original CWS model using AW from P/PET using 180 days and 2) NDWI-CWS model using NDWI-based AW.

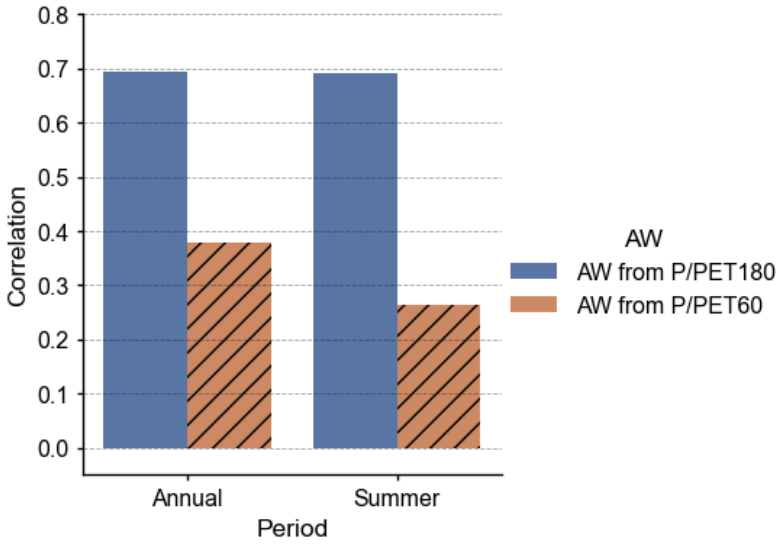

Figure S19. Correlation between deseasonalized root-zone water storage and deseasonalized AW values from P/PET using 180 days (i.e. CWS model with AW using P/PET180) and 60 days (i.e. the original CWS, labeled as P/PET60) in Equation 3.

References:

Baldocchi, D.D., Xu, L., Kiang, N., 2004. How plant functional-type, weather, seasonal drought, and soil physical properties alter water and energy fluxes of an oak–grass savanna and an annual grassland. Agric. For. Meteorol. 123, 13–39. https://doi.org/10.1016/j.agrformet.2003.11.006

Cui, G., Anderson, M., Bales, R., 2023. Runoff response to the uncertainty from key water-budget variables in a seasonally snow-covered mountain basin. J. Hydrol. Reg. Stud. 50, 101601. https://doi.org/10.1016/j.ejrh.2023.101601

Cui, G., Rice, R., Anderson, M., Avanzi, F., Hartsough, P., Guo, W., Conklin, M., Bales, R., 2022. Precipitation estimates and orographic gradients using snow, temperature, and humidity measurements from a wireless-sensor network. Water Resour. Res. 58, e2021WR029954. https://doi.org/10.1029/2021WR029954

Kim, J., Guo, Q., Baldocchi, D., Leclerc, M., Xu, L., Schmid, H., 2006. Upscaling fluxes from tower to landscape: Overlaying flux footprints on high-resolution (IKONOS) images of vegetation cover. Agric. For. Meteorol. 136, 132–146. https://doi.org/10.1016/j.agrformet.2004.11.015

Ma, S., Baldocchi, D., Wolf, S., Verfaillie, J., 2016. Slow ecosystem responses conditionally regulate annual carbon balance over 15 years in Californian oak-grass savanna. Agric. For. Meteorol. 228–229, 252–264. https://doi.org/10.1016/j.agrformet.2016.07.016

Worldbank, 2022. World Bank Climate Change Knowledge Portal [WWW Document]. URL https://climateknowledgeportal.worldbank.org/country/italy/climate-data-historical (accessed 8.23.22).